Identification of nuclear pore proteins at plasmodesmata: potential role in intercellular transport?

T. Moritz Schladt[1,*, §], Manuel Miras[1,3,*], Jona Obinna Ejike[1,2,*], Mathieu Pottier[1,4,*], Lin Xi[5], Andrea Restrepo-Escobar[1], Masayoshi Nakamura[6,7], Niklas Pütz[1], Sebastian Hänsch[2,8], Chen Gao[1], Julia Engelhorn[1,2], Marcel Dickmanns[1,9], Gwendolyn V. Davis[1], Ahan Dalal[1,2], Sven Gombos[5], Ronja Lange[1], Rüdiger Simon[2,9], Waltraud X. Schulze[5] & Wolf B. Frommer[1,2,6,§]

[1] Heinrich Heine University Düsseldorf, Faculty of Mathematics and Natural Sciences, Institute for Molecular Physiology, 40225 Düsseldorf, Germany
[2] Cluster of Excellence on Plant Sciences, Heinrich Heine University Düsseldorf, 40225 Düsseldorf, Germany
[3] New address: Department of Stress Biology and Plant Pathology, CEBAS-CSIC, E-30100 Murcia, Spain
[4] New address: Université de Lorraine, INRAE, IAM, F-54000 Nancy, France
[5] Department of Plant Systems Biology, University of Hohenheim, 70593 Stuttgart, Germany
[6] Institute for Transformative Biomolecules (WPI-ITbM), Nagoya University, 464-860 Nagoya, Japan
[7] New address: Department of Biochemistry and Molecular Biology, Saitama University, 330-8570 Saitama, Japan
[8] Center for Advanced Imaging; Heinrich Heine University Düsseldorf, 40225 Düsseldorf, Germany
[9] Department of Molecular Structural Biology, Max Planck Institute of Biochemistry, Martinsried, Germany
[10] Heinrich Heine University Düsseldorf, Faculty of Mathematics and Natural Sciences, Institute of Developmental Genetics, 40225 Düsseldorf, Germany

* Equal contribution
§ For correspondence: schladti@hhu.de, frommew@hhu.de

Abstract

Plasmodesmata (PD) mediate intercellular exchange of small molecules, RNAs and proteins between plant cells with an apparent exclusion limit for passive non-specific transport, and transport of specific cargo mediated by mediators. PD and nuclear pore complexes (NPC) are nanometer sized micropores with strikingly similar properties. Cargo translocation through NPC is mediated by phase separating FG-nucleoporins (FG-NUP). Here, bioinformatics, proteomics and fluorescence imaging identified FG-NUPs at PD. Transient expression of GFP fusions at low and intermediate expression levels supported dual localization of 12 NUPs to NPC and PD. Structured illumination microscopy detected the transmembrane anchor NUP CPR5 close to orifices of PD. *cpr5* mutants showed reduced intercellular short-root (SHR) transport. However, transport defects cannot be excluded due to indirect effects in the mutants. Identification of FG-NUPs at PD is consistent with the recruitment of NUPs to form a PD pore gating complex consistent with phase separation domains as diffusion barriers at PD. Further analyses will be required to determine whether NUPs are *bona fide* PD components, or accumulate at PD in certain conditions, or may serve intermediate NPC storage.

Introduction

Nutrient exchange and communication between cells are essential for multicellular organisms. Besides membrane transporters and cell surface receptors, metazoa, fungi and plants independently evolved cell-cell bridges. The green lineage developed unique structures, called plasmodesmata (PD), composed of modified cell wall domains that form plasma membrane-lined channels and that contain an ER-derived desmotubule providing continuity between the cytoplasm of neighboring cells (symplasm). Since PD are embedded into the cell wall and contain diverse membrane and soluble proteins, PD pose a major challenge for biochemical and cell biological analyses. Several studies obtained PD proteomes by enriching membrane proteins in cell wall fractions (Bayer et al., 2006; Brault et al., 2019; Fernandez-Calvino et al., 2011; Gombos et al., 2023). Genetic approaches failed so far to identify proteins that could fully explain the transport mechanism, possibly due to redundancy or lethality of mutants. Intercellular transport studies are also challenging since intact at minimum, a functional two cell system is required. Current models for PD translocation implicate a simple filter mechanism generated by spoke-like structures connecting the peripheral plasma membrane with the desmotubule, however the complex transport properties as well as inconsistencies such as the finding that sleeveless PD lacking an obvious path may put these models in question.

Key features of PD transport include the ability to translocate highly diverse cargo (from ions to macromolecules), an apparent size exclusion limit (which, depending of the type of PD, can reach 70 kDa, in funnel PD up to 120 kDa), and the ability to translocate specific cargo (Paultre et al., 2016; Ross-Elliott et al., 2017). Translocation through PD and the nuclear pore complex (NPC) share common features, namely both NPC and PD transport a similar spectrum of cargo species (ions, metabolites, proteins, and ribonucleoprotein complexes)(Ejike et al., 2025; Lee et al., 2000). For both NPC and PD, the ability for pore dilation has been described (Kragler et al., 1998; Zimmerli et al., 2021). Both NPC and PD constitute selective barriers, allowing '*passive passage of molecules'* with an apparent size exclusion limit (term used in animal literature; named '*non-targeted movement*' for PD) and '*facilitated translocation of specific macromolecules'* ('*targeted movement*' for PD)(Crawford and Zambryski, 2001; Frey et al., 2018). Notably, the surface properties of cargo proteins play an important role for translocation, allowing even tetrameric GFP variants with compatible surface properties to pass (Frey et al., 2018). The core of the permeability barrier of the NPC appears to be a separated phase / condensate formed by disordered phenylalanine–glycine (FG) repeat-containing proteins, the FG-nucleoporins (Frey et al., 2018; Hoogenboom et al., 2021; Ng et al., 2021; Yu et al., 2023). These smart sieves mediate passage of smaller molecules without interaction with the FG repeats, while larger molecules or specific cargo can pass with the help of nuclear transport receptors that specifically interact with the FG repeats (Kehlenbach et al., 2023). As a shared structure among eukaryotes, the ultrastructure, function and transport mechanism of the NPC is well understood (Ejike et al., 2025; Mosalaganti et al., 2022). The human NPC, with about 1000 polypeptides, has an approx. diameter of 120 nm, a pore size of ~43 nm and a height of 80 nm generated by membrane-anchors, three stacked rings (a sandwich of two outer and one inner ring), cytoplasmic filaments, and a nucleocytoplasmic basket (Lin and Hoelz, 2019). The human genome encodes twelve FG-nucleoporins (NUPs): NUP42, NUP50, NUP54, NUP58 (aka NUP45), NUP62, NUP98, NUP153, NUP214, POM121, POM121B, POM121C, and NUP358(Terry and Wente, 2009), while plant genomes encode ten FG-NUPs: NUP42 (aka CG1), NUP50a & NUP50b, NUP54, NUP58, NUP62, NUP98a & NUP98b, NUP136 and NUP214 (Chopra et al., 2019; Makarov et al., 2021). The majority of the FG-NUPs were conserved, with two FG-NUPs apparently lost in the green lineage (POM121, NUP358).

FG-NUPs and other NUPs in PD fractions of *Physcomitrium patens* and localization to PD

Based on the striking similarities in transport properties, we hypothesized that PD transport may use permeability barriers similar as the NPC, that is, phase-separation generated by FG-repeat proteins. We thus explored whether the green lineage evolved a distinct set of FG-repeat containing proteins. A bioinformatic search for FG repeat-containing proteins in the genome of the moss *P. patens* revealed that 12 out of the 15 top-ranked FG-containing proteins were NUPs; the other three proteins were not considered candidates for a transport function (table S1; file S1; file S2 for Arabidopsis FG-containing proteins). An alternative hypothesis was that the PD permeability barrier is generated by NUPs derived by tandem gene duplications followed by differentiation into NPC and PD functions. However,

phylogenetic analyses of Arabidopsis *NUPs* showed that the majority of NUPs are encoded by single genes (see also table S2 for overview of Arabidopsis *NUPs*)(Makarov et al., 2021; Zhang et al., 2020). Interestingly, however, the PD proteome from *P. patens* contained FG-NUP50a and two other NUPs, SEC13 and NUA (Gombos et al., 2023). Since PD cannot be purified to homogeneity, we cannot exclude that these NUPs represent contaminations. Previous work had indicated that *bona-fide* moss PD proteins can be targeted to PD when expressed in tobacco leaves (Gombos et al., 2023). To test whether FG-NUPs localize exclusively to the NPC or can also be targeted to PD, the subcellular localization of fluorescent protein (FP) fusions of three *P. patens* FG-NUPs (NUP58, NUP62 and NUP98) was analyzed by confocal microscopy after β-estradiol-controlled transient expression in *Nicotiana benthamiana*. A substantial number of fluorescent puncta derived from C-terminal mVenus fusions of the three FG-NUPs overlaid with fluorescent puncta of aniline blue marking callose at PD (Figure 1; Figure1-figure supplement 1). PD localization did not appear to be due to an FG-NUPs-specific mis-localization, since the inner ring linker NUP35, which connects the transmembrane interaction hub with the ALADIN-NDC1 core to NUP155, also localized to PD (Figure 1). Of note, the fluorescent puncta derived from mVenus fusions in the periphery did not exclusively localize to aniline blue labeled PD pit fields. Fluorescent mVenus and aniline blue derived puncta were also separately detected in locations without overlay. It is known that aniline blue does not detect all pit fields (Huang et al., 2022). Notably, transient expression in *N. benthamiana*, even though controlled by use of an estrogen-inducible system, can lead to overexpression; thus, the observed localization could either represent a physiologically relevant site for accumulation when under conditions of excess, or be due to accumulation in the vicinity of PD orifices.

FG-NUPs and other NUPs in PD fractions of Arabidopsis

To explore whether FG-NUPs may also be present in PD fractions from a vascular plant, we utilized established PD enrichment and data analysis pipelines to generate a PD proteome from Arabidopsis shoots (Gombos et al., 2023). This shoot PD proteome had an overlap of 80% with published PD proteomes and included ~43% of known high-confidence PD proteins, e.g., the well-established plasmodesmata-located proteins (PDLP) and multiple C2 domains and transmembrane region proteins (MCTP) PD markers (table S3, Figure 2-figure supplement 1 and 2, file S3)(Brault et al., 2019; Thomas et al., 2008). The Arabidopsis PD-enriched fraction included seven Arabidopsis FG-NUPs (Figure 2A). Moreover, inner and outer ring and basket NUPs were found in the high-confidence PD protein list (Figure 2A, C). In total, 20 proteins from different NPC domains were identified. 15 proteins were enriched in PD fractions compared to cell wall and total Arabidopsis protein fractions (Figure 2A, C, Figure 2-figure supplement 1 and 2). Several of the identified nuclear pore components passed the threshold for consideration as high-confidence PD proteins, in particular proteins of the inner and outer rings, core and basket. High-confidence PD scoring was based on enrichment in biochemical PD fractions as well as on an iterative weighting process which factors in features of known PD-localized proteins (Gombos et al. 2023). Separation of PD scores of "likely PD proteins" and likely contaminants (here: plastidic and mitochondrial proteins)(Fernandez-Calvino et al., 2011; Gombos et al., 2023) was significant, allowing to define confidence scores. NUP proteins were also previously identified in PD proteome preparations. In particular NUPs such as FG-NUPs NUP62, NUP214, NUP50a, as well as CPR5, GP210, NUP35, NUP93a, NUP155, NUP205, NUP43, HOS1 (aka HOS1/ELYS), SEC13, and NUP82 were found in proteomics data of cell wall/PD protein fractions from other studies (table S4)(Bayer et al., 2006; Fernandez-Calvino et al., 2011; Gombos et al., 2023; Kirk et al., 2022; Kraner et al., 2017). Biochemical enrichment of PD resulted in enrichment of well-established PD proteins, such as PDLPs and MCTPs (Figure 2-figure supplement 2). As expected, likely contaminants, such as plastidic and mitochondrial proteins were depleted during PD preparation. Very highly abundant proteins, such as cytosolic ribosomal proteins, as well as histones remained high in all fractions. Ribosomal proteins did not show significant differences in abundance between fractions, while histones seemed enriched in cell wall preparations. The abundance of nuclear proteins of the nucleus showed distinct patterns: NUPs were enriched in cell wall and PD fractions compared to total cell extract, as 75% of NUP proteins were more abundant in PD fractions, exceeding the proportions observed in TC (60%) and CW (~50%) fractions. The abundance of other nuclear envelope proteins was unaffected by the PD purification and showed no enrichment in PD fractions (Figure 2-figure supplement 2). In contrast to NUPs, ER-resident proteins displayed no significant change in abundance in the cell wall fraction compared to total cell extract, yet showed a slight but consistent enrichment in the PD fraction (Figure 2-figure supplement 2). Of note, grouping of the proteins provides an average; individual proteins within

156 each group may deviate from the average pattern. While the detection of a large number of NUPs
157 including FG-NUPs in the PD fractions, even with enrichment, may support a possible role in PD
158 functions, we can not fully exclude that they represent contaminants.

159 **Localization of Arabidopsis FG-NUPs and other NUPs to PD**

160 To explore whether Arabidopsis FG-NUP-mVenus fusions can be detected at PD, candidates were
161 expressed from an β-estradiol-inducible promoter in *N. benthamiana* leaves. Fluorescence derived from
162 FP-fusions of the FG-NUP58, FG-NUP62 and FG-NUP98b overlaid with aniline blue fluorescent puncta
163 (with a significantly higher PD index relative to that for the non-specific cell wall dye propidium iodide,
164 Figure 3A, B, Figure 3-figure supplement 1, table S2), indicating that Arabidopsis FG-NUPs can be
165 targeted to PD. Notably, 12 out of a total of the 16 NUPs tested here localized to puncta in the cell
166 periphery that overlaid with aniline blue fluorescence at pit fields (Figure 3, Figure 4A, B; Figure 3-figure
167 supplement 1, list of 16 tested NUPs: table S2)(Zavaliev and Epel, 2015). Overall, 12 NUPs showed
168 significant enrichment at PD compared to the cell wall marker (Figure 3B, Figure 4B, table S2), including
169 two outer ring NUPs (NUP43, HOS1/ELYS) and two transmembrane NUPs (GP210, CPR5) (Figure 4B,
170 H). Ten NUP fusions for various inner and outer ring and membrane anchor NUPs were also detected in
171 nuclei (Figure 3-figure supplement 1). Fluorescent puncta of aniline blue and FP-fusions of PD protein
172 typically do not provide a perfect colocalization since aniline blue staining does not mark all PD and
173 typically, the overlay is partial since FP-fusions are not detected at all PD even for high confidence PD
174 proteins (Pendle and Benitez-Alfonso, 2015). As an independent line of evidence we observed overlay of
175 the PD marker PDLP5-mScarlet3 and an mCitrine fusion of the putative NUP107-160 complex
176 recruitment factor HOS1/ELYS at PD (Figure 4G). To test for potential artifacts, caused possibly by
177 mistargeting due to overexpression, the concentration of the inducer β-estradiol and the induction time
178 were reduced. In leaves transiently expressing NUP43-mCitrine or CPR5-FP fusions, the fluorescence
179 intensity correlated with the estradiol concentration used, with decreased fluorescence intensity for
180 samples where 2μM estradiol was applied versus the intensity in samples exposed to 20μM estradiol
181 (Figure 4 D,E). Notably, the fluorescence ratio between periphery and nucleus did not differ significantly
182 after expression induction by 2 μM compared to 20 μM β-estradiol (Figure 4F) and PD localization was
183 not eliminated (example for localization of NUP43-mCitrine in Figure 4C; PD index(NUP43, 2μM) =
184 1.42, PD index(CPR5, 2μM) = 1.40). The resolution of confocal imaging is insufficient to conclude that
185 the NUPs localize inside PD or accumulate in the vicinity. We also cannot exclude that expression of the
186 NUP fusions leads to mis-targeting to PD. Different from data obtained for NUP98a (Gallemí et al., 2016),
187 a C-terminal mVenus fusion to the auto-cleavable NUP98b was fluorescent and localized to PD (Figure
188 3, Figure 3-figure supplement 1), indicating that either under the condition used in our experiments, the
189 main fraction of NUP98b was unprocessed, or that the C-terminal peptide reassociated with the N-
190 terminal domain of NUP98b, as previously described for the two splice forms of the human NUP98
191 (Hodel et al., 2002). Out of 16 NUPs tested, four NUPs did not localize at PD, as indicated by non-
192 significant PD indices over the cell wall marker (p-values > 0.08, table S2). Out of 35 currently known
193 Arabidopsis NUPs, 19 NUPs were not yet tested here (table S2).

194 Single copy insertions of GFP-fusions in stable transformants reduce the potential for artifacts caused by
195 overexpression. Analysis of nine independent stably transformed homozygous single insertion
196 Arabidopsis lines expressing a full-length genomic FG-NUP62-GFP fusion under the control of the native
197 NUP62 promoter showed dual localization of the protein to the nuclei and PD. However, PD localization
198 was only detected in mature cotyledons older than 10 days (Figure 3C-E). Notably, the peripheral
199 localization of NUP62-GFP was not restricted solely to PDs, as punctate fluorescence was detected at the
200 cell surface, outside of PD regions (Figure 3E). NUP62 protein abundance in two-week-old cotyledons
201 of the stable NUP62p:NUP62-GFP transformants was not statistically different to NUP62 protein levels
202 in WT (Figure 3F). Notably, the punctate fluorescence at the cell periphery, encompassing both PD-
203 associated and non-PD-associated localization, were not detectable or absent in roots and young leaves of
204 four-day-old seedlings (Figure 3D). However, it cannot be excluded that the GFP fusion impacts NUP62
205 localization.

206 Components of the inner ring, NUP93a and NUP155, and the basket, NUP82, were also detected at PD
207 when heterologously overexpressed in *N. benthamiana*, although with lower confidence compared to,
208 e.g., CPR5. Analysis of published data from other groups, who had localized NUPs to nuclei also showed

peripheral puncta, which had not been analyzed further (table S5). We assessed whether NUP localization is distinct from ER localization in *N. benthamiana* leaves that heterologously co-expressed NUP43-mVenus and the ER luminal marker mCherry-HDEL. The localization patterns of NUP43-mVenus and of the mCherry-HDEL luminal ER marker were clearly distinct (Figure 5, Figure 5-figure supplement 1). NUP43-mVenus may be associated to the ER, however restricted to subregions of the ER, which partially overlay with aniline blue-labeled pit fields (Figure 5, Figure 5-figure supplement 1). As of now, we cannot exclude that the localization in the periphery is an overexpression artifact due to accumulation in the ER at the orifices of PD since the complexes are too large for translocation (Giordano et al., 2013). Alternatively, the puncta in the periphery could be the consequence of an accumulation, when biotic or abiotic conditions lead to elevated production of NUPs that cannot replace existing NUPs, similar to annulate lamellae (AL). In such conditions, the peripheral accumulation might serve as cellular storage of excessive NUPs. Interestingly, in mammalian cells, depletion of NUP98 led to FG-NUP accumulation sites in the periphery at ER junctions. Such sites of accumulation may serve as NUP storage depots rather than sites of degradation (Pletan et al., 2025).

Topology of CPR5, a potential membrane anchor at both NPC and PD

Since the phase separation domain in the nuclear pore is produced by ten FG-NUPs and PD appear to contain multiple FG-NUPs, it may be necessary to mutate multiple *FG-NUP* genes before it is possible to observe intercellular transport defects (Xiao et al., 2020). It is also conceivable that *knock-out* mutants in multiple *FG-NUPs* may be lethal. We thus rather focused on the green lineage-specific membrane anchor CPR5, a nuclear pore component with a high PD index of 1.48 (Figure 4, table S2). Four potential membrane proteins that anchor the human NPC in the nuclear membrane had been identified: GP210, POM121, NDC1 and TMEM33. Arabidopsis encodes genes for three anchors GP210, NDC1 and PNET1 (homolog of human TMEM209; table S6), while CPR5 had been proposed to serve as an anchor in the equatorial plane of the NPC (Apelt et al., 2016; Gu et al., 2016). Since CPR5 was among the top 5 candidates based on the PD index, one may hypothesize that it may serve as an anchor for an NPC-like structure at PD (Figure 4A, B, Figure 3-figure supplement 1). CPR5, a polytopic membrane protein, is predicted to form a globular helix bundle domain at its N-terminus, flanked by disordered regions and connected to a 105 amino acid α-helix (Figure 6-figure supplement 1). The central helix contains a hydrophobic region, which, together with four shorter hydrophobic helices, forms an approximately 35 Å long transmembrane domain, consistent with the expected thickness of ER membranes. The C-terminus possibly extends into the ER lumen. While it has been considered that CPR5 may play specialized roles, e.g., in defense reactions, it is also conceivable that the phenotypes are secondary defects (Arra et al., 2024; Gu et al., 2016; Ma et al., 2023; Peng et al., 2022), caused by the missing anchoring activity (Apelt et al., 2016; Gu et al., 2016). CPR5 is encoded by a single gene in Arabidopsis and two in rice (Figure 6-figure supplement 2, table S6, table S7)(Arra et al., 2024). In PD, CPR5 could either be embedded into the plasma membrane near or at PD, with the C-terminus facing the apoplasm, or into the ER/desmotubule membrane, with its C-terminus facing the desmotubule lumen (or ER lumen in the vicinity of PD) and the long N-terminal domain pointing into the intermembrane space of PD/cytosol, analogous to the CPR5 topology in the ER-derived nuclear membrane at the NPC. A split-GFP system for topology studies of membrane proteins was used to determine whether the C-terminus of CPR5 faces the luminal side of the ER (Xie et al., 2017). When an N-terminal GFP11 fusion to CPR5 was co-expressed with a free cytosolic GFP1-10, fluorescence was reconstituted, consistent with the N-terminus being located in the cytosol or the cytosolic sleeve of PD (Figure 6A; Figure 6-figure supplement 3). A control using a GFP1-10 domain targeted to and retained in the ER lumen (GFP1-10-HDEL) did not show detectable fluorescence reconstitution (Figure 6B). The complementary fusion of GFP11 to the C-terminus of CPR5 led to reconstitution of fluorescence when co-expressed with an ER lumen targeted GFP1-10-HDEL, but not when co-expressed with a cytosolic GFP1-10 (Figure 6A, B; Figure 6-figure supplement 3). The topological data are consistent with a model in which the C-terminal five-helix-bundle of CPR5 traverses the ER/desmotubule membrane with the C-terminus inside the lumen of the ER/desmotubule, while the extended central α-helix, the predicted unstructured domains, and the smaller helical bundle of CPR5 are located in the intermembrane space between the ER/desmotubule and the plasma membrane (Figure 6-figure supplement 1).

Localization of CPR5 at the orifices of PD

A hypothetical NPC-like structure could serve as a micropore in the PD channel, or be present close to the PD entrance. To determine CPR5 localization in the PD at higher resolution, we performed structured illumination microscopy (SIM) with a CPR5-mCitrine fusion. CPR5 was found to localize adjacent to aniline blue labeled callose deposition at PD. Therefore, CPR5 may localize to or near the neck region of PD, but not in the central cavity of the PD, where a PDLP5-mScarlet3 was localized (Figure 6C, D; Figure 6-figure supplement 4)(Fitzgibbon et al., 2010). These findings are consistent with a model in which NUPs are present at or close to the PD orifices. We did not observe puncta at both paired neck regions in all cases (Figure 6-figure supplement 4B, top), possibly due to mosaic-like expression in *N. benthamiana*, in which only one of the adjacent cells expressed the fusion protein (model: Figure 6D). CPR5-mCitrine localization was absent at some PD (Figure 6-figure supplement 4B, *bottom*): in 10 images from 3 independent repeats, CPR5-mCitrine and PDLP5-mScarlet3 localized to 76 ± 6% and 81 ± 10% of the aniline blue labeled pit fields, respectively, while CPR5-mCitrine localized to 79 ± 9% of the PDLP5-mScarlet3 puncta (Figure 6-figure supplement 4D). Note that CPR5-mCitrine also localized in the periphery outside PD (Figure 6-figure supplement 4D). To assess whether the CPR5-mCitrine fusion protein is functional in Arabidopsis, we tested whether CPR5p:CPR5-mCitrine (including all introns) expression in the *cpr5-1* mutant background results in a rescue of the severe growth phenotype of the *cpr5-1* loss-of-function mutant (Bowling et al., 1997). Indeed, roots were significantly longer in the two independent transgenic *cpr5-1*/CPR5p:CPR5-mCitrine Arabidopsis lines compared to the *cpr5-1* mutant, and four-week-old plants showed a more WT-like growth phenotype (Figure 7-figure supplement 1, G–I). However, we could not detect fluorescence in 10-14 day old seedlings, which could be due to a variety of reasons, such as cleavage of the FP and degradation of the FP without accumulating elsewhere in the cells. The lack of fluorescence in the transgenic lines requires further investigation.

Intercellular transport defects in *cpr5* mutants

If indeed NUPs form phase-separated barriers at PD to control cell-to-cell transport, and given the defects of *cpr5* mutants in nuclear transport, one may expect that interference with CPR5 function might impair *facilitated and non-facilitated cell-to-cell translocation of specific macromolecules*. Particle bombardment of Arabidopsis leaves was performed to transiently express a tandem-GFP fusion (2xmEGFP; 54 kDa) in two independent *cpr5* loss-of-function mutants (EMS mutant *cpr5-1* (G420D) and T-DNA insertion mutant *cpr5-T3* ; Figure 7-figure supplement 1A, B)(Bowling et al., 1997; Crawford and Zambryski, 2000; Faulkner et al., 2013; Gu et al., 2016; Otero et al., 2016; Sakulkoo et al., 2018; Wang et al., 2017). Cell-to-cell movement of 2xmEGFP was significantly reduced in the *cpr5* mutants relative to wild type (WT) (Figure 7A, B; Figure 7-figure supplement 1A, B). Originally named for its *constitutive pathogen response* phenotype, loss of CPR5 activity can trigger constitutive defense responses that could cause callose deposition and closure of PD (Kohler et al., 2002), however, callose levels were not significantly different (Figure 7C).

The transcription factor SHORT-ROOT (SHR), produced in cells of the stele, migrates into the endodermis by *facilitated cell-to-cell translocation,* followed by nuclear import (Nakajima et al., 2001). Intercellular transport of SHR is crucial for tissue patterning (Koizumi et al., 2012; Nakajima et al., 2001; Winter et al., 2024). To explore whether SHR-GFP (86.6 kDa) movement was impacted in a *cpr5* loss-of-function mutant, we compared the endodermis-to-stele ratio (E:S ratio) of GFP fluorescence intensity in roots of homozygous *shr* mutants expressing pSHR:SHR–GFP in WT, as well as in the *cpr5-1* mutant background. The E:S ratio was significantly reduced in *cpr5-1* compared to WT, consistent with a defect in facilitated SHR transport across PD (Figure 7D, E). Fluorescence recovery after photobleaching (FRAP) of nuclei in the root endodermis of homozygous *shr*/pSHR:SHR lines in *cpr5-1* was significantly lower compared to WT, further supporting that targeted transport across PD is reduced in *cpr5-1* (Figure 7F,G, Figure 7-figure supplement 1F). Notably, no significant difference in SHR–GFP fluorescence intensity was observed in the steles of WT when compared to *cpr5-1* lines (Figure 7-figure supplement 1E). The *cpr5* mutants showed no detectable defect in small molecule transport indicative of preservation of the capability to mediate small molecule transport as shown by 'Drop-ANd-See' *trans*-leaf diffusion assays (DANS, carboxyfluorescein: 376 Da; control CaMV*35S:PDLP5*; Figure 7H, I)(Lee et al., 2011). In summary, the intercellular transport assay results indicate that a callose-independent transport mechanism for macromolecules is defective in *cpr5* mutants. While consistent with a possible

contribution of NUPs to intercellular transport, we cannot exclude that the reduced transport is due to secondary effects in the *cpr5* mutants, which show rather severe phenotypic defects (Figure 5-figure supplement 1C, D).

Discussion

Based on the observations that (i) a substantial number of NUPs were identified in PD-enriched cell wall fractions, (ii) 12/35 known plant NUPs, including multiple FG-NUPs, localized to PD, and (iii) intercellular tandem-GFP and SHR transport was reduced in *cpr5* mutants could indicate that components of the NPC may generate a complex that can sustain a similar phase separation domain at PD as found in the NPC, and that phase separation generated by FG-NUPs may play a role in intercellular translocation (Kehlenbach et al., 2023). Previous studies had shown that cargo size cannot be the only criterion for cell-to-cell transport efficiency through PD (Alazem et al., 2025; Campbell et al., 2025; Howell et al., 2024; Kragler et al., 1998; Lee et al., 2003). The evidence for PD localization of NUPs obtained here is intriguing, as it may provide new potential explanations for the underlying mechanism of transport of certain mobile molecules (e.g. RNA-protein complexes) that are larger than the expected size exclusion limit (Tee and Faulkner, 2024). In this context the discovery of a new function of the nuclear transport receptor importin α4 as a PD-associated protein in mediating systemic infection of a plant virus in rice may further support the hypothesis of NPC-like transport functions (Lu et al., 2025).

Nuclear transport experiments using surface modified GFPs and analysis of the properties of nuclear transport receptors indicate that the phase separated domain generated by FG-NUPs in the permeation pathway of the NPC facilitates the transit of cargo that carry arginines, cysteines, histidines, and hydrophobic amino acids at their surface (Ejike et al., 2025; Frey et al., 2018). It will be very informative to test whether similar cargo surface properties are important for the transport through PD. Transport assays combined with pharmacological approaches using compounds such as hexanediol, which disrupt phase-separated domains, and systematic analyses of transport using surface-modified FPs of the same size (Frey et al., 2018; Ng et al., 2023) might help identifying phase separated domains at PD.

In summary we found three independent lines of evidence for the presence of NUPs at or near PD in the context of this work, based on subcellular localization, proteomics, and transport. However, all three independent lines could potentially be the result of artifacts. In particular, we found NUP localization at PD in overexpression conditions and, interestingly, also in stable transgenic Arabidopsis lines with presumably lower protein levels. However, NUP localization in the Arabidopsis lines at PD has only been observed in mature cotyledons and so far not in other tissues such as younger leaves or root. We can not exclude that in the NUP62-GFP lines, PD localization of NUPs is caused by elevated protein levels. Alternatively, it might be possible that localization of NUPs at PD occurs at (natively) elevated protein levels and/or depends on factors such as growth condition, pathogen infection and hormones, which were shown to influence mRNA levels of NUPs (Ascencio-Ibanez et al., 2008; Chen et al., 2012; Narsai et al., 2011; Okuma et al., 2014; Song et al., 2009). Interestingly, dynamic changes in subcellular localization of NUPs in response to environmental stimuli were reported previously, e.g., HOS1-GFP re-localizes from the periphery to the nucleoplasm after cold treatment (Lee et al., 2001). Perhaps the PD localization of NUPs is dynamic, occurring only under certain environmental conditions. To validate the subcellular localization, additional evidence is needed from stable transgenic lines with NUP fusions expressed under the control of the native promoter and terminator, complementing the NUP mutant background, and grown in different environmental conditions. Specific antisera raised against plant NUPs that are suitable for immunolocalization may help to clarify the subcellular localization of NUPs under native conditions. New insights may also be generated by cryo-electron tomography, for which recently suitable protocols have been established (Pöge et al., 2025). An alternative hypothesis that also implicates LLPS for the PD permeability barrier is based on the finding that the linker between the N-terminal C2A and C2B domains (C2A-B linker domain) of multiple C2 domains and transmembrane region proteins (MCTP) found in PD is predicted to be disordered and show strong intrinsic propensity for liquid-liquid phase separation (Dickmanns et al., 2025). Cryo-electron microcopy of plasmodesmata identified assemblies that decorate the desmotubule, which are likely formed by MCTPs, and which could then form an extended permeability barrier in the PD pore (Dickmanns et al., 2025).

366 There is evidence for NUPs to constitute a permeability barrier between cytoplasm and cilia (ciliary
367 transition zone) in animal cells (Blasius et al., 2019; del Viso et al., 2016; Gu et al., 2016; Takao et al.,
368 2017). However, the exact composition of the proposed ciliary pore complex and its anchoring at the
369 ciliary base remains a matter of debate, as cryo-ET structures of the ciliary base/ transition zone are not
370 yet available (Johnson and Malicki, 2019). Similarly, the assembly of NUPs at PD must differ from that
371 at the NPC because, as described above, desmotubules extend through the central channel of PD and the
372 cytoplasmic sleeve width at PD is smaller than the pore width at the NPC (Ejike et al., 2025; Mosalaganti
373 et al., 2022; Nicolas et al., 2017). The localization of the same NUPs at PD as well as nuclear pores is
374 unexpected, given that one would rather expect gene duplication and diversification to enable independent
375 regulation. Note that not all known NUPs were tested here, and some of those tested did not localize to
376 the PD. The structure, function and regulation of the predicted PD pore complex (PDPC) may differ from
377 that of the NPC.

378 NUPs seem to also play functional roles outside the NPC in animal cells: FG-NUPs were found in several
379 cyto- and nucleoplasmic membrane-less organelles, such as P-bodies, P-granules, stress granules, and
380 viral-associated organelles. In animals, annulate lamellae, preassembled NPCs in ER stacks, are
381 characteristic for rapidly dividing cells during germ cell development, early embryogenesis and
382 cancerogenic growth and might serve as storage place for NUPs (Kessel, 1992; Penzo and Palancade,
383 2023). AL have also been found in plant cells (Scheer and Franke, 1972). High NUP levels could result
384 in accumulation within AL. Missing an organellar marker for AL, we cannot exclude that fluorescent
385 puncta derived from NUP-FP fusions in our subcellular localization experiments indicate NUP
386 localization to AL. However, the arrangement of fluorescent puncta did not follow a stacking pattern,
387 which we would expect because of the stacked ER sheets in AL.

388 PD are challenging research subjects due to the embedding into the cell wall, and the presence of multiple
389 membranes. Based on the similarities between transport properties of PD and NPC, one may hypothesize
390 that they both use similar transport mechanisms. Further characterization will be required to explore
391 mechanisms for delivery of a diverse set of GFP-fused NUPs to PD, and to evaluate their localization and
392 trafficking, e.g. by immunolocalization. Alternatively, accumulation could serve as transient storage of
393 NPC complexes, or are a consequence of overaccumulation at the constriction of ER at PD entrances.

394 **Materials and Methods**

395 **<u>Plant materials and growth conditions</u>**

396 *Physcomitrium patens* (*P. patens*) ecotype Grandsen cultures were obtained from the *International Moss*
397 *Stock Center (IMSC)* (Freiburg). *P. patens* was cultured in liquid cultures of modified BCD medium as
398 described (Gombos et al., 2023). The BCD medium consisted of the following solutions which were
399 mixed prior to use: Solution B (0.1 mM $MgSO_4 \cdot 7H_2O$), Solution C (1.84 mM KH_2PO_4), Solution DK (1
400 M KNO_3), Solution DF (4.5 mM $FeSO_4 \cdot 7H_2O$), Trace Element Solution (TES) (614 mg H_3BO_3, 55 mg
401 $CuSO_4 \cdot 5H_20$, 28 mg KBr, 110 mg $Al_2(SO_4)3 \cdot K_2SO_4 \cdot 24H_20$, 389 mg $MnCl_2 \cdot 4H_20$, 55 mg $ZnSO_4 \cdot 7H_20$,
402 28mg LiCl, 10 mM $CoCl_2 \cdot 6H_20$, 28 mg KI and 28 mg $SnCl_2 \cdot 2H_20$ in 1 L H_20), 500 mM diammonium
403 tartrate and 1 M $CaCl_2$. For liquid cultures, 1% (m/v) glucose was added. For propagation of liquid
404 cultures, moss was homogenized and then transferred to 100 ml medium in a 250 ml. Cultures were
405 harvested after two weeks of growth at 21°C under long day conditions (16 h light/8 h dark) at
406 ~90 µmol m^{-2} sec^{-1}, 60% humidity.

407 Arabidopsis *cpr5-1* (G420D) mutant and *cpr5-T3* (SALK_074631) T-DNA insertion mutant were kindly
408 provided by Dr. Gu (University of California Berkeley) and Professor Chun-Hai Dong (Qingdao
409 Agricultural University), respectively (Bowling et al., 1994; Wang et al., 2017). Arabidopsis Col-0
410 *shr*/pSHR:SHR–GFP line was described before (Cui et al., 2007) and kindly gifted by Ikram Blilou,
411 KAUST. The pSHR:SHR–GFP/*cpr5-1* in the *shr* mutant background was generated by crossing, and
412 identified in the F2 segregating generation by sequencing of CPR5. For quantification of the SHR-GFP
413 endodermis-to-stele ratio, F5 seedlings of the Arabidopsis lines pSHR:SHR–GFP *cpr5-1* were grown on
414 a glass plate coated with ½ salt strength Murashige and Skoog (MS) media agar [half-strength Murashige
415 and Skoog basal salt mixture (Duchefa Biochemie, Haarlem, The Netherlands), 0.1 % (w/v) 2-(N-
416 morpholino)-ethanesulfonic acid, 1.5% agar, pH 5.6] (Dyachok et al., 2010) for 6 days in short day
417 conditions (10 h light, 14 h darkness), at 21°C with a light intensity to 130 µmol m^{-2} s^{-1}. For microparticle

418 bombardment assays and callose quantification, Arabidopsis Col-0, *cpr5-1,* and *cpr5-T3* plants were
419 grown on ½ MS plates in the same conditions as described above for 4 weeks. Nine independent stably
420 transformed homozygous Arabidopsis wildtype lines with single insertions for NUP62-GFP were used
421 for fluorescence imaging (T3 segregants; 3:1 segregation) and grown on ½ MS media supplemented with
422 1% (w/v) sucrose and 1% (w/v) agar in a growth chamber (16 h light/8 h darkness, 23 °C, 50 µmol m^{-2} s^{-}
423 ^{1}of white light, 60% humidity). For DANS assay, Arabidopsis WT and T-DNA insertion lines were grown
424 in soil with one plant per pot at 21°C under long day conditions (16 h light/8 h dark) for 3 weeks. For
425 analyses of the Arabidopsis shoot proteome, plants were grown in soil at 21°C under long day conditions
426 (16 h light/8 h dark) at ~90 µmol m^{-2} sec^{-1}, 60% humidity. Respective tissues were harvested after three
427 or five weeks. *Nicotiana benthamiana* (*N. benthamiana*) plants were grown individually in a pot under
428 controlled conditions (16 h light/8 h darkness, 26 °C, ~90 µmol m^{-2} s^{-1}, 60% humidity).

429 **DNA constructs**

430 For transient expression in *N. benthamiana*, the selected NUP open reading frames (ORFs) were cloned
431 into the binary pAB134-mVenus plasmid (Bleckmann et al., 2010). To generate the ORFs, total RNA was
432 extracted from Arabidopsis leaves using the RNeasy plant mini kit (Qiagen, Hilden, Germany), and
433 DNase I treatment was performed following the manufacturer's instructions. cDNA was then synthesized
434 using the Maxima H Minus First Strand cDNA synthesis kit (Thermo Fisher Scientific Inc., Waltham,
435 Massachusetts, USA). The ORFs were amplified, incorporating the Gateway attB sites, and purified PCR
436 products were cloned into pDONR221 using a BP clonase reaction (Thermo Fisher Scientific Inc.,
437 Waltham, Massachusetts, USA). *E. coli* Stellar cells (Takara Bio) were transformed with the resulting
438 entry vectors. Plasmids with the correct sequence were isolated and then recombined by LR reaction into
439 the binary plant expression vector pAB134-mVenus as C-terminal mVenus fusions under the control of a
440 β-estradiol-inducible promoter (Bleckmann et al., 2010). For localization of PpNUP35.1,
441 Pp3c6_16260V3 was amplified and cloned into the binary pAB134-mVenus plasmid. For SIM
442 experiments, XVE:CPR5-mCitrine and XVE:PDLP5-mScarlet3 were generated using GreenGate
443 (Lampropoulos et al., 2013). CPR5 and PDLP5 genomic sequences were amplified with primers including
444 *Bsa*I restriction sites and ligated to pGGC000 previously digested with *Bsa*I. Resulting vectors were used
445 to generate expression constructs using the GreenGate modules: XVE promoter (module A), CPR5 or
446 PDLP5 (module C), C-mCitrine or mScarlet3 (module D), HSP18.2-Terminator (module E), and the
447 pOLE1:OLE1-RFP seed coat selection marker (Shimada et al., 2010) (module F) were ligated to the
448 linearized binary vector pGGZ003.

449 Monomeric enhanced GFP (mEGFP) and 2xmEGFP sequences were amplified by PCR from plasmids
450 pENTR-R4R3-mEGFP-C (Addgene #113749) and pGGC025 (Addgene #48830), respectively, using
451 Gateway specific primers adding the attB1 and attB2 sites and cloned into pDONR221 by BP reaction
452 (Thermo Fisher Scientific Inc., Waltham, Massachusetts, USA). The resulting constructs, pDONR221-
453 mEGFP and pDONR221-2xmEGFP were used for LR reaction into the destination vector pGWB502
454 (Addgene #74844). The p35S:3xmCherry construct was generated using GreenGate by ligating the
455 modules Ca MV 35S promoter (Addgene #48815) (module A), 3xmCherry (Addgene #48831) (module
456 C), HSP18.2-Terminator (module E), and the pOLE1:OLE1-RFP seed coat selection marker (module F)
457 into the linearized binary vector pGGZ003. Topology localization of CPR5 was carried out using the split-
458 GFP system with the vectors kindly provided by Prof. Thordal-Christensen (University of Copenhagen)
459 (Xie et al., 2017). pDONR-CPR5 plasmid was recombined into pDest-GW-GFP11 and pDest-GFP11-
460 GW to generate either N- and C- fusions to the GFP 11th β-sheet using LR Gateway reactions (Thermo
461 Fisher Scientific Inc., Waltham, Massachusetts, USA). The GFP1-10 fragment was co-expressed with
462 either cytosolic localization (GFP1-10) or with ER-luminal localization (GFP1-10-HDEL). Plasmids
463 pEG100-35S:nYFP-CPR5, pEG100-35S:cYFP-CPR5 and pEG100-35S:NUP93a-cYFP used for homo-
464 and hetero-oligomerization were kindly gifted by Prof. Xinnian Dong (Duke University. North Carolina,
465 USA) (Gu et al., 2016). The nYFP fragment contains residues 1-172, and cYFP consists of residues 173-
466 238. A translational fusion NUP62-GFP construct was generated from a genomic clone of *NUP62*
467 (At2g45000), including a 1135-bp region 5'-upstream from the initiation ATG and a 407-bp region 3'-
468 downstream from the stop codon. mEGFP was fused to the NUP62 separated by a
469 GGGGSGGGGSGGGGS-linker (Shimozono and Miyawaki, 2008), just before the stop codon using
470 NEBuilder® HiFi DNA Assembly (NEB). The fluorescent protein-fusion construct was digested by *Not*I

471 and integrated into the pBIN40 binary vector (Miyashima et al., 2011). The final binary vectors were
472 introduced into *Agrobacterium tumefaciens* strain GV3101:pMP90 and used to carry out the
473 transformation of Arabidopsis. We confirmed the nucleotide sequences of all constructs using standard
474 DNA manipulation and sequencing techniques. Primers used in this study are listed in table S8.

475 **Transient expression in *N. benthamiana* leaves**

476 The *Agrobacterium tumefaciens* strain GV3101 (pMP90, pSOUP), containing the desired construct, was
477 cultured overnight, then diluted to 1/10 and grown until the culture reached an OD_{600} of 0.6-0.8. Cultures
478 were pelleted by centrifuge at 4000 rpm for 10 minutes. Bacteria were subsequently re-suspended in an
479 Infiltration Buffer comprising 0.01 M 2-(N-morpholino) ethanesulfonic acid (MES) at pH 5.6, 0.01 M
480 $MgCl_2$, and 150 µM acetosyringone at a final OD_{600} of 0.3. The *Agrobacterium* strain containing the
481 intended construct was then combined with an *Agrobacterium* strain containing the P19 silencing
482 suppressor (OD_{600} 0.1) (Qu and Morris, 2002). The resulting mixture was introduced into the leaves of 4-
483 week-old *N. benthamiana* plants through syringe infiltration. Two days after infiltration, gene expression
484 was induced by spraying infiltrated leaves with β-estradiol solution (20 µM β-estradiol, 0.1% v/v Tween-
485 20). Induction time was dependent on protein maturation times and ranged from 6 to 24 h. To test
486 localization of XVE:NUP43-mCitrine or XVE:CPR5-FP fusions at lower expression levels induction was
487 performed with 2 µM β-estradiol and induction times did not exceed 10 h (2 µM β-estradiol, 0.1% v/v
488 Tween-20).

489 For split-GFP assays, agrobacterial cultures were suspended in the Infiltration Buffer at a final OD_{600} of
490 0.3. *Agrobacterium* strains containing constructs split-GFP were co-infiltrated with the P19 silencing
491 suppressor (OD_{600} 0.1) into *N. benthamiana* leaves. For split-GFP assays either GFP11-CPR5 or CPR5-
492 GFP11 and GFP1-10 or GFP1-10-HDEL were co-infiltrated. Samples were imaged 2 days post
493 infiltration.

494 **Microscopy**

495 **Subcellular localization of FP fusions by confocal microcopy**

496 Confocal microscopy was performed on a Zeiss LSM 900 (Carl Zeiss, Oberkochen, Germany) equipped
497 with Airyscan GaAsP-PMT detectors and diode lasers using a 40x/1.20 water immersion objective (C-
498 Apochromat 40x/1.20 W Korr FCS). mCitrine or mVenus were excited with a 488 nm laser and emission
499 was collected in a 520-579 nm window. GFP was excited at 488 nm and collected in a 500-550 nm
500 window. mScarlet3 was excited at 561 nm and collected from 579-617 nm (Gadella et al., 2023). To
501 visualize pit fields, *N. benthamiana* leaves expressing a protein of interest were infiltrated with 0.1% (w/v)
502 aniline blue (Sigma Aldrich) solution and then imaged (excitation at 405 nm and 3-5% laser power,
503 emission detected in a 440-480 nm window). Free mScarlet3 was expressed and excited to visualize
504 cytoplasmic localization. Propidium iodide, a cell impermeant dye, stains the apoplasm when short
505 incubation times are used. Thus, for visualization of the cell wall, shortly before the experiment, PI was
506 pipetted on the object slide on the leaf disc (excitation 561 nm, 6% laser power, emission 574-617 nm).
507 Pit fields in cotyledons of 8-day old transgenic NUP62-GFP Arabidopsis seedlings were stained by
508 immersing leaves in 0.5% aniline blue in Sørensen's phosphate buffer [0.5% aniline blue (w/v) in 200
509 mM Sørensen's phosphate buffer prepared with Na_2HPO_4 and NaH_2PO_4 pH 8, Sigma-Aldrich, Saint
510 Louis, Missouri, USA)]. For confocal imaging of NUP62-GFP Arabidopsis lines, an Eclipse Ti2 inverted
511 microscope (Nikon) equipped with spinning disk confocal unit CSU-10 (Yokogawa) and a sCMOS
512 camera PRIME 95B (Photometrics, Tuscon, AZ, USA) was used. GFP was excited with a 488-nm laser,
513 and emission was collected with a 525/50-nm filter (Semrock, Rochester, New York). Images were taken
514 with a 100x oil-immersion lens (CFI Plan Apo Lambda 1.45 NA, Nikon).

515 **Structured Illumination Microscopy**

516 For structured illumination microscopy (SIM), only pit fields that were not deeply embedded in the plant
517 tissue and most proximal to the cover glass close to the objective, were observed. To do so, a *N.*
518 *benthamiana* leaf disk (2-mm diameter) was immersed in water and pressed between an object slide and
519 a high-precision coverslip (1.5H, 18 x 18 mm; A. Hartenstein) using a magnet. The sample chamber was
520 sealed with a flexible mounting adhesive (Fixo gum; Marabu). Z-stacks with a scaling of 149-nm steps
521 were obtained using an Elyra PS1 (Zeiss Microscopy GmbH, Oberkochen, Germany) equipped with a C-

522 Apochromat 63x/1.2 water-immersion M27 objective. Frame size was 512 x 512 pixels. PDLP5-
523 mScarlet3, CPR5-mCitrine, and aniline blue were excited with 561 nm, 488 nm, and 405 nm laser
524 wavelengths, respectively. Detection filters were set for the different channels: aniline blue: bandpass
525 (BP) 420–480/LP 750; CPR5-mCitrine: BP 495–570/LP 750; PDLP5-mScarlet3: BP 570-650/LP 655. In
526 initial control experiments with the Elyra PS1, we observed more puncta in the green channel after
527 excitation at 488 nm, after having used the 405 nm laser to excite aniline blue. These additional puncta in
528 the green channel precisely overlayed with the puncta observed in the aniline blue channel. The
529 identification of fluorescent puncta in this channel in response to excitation of aniline blue might be the
530 result of photoconversion to longer wavelengths. To exclude possible artifacts due to photoconversion of
531 the aniline blue, which could lead to emission in the channels used for detection of mCitrine, sequential
532 excitation was performed at 561, 488 and 405 nm. The grating periods (grid size) for structured
533 illumination were set to 34, 34, and 28 µm, respectively, for the three different laser wavelengths. The
534 number of grid rotations was set to 3 rotations. Camera exposure time ranged from 49-128 ms. The setup
535 was operated using Zeiss ZEN 2.3 SP1 software. An internal deconvolution program for SIM z-stacks
536 was used in 3D mode with maximum isotropy, zero sectioning, and the baseline shift active for all three
537 excitation channels. The noise filter was initially run in automatic mode, but was set to a unit below the
538 automatic setting for the actual processing.

539 **Callose quantification in Arabidopsis seedlings**

540 CPR5 is involved in the activation of pattern triggered immunity (PTI) and in the repression of effector-
541 triggered immunity (ETI) (Ma et al., 2023; Wang et al., 2014). The *cpr5-1* mutant had previously been
542 reported to show constitutive resistance to two virulent pathogens (Bowling et al., 1997). An important
543 plant defense mechanism against pathogens is induction of callose deposition at PD. Elevated callose
544 deposition in the *cpr5*-1 mutant after wounding has been reported (Kohler et al., 2002). To test whether
545 callose deposition was increased relative to WT under the growth and experimental conditions used here,
546 PD callose levels in WT and *cpr5-1* Arabidopsis seedlings were quantified. Leaf 5 of young seedlings (8-
547 12 leaf stage) was stained to minimize variability. Leaves were detached with a forceps, immersed in 1%
548 aniline blue diluted in water [1% aniline blue (w/v); Sigma-Aldrich, Saint Louis, Missouri, USA] and
549 infiltrated by applying a vacuum in a 20 ml syringe. Aniline blue fluorescence was observed on a Zeiss
550 LSM 900 (Zeiss Microscopy GmbH, Oberkochen, Germany) C-Apochromat 40x/1.20 W Korr FCS and
551 GaAsP-Pmt1 detector with excitation at 405 nm, 5% laser power and gain at 632 V. Emission was detected
552 from 400-500 nm. Imaging parameters were consistent across all experiments. Per experiment, 3-4 leaves
553 were assayed per genotype, 4 images were acquired per leaf. Four independent experiments were
554 performed for WT and 5 for *cpr5-1*. Mean aniline blue fluorescence intensity was quantified with Fiji
555 using the calloseQuant macro (calloseQuant settings: Method A, peak prominence = 55 and measurement
556 radius = 6) (Huang et al., 2022). Regions of Interest (ROIs) assigned to non-PD regions by the Fiji macro
557 were removed manually. Mean aniline blue fluorescence per image was plotted.

558 **<u>Plasmodesmatal proteome</u>**

559 **Preparation of *A. thaliana* plasmodesmatal (PD), cell wall (CW) and total cellular proteins (total**
560 **cell extract, TC) fractions**

561 Various Arabidopsis shoot tissues, including cauline leaves, meristem, and rosette leaves, were collected
562 individually. Each sample pool consisted of at least six plants. PD preparation involved a minimum of
563 three pools of the same tissue type. Tissues were freshly excised and promptly frozen in liquid nitrogen.
564 The PD preparation protocol was based on two previously published methods (Faulkner and Bayer, 2017;
565 Kraner et al., 2017). Each pool of samples was ground in liquid nitrogen and incubated in PD extraction
566 buffer [150 mM NaCl, 10 mM EDTA, 1 mM DTT, 1% (v/v) Triton X-100, 0.5% (v/v) sodium
567 deoxycholate, 0.1% (w/v) SDS, 10% (v/v) glycerol, and 100 mM Tris-HCl, pH 8] with 0.5% Protease
568 Inhibitor Cocktail (PIC, P9599, Sigma-Aldrich), 5 mM DTT, 1 mM PMSF, 50 mM NaF, 1 mM Na_3VO_4,
569 1 mM benzamidin and 4 µM leupeptin. For the cell wall fractions, two rounds of grinding in liquid
570 nitrogen efficiently removed soluble protein contaminants and better prepared cell walls for digestion.
571 The pellet was washed at least four times with a low concentration of detergents [150 mM NaCl, 10 mM
572 EDTA, 0.1% (v/v) Triton X-100, 10% (v/v) glycerol, and 100 mM Tris–HCl, pH 8]. After the last washing
573 step, the sample was centrifugated at 1500 x g at 4 °C with swing-out bucket (Sigma 3-30KS, Rotor 11390

574 & 13150). Cell wall fractions (CW; 100-200 µl) were collected from the final pellet. The rest of the CW
575 pellet was digested in cell wall digestion buffer (1.4% cellulase, mannitol 300mM, 10 mM $CaCl_2$, 10 mM
576 KCl) with 1 mM DTT and 0.5% PIC (P9599, Sigma-Aldrich) at room temperature for 1 h. After
577 centrifugation, the supernatant was collected and ultracentrifuged for 80 min at 4 °C and 110,000 x g
578 (Beckman XPN-80, Rotor SW41Ti). After ultracentrifugation, the resulting pellet was washed twice with
579 TBS buffer (2.5 mM KCl, 140 mM NaCl and 20 mM Tris-HCl, pH 7.4 with 0.5% PIC). The final pellet
580 was PD fraction (PD). Total protein (total cell extract, TC) was extracted according to He *et al*. (He et al.,
581 2022). All fractions were dissolved in 8M UTU (6 M urea, 2 M thiourea, Tris-HCl pH 8.0) before in-
582 solution tryptic digestion. For Arabidopsis cotyledon protein extraction and purification, cotyledons from
583 wild-type (Col-0) and NUP62-GFP single insertion transgenic lines were harvested and immediately
584 transferred to 1.5 ml microcentrifuge tubes. Samples were prepared in three biological replicates with two
585 technical replicates each. Tissue was homogenized in RIPA buffer and centrifuged at 14,000 × g for 15
586 min at 4°C. The resulting supernatant was carefully transferred to a fresh tube. For protein precipitation,
587 1/20 volume of 2.5 M sodium acetate (NaOAc, pH 5.0) was added, followed by 5 volumes of ice-cold
588 ethanol (EtOH). Samples were mixed by gentle inversion and incubated at room temperature (24°C) for
589 3 hr, then centrifuged at 21,000 × g for 20 min. The protein pellet was air-dried briefly and subsequently
590 resolubilized in UTU buffer (6 M urea, 2 M thiourea).

591 **Protein clean-up, trypsin digestion and peptide desalting**

592 A single-pot, solid-phase-enhanced, sample-preparation (SP3) technology (Hughes et al., 2019) with
593 trypsin digestion was used to remove the detergent in the protein extracts. Disulfide bridges were reduced
594 by an excess of DTT (6.5 mM), and alkylation of free cysteines was done by iodoacetamide (27 mM).
595 SpeedBead Magnetic Carboxylate Modified Particles (SP3 beads, 45152105050250 / 65152105050250,
596 GE Healthcare) were pre-washed by Milli-Q water. SP3 beads (50 µg/µl) were added to the protein sample
597 in a ratio of 1:10. 50% ethanol was used for inducing protein-bead binding. After incubating 15 min at 24
598 °C, 1,000 rpm constant shaking, the beads were washed three times with 80% ethanol and subjected to
599 trypsin digestion [100 mM Ammonium bicarbonate, trypsin (trypsin: protein ratio 1:100, V5113,
600 Promega)] for 12-14 h at 37 °C. Digested proteins were acidified to pH 2 using TFA and were then
601 desalted over C18 STAGE tips (Rappsilber et al., 2003).

602 **LC-MS/MS analysis of peptides**

603 Peptide mixtures were analyzed by HPLC system nanoflow Easy-nLC (Thermo Scientific, Waltham,
604 Massachusetts) and Orbitrap hybrid mass spectrometer (Q-exactive, Thermo Scientific). Peptides were
605 eluted from a 75 µm x 25 cm analytical C18 column (PepMan, Thermo Scientific) on a linear gradient
606 running from 5% to 90% acetonitrile over 70 min. Proteins were identified based on the information-
607 dependent acquisition of fragmentation spectra of multiple charged peptides. Up to ten data-dependent
608 MS/MS spectra were acquired in the linear ion trap for each full-scan spectrum acquired at 60,000 full-
609 width half-maximum (FWHM) resolution.

610 **Peptide and protein identification**

611 MaxQuant version 2.2.0.0 was used for raw file peak extraction and protein identification against the
612 Arabidopsis TAIR11 database (35,386 entries). The following parameters were applied: trypsin as
613 cleaving enzyme; minimum peptide length of six amino acids; maximal two missed cleavages;
614 carbamidomethylation of cysteine as a fixed modification; N-terminal protein acetylation, and oxidation
615 of methionine as variable modifications. Peptide mass tolerance was set to 20 ppm, and 0.5 Da was used
616 as the MS/MS tolerance. Multiplicity was set to 1. For label-free quantification, retention time matching
617 between runs was chosen within a time window of two minutes. iBAQ quantification was selected within
618 label-free quantification. The peptide false discovery rate (FDR) and the protein FDR were set to 0.01,
619 while site FDR was set to 0.05. Hits to contaminants (e.g. keratins) and reverse hits identified by
620 MaxQuant were excluded from further analysis. The mass spectrometry proteomics data have been
621 deposited to the ProteomeXchange Consortium via the PRIDE partner repository (Deutsch et al., 2020)
622 with the dataset identifier PXD049466.

623 **PD score (V1.5)**

624 The PD scoring (v1.5) was derived from the earlier PD score equation by Gombos *et al.* (Gombos et al.,
625 2023) with the modification that its components enrichment score and feature score were scaled between
626 0 and 1. The proteingroups.txt output from Maxquant was analyzed using Perseus. Protein iBAQ values
627 were normalized using z-scores, and the values for PD, CW, and TC fractions were averaged across tissues
628 (file S3). The ratios PD/CW and PD/TC were then calculated based on the average values obtained for
629 each fraction. The PD enrichment score for each protein is the sum of PD/CW and PD/TC. The score was
630 then scaled to a range of 0 to 1, based on the proportion of the distance to the minimum score. Regardless
631 of the enrichment score, the feature score relies on the frequency of protein functions, subcellular
632 localizations and PFAM domains (available at https://pfam.xfam.org/) identified within the high-
633 confidence dataset and validated PD candidates (Gombos et al., 2023; Johnston et al., 2023; Kirk et al.,
634 2022). Features of known PD proteins were extracted and weighted against the entire Arabidopsis
635 proteome. Structural features included Pfam domains PF00722 (GHL), PF06955 (XET_C), PF08372
636 (PRT_C), PF00335 (Tetraspanin), and PF00168 (C2 domain). Subcellular localization features included
637 plasma membrane (PM), endoplasmic reticulum (ER), extracellular space (EX), and cell wall (CW).
638 Functional features were assigned according to MapMan categories bin 10, 15, 26, and 30. Similar to the
639 enrichment score, the feature score was also normalized to a scale from 0 to 1, based on the proportion of
640 the distance to the minimum score across all *Arabidopsis* proteins (30843 entries). For each protein, the
641 PD score (v 1.5) is obtained by summing the transformed PD enrichment score and the feature score,
642 resulting in a range from 0 to 2. A higher PD score (1.5) indicates a greater likelihood that the protein is
643 a PD protein.

644 **<u>Intercellular Transport assays</u>**

645 **Microparticle bombardment**

646 To test passive diffusion of 2xEGFP, microparticle bombardment was performed to deliver DNA coated
647 gold microcarriers into single epidermal cells. 60 mg of 1.0 µm gold microcarriers (Bio-Rad Laboratories,
648 Hercules, CA, USA) were added into a 1.5-mL microcentrifuge tube and washed with 70% ethanol before
649 use. After the final washing step, 1 mL of 50% glycerol was added, and the tube was sealed using
650 Parafilm® (Amcor). The suspended gold particles (35 µL) were labelled with 2 – 2.5 µg of plasmid DNA
651 (pGWB502-p35S:2xmEGFP) in the presence of 0.1 M spermidine and 2.5 M $CaCl_2$. Tubes were vortexed
652 for 1 min and put on ice for 1 min. Coated gold particles were centrifuged at 1,500 x g for 30 sec. The
653 particles were washed twice with 70% ethanol. After the second washing step, 35 µL of 100% ethanol
654 was added and vortexed until the pellet completely dispersed. This gold suspension (10 µL) was
655 transferred onto a macrocarrier (Bio-Rad Laboratories, Hercules, CA, USA). Bombardment was
656 performed using the PDS-1000/He Biolistic Particle Delivery System (Bio-Rad, #1652257) as described
657 (Tee et al., 2022). To visualize bombardments, 2xmEGFP was excited with a 488-nm laser and emission
658 detected at 495-548 nm, while 3xmCherry was excited with a 561-nm laser and emission detected at 548-
659 617 nm. Cells showing fluorescence in the GFP channel were counted manually on maximum projections.
660 To identify the initially bombarded cell, Arabidopsis leaves were bombarded with gold particles coated
661 with pGWB502-p35S:3xmCherry (84 kDa, unable to move passively through non-specific trafficking)
662 and pGWB502-p35S:2xmEGFP. Fluorescence intensity profile plots across transects were generated
663 using Fiji software package (Schindelin et al., 2012) to analyze the correlation of the fluorescence
664 intensity of mCherry (bombarded cell) and mEGFP (Figure 7-figure supplement 1).

665 **SHR-GFP endodermis-to-stele ratio and Fluorescence Recovery After Photobleaching (FRAP)**
666 **analysis**

667 SHR–GFP was detected in root endodermis and stele using a Zeiss LSM 900 equipped with Airyscan
668 GaAsP-PMT detectors and diode lasers using a C-Apochromat 40x/1.20 W Korr FCS water objective.
669 For quantification of SHR-GFP, a brief Z-stack series of up to 60 sections of short intervals (2.1 µm)
670 around the ROI were captured, and the Sum-Projection of the volume was analyzed using ImageJ. The
671 background fluorescence was subtracted from the average pixel intensity in the circled region in the
672 endodermis (E) and from the average pixel intensity of the corresponding boxed region in the stele (S)
673 (see Figure 7D). The ratio between endodermis and corresponding stele region was calculated (E:S).
674 Multiple samples were taken for each root to determine the average ratio.

675 The SHR–GFP fluorescence was bleached in endodermal cells using the 488 nm laser at full laser power
676 for 150 iterations, which lead to around 50-70% reduction in fluorescence. 1-3 cells in the same cell layer
677 were bleached at the same time for each root. To acquire recovery images, laser power was set to 2% to
678 avoid bleaching. The recovery images of the bleached areas were captured every 20 min to reduce the
679 possibility of additional bleaching from frequent scanning. To ensure the identification of the same region
680 of interest during the time-course imaging, a brief Z-stack series of up to 60 sections with short interval
681 (2.1µm) around the region of interest were captured. In this way, the same region should be included in
682 the series of images and can be re-tracked later for analysis. For each time point the Sum-Projection of
683 the same volume was analyzed. The background subtracted fluorescence intensity ratio (endodermis
684 bleached nucleus/endodermis control nucleus) before bleach, after bleach and after 60 minutes was
685 determined using ImageJ (see also Figure 7-figure supplement 1F for positions of ROIs). Time 0 post-
686 bleach fluorescence was set to 0 and all measurements were normalized to this point by subtracting the
687 time 0 post-bleach fluorescence signal from all of the pre-bleach and the recovery values. The percent
688 recovery was calculated using the normalized values. For analysis of intracellular FRAP, a frame size of
689 512 × 512 pixels with a scanning speed of 0.93 ms per frame (1 Hz) and bi-directional scanning was used
690 to accelerate the scanning rate for each frame.

691 **DANS assay**

692 For Drop-ANd-See (DANS) assays, 1 µl of 10 mM 5-(and 6)-carboxy-fluoresceindiacetat-
693 acetoxymethylester (CFDA) in 0.002 % Silwet® was pipetted on the adaxial side of a rosette leaf and
694 removed after 5 min. The 4th and 24 h later also the 5th rosette leaf was used. For microscopy, the leaf was
695 cut off, washed in water, and mounted between two cover slips. Fluorescence was observed under an Axio
696 Zoom.V16 (Zeiss Microscopy GmbH, Oberkochen, Germany) equipped with a X-Cite Xylts (Excelitas
697 Technologies, PA, USA) LED light source, using a GFP broad bandpass filter cube (excitation: 470/40
698 nm, beam splitter: FT495 nm, emission: 525/50 nm). Images of the adaxial- and abaxial side were taken
699 using Orca-fusionBT digital camera (C15440, Hamamatsu, Japan). Imaging parameters were consistent
700 across experiments. To identify the fluorescent area, thresholding was performed in ImageJ with the same
701 threshold value for adaxial-and abaxial sides. The diffusion is quantified by ratio between the area above
702 the intensity threshold on the abaxial side and the adaxial side. Experiments of the same day were
703 normalized to the WT experiments of the same day.

704 **<u>Bioinformatics</u>**

705 **FG repeat analysis**

706 To identify FG repeat proteins, *A. thaliana* and *P. patens* peptides encoded by gene models were
707 downloaded from Araport 11 and Phypa_V3 genomes and screened, respectively. FG occurrences were
708 counted in a sliding window of 200 amino acids (aa), and the maximum number of FG repeats per window
709 was determined using a custom python script (Supplementary Script 1 and 2). Within the same script, the
710 number of GLFG and xFxFG motifs in each peptide were counted (table S1).

711 **PD index quantification**

712 Overlay of fluorescence from NUP-FPs and aniline blue was quantitatively scored using the PD index
713 (Grison et al., 2019). To minimize bias in quantification, we employed our recently developed PD index
714 script (Gombos et al., 2023). Briefly, clear PD sites were cropped, and channels were separated. PD were
715 identified using auto threshold and Fiji YEN-algorithm, with user modifications. Center coordinates of
716 PD were determined, and square ROIs were set. The PD index was calculated by dividing mean intensity
717 values of PD ROIs by background ROI values. Background ROIs were defined as areas of weak aniline
718 blue fluorescence. Regions previously recognized as PD were automatically omitted from the positioning
719 of background ROIs. Image processing was used for background ROI placement. The software Igor Pro
720 (version 9) was used for data plotting and SPSS was used for statistical analyses.

721 **Structure prediction for CPR5**

722 The structure of CPR5 was predicted using Alphafold monomer version 2.3.1 (Jumper et al., 2021).

723 **<u>Phylogenetic analyses</u>**

The tree shown in Figure 6-figure supplement 2 was generated from 68 amino acid sequences as listed in table S7. Full-length sequences were imported into the Molecular Evolutionary Genetics Analysis (MEGA) package version 11, and aligned by CLUSTALW (Tamura et al., 2021). All positions with at least 85% site coverage were used. Phylogenetic analyses were conducted using the Maximum Likelihood method. Based on the suggestions of the "find best protein model (ML)" tool in MEGA 11, the lower BIC (Bayesian Information Criterion) model was selected, which was the JTT matrix-based model (Jones et al., 1992). A discrete Gamma distribution was used to model evolutionary rate differences among sites (five categories, +G, parameter = 6.413). Initial trees for the heuristic search were obtained automatically by applying Neighbor-Joining and BioNJ algorithms to a matrix of pairwise distances estimated using the JTT model, and then selecting the topology with a superior log likelihood value. The bootstrap consensus tree inferred from 1000 replicates was taken to represent the evolutionary history of the analyzed genes. Branches corresponding to partitions reproduced in less than 50% bootstrap replicates were collapsed.

Statistics

In the PD proteome from Arabidopsis leaf tissue, we identified 5145 proteins from PD, CW, and TC fractions, with 3347 proteins having a PD score > 0.63. Among them, 3062 proteins were quantifiable in the PD fraction, constituting our Arabidopsis shoot PD proteome. Among these, 2268 proteins were categorized as high-confidence PD proteins, while 792 proteins fall into the medium-confidence category (file S3). The PD index is based on the analysis of at least 15 images from three independent repeats for each NUP and negative control. The quantification of the intercellular spread of 2xmEGFP by counting fluorescent cells in the mEGFP channel is based on the analysis of $n_{(WT)} = 17$ independent biological experiments with in total 594 bombarded cells; $n_{(cpr5\text{-}1)} = 6$ independent biological replicates with in total 278 bombarded cells; $n_{(cpr5\text{-}T3)} = 4$ independent biological replicates with in total 99 bombarded cells. Kruskal-Wallis test with Bonferroni-corrected Dunn´s test for pairwise comparison was used to test for significant differences in mean cell counts between WT, *cpr5-1*, and *cpr5-T3* with $p_{(WT\ vs.\ cpr5\text{-}1)} < 1x10^{-10}$, $p_{(WT\ vs.\ cpr5\text{-}T3)} = 0.025$, and $p_{(cpr5\text{-}1\ vs.\ cpr5\text{-}T3)} = 0.00005$. The *p*-values are summarized in table S2. The callose quantification is based on $n_{(WT)} = 4$ independent experiments, $n_{(cpr5\text{-}1)} = 5$ independent experiments. Student´s *t*-test indicated a non-significant difference with $p = 0.48$.

SHR-GFP endodermis-to-stele ratio is based on the quantification of $n_{(WT)} = 62$ and $n_{(cpr5\text{-}1)} = 62$ different endodermis nuclei and corresponding stele regions, while per root 3-4 different nuclei and corresponding stele regions were quantified. For endodermis-to-stele ratio, Mann-Whitney U test indicated a significant difference between WT and *cpr5-1* background with $p = 0.0006$. For baseline stele fluorescence, Mann-Whitney U test indicated no significant differences between s*hr* and s*hr x cpr5-1* with $p = 0.074$. The quantification of SHR-GFP fluorescence recovery was normalized to a control nucleus in the endodermis (see Methods and Figure 7-figure supplement 1F) and is based on n(WT) = 59 and n(*cpr5-1*) = 59 bleached nuclei, while per root 3-4 nuclei were bleached. Student´s T-Test indicated a significant difference between WT and *cpr5-1* background with p = 0.037.

For the DANS data, Kruskal-Wallis test with Bonferroni-corrected Dunn´s test for pairwise comparison was used to test for significant differences between WT and mutant lines. All statistical test were performed with SPSS. In all box plots median is represented by vertical line inside the box, mean is represented by the bold +. Values between quartiles 1 and 3 are represented by box ranges, and 5th and 95th percentile are represented by error bars. Data was plotted using Igor Pro (version 9).

References

Alazem M, Nuzzi SN, Burch-Smith TM. 2025. Viral Movement Proteins and Plasmodesmata: turning gatekeepers into gateways. Journal of Experimental Botany eraf184. DOI: https://doi.org/10.1093/jxb/eraf184

Apelt L, Knockenhauer KE, Leksa NC, Benlasfer N, Schwartz TU, Stelzl U. 2016. Systematic protein–protein interaction analysis reveals intersubcomplex contacts in the Nuclear Pore Complex. Molecular & Cellular Proteomics : MCP **15**:2594–2606. DOI: https://doi.org/10.1074/mcp.M115.054627, PMID: 27194810

Arra Y, Auguy F, Stiebner M, Chéron S, Wudick MM, Miras M, Schepler-Luu V, Köhler S, Cunnac S, Frommer WB, Albar L. 2024. Rice Yellow Mottle Virus resistance by genome editing of the

775 *Oryza sativa L. ssp. japonica* nucleoporin gene *OsCPR5.1* but not *OsCPR5.2*. Plant
776 Biotechnology Journal **22**:1299–1311. DOI: https://doi.org/10.1111/pbi.14266, PMID: 38124291

777 Ascencio-Ibanez JT, Sozzani R, Lee TJ, Chu TM, Wolfinger RD, Cella R, Hanley-Bowdoin L. 2008.
778 Global analysis of Arabidopsis gene expression uncovers a complex array of changes impacting
779 pathogen response and cell cycle during geminivirus infection. Plant Physiology **148**:436–54.
780 DOI: https://doi.org/10.1104/pp.108.121038

781 Bayer EM, Bottrill AR, Walshaw J, Vigouroux M, Naldrett MJ, Thomas CL, Maule AJ. 2006. Arabidopsis
782 cell wall proteome defined using multidimensional protein identification technology. Proteomics
783 **6**:301–311. DOI: https://doi.org/10.1002/pmic.200500046

784 Blasius TL, Takao D, Verhey KJ. 2019. NPHP proteins are binding partners of nucleoporins at the base
785 of the primary cilium. PLOS ONE **14**:e0222924. DOI:
786 https://doi.org/10.1371/journal.pone.0222924

787 Bleckmann A, Weidtkamp-Peters S, Seidel CA, Simon R. 2010. Stem cell signaling in Arabidopsis
788 requires CRN to localize CLV2 to the plasma membrane. Plant Physiology **152**:166–76. DOI:
789 https://doi.org/10.1104/pp.109.149930

790 Bowling SA, Clarke JD, Liu Y, Klessig DF, Dong X. 1997. The cpr5 mutant of Arabidopsis expresses
791 both NPR1-dependent and NPR1-independent resistance. The Plant Cell **9**:1573–84.

792 Bowling SA, Guo A, Cao H, Gordon AS, Klessig DF, Dong X. 1994. A mutation in Arabidopsis that
793 leads to constitutive expression of systemic acquired resistance. The Plant Cell **6**:1845–5187.

794 Brault ML, Petit JD, Immel F, Nicolas WJ, Glavier M, Brocard L, Gaston A, Fouché M, Hawkins TJ,
795 Crowet J-M, Grison MS, Germain V, Rocher M, Kraner M, Alva V, Claverol S, Paterlini A,
796 Helariutta Y, Deleu M, Lins L, Tilsner J, Bayer EM. 2019. Multiple C2 domains and
797 transmembrane region proteins (MCTPs) tether membranes at plasmodesmata. EMBO reports
798 **20**:e47182. DOI: https://doi.org/10.15252/embr.201847182, PMID: 31286648

799 Campbell R, Cowan G, Wurzinger B, Ducreux LJM, Dessoly J, Guo W, Zhang R, Morris JA, Hedley P,
800 Wahl V, Taylor MA, Hancock RD. 2025. GERMIN3 regulates tuber initiation and axillary bud
801 activation by facilitating plasmodesmatal gating. The Plant Journal **122**:e70186. DOI:
802 https://doi.org/10.1111/tpj.70186

803 Chen C-C, Fu S-F, Lee Y-I, Lin C-Y, Lin W-C, Huang H-J. 2012. Transcriptome analysis of age-related
804 gain of callus-forming Capacity in Arabidopsis hypocotyls. Plant and Cell Physiology **53**:1457–
805 1469. DOI: https://doi.org/10.1093/pcp/pcs090

806 Chen G, Xu D, Liu Q, Yue Z, Dai B, Pan S, Chen Y, Feng X, Hu H. 2023. Regulation of FLC nuclear
807 import by coordinated action of the NUP62-subcomplex and importin β SAD2. Journal of
808 Integrative Plant Biology **65**:2086–2106. DOI: https://doi.org/10.1111/jipb.13540

809 Chopra K, Bawaria S, Chauhan R. 2019. Evolutionary divergence of the nuclear pore complex from fungi
810 to metazoans. Protein Science **28**:571–586. DOI: https://doi.org/10.1002/pro.3558

811 Collins PP, Broad RC, Yogeeswaran K, Varsani A, Poole AM, Collings DA. 2023. Characterisation of
812 the trans-membrane nucleoporins GP210 and NDC1 in *Arabidopsis thaliana*. Plant Science
813 **332**:111719. DOI: https://doi.org/10.1016/j.plantsci.2023.111719

814 Craige B, Tsao C-C, Diener DR, Hou Y, Lechtreck K-F, Rosenbaum JL, Witman GB. 2010. CEP290
815 tethers flagellar transition zone microtubules to the membrane and regulates flagellar protein
816 content. The Journal of Cell Biology **190**:927–940. DOI: https://doi.org/10.1083/jcb.201006105,
817 PMID: 20819941

818 Crawford KM, Zambryski PC. 2001. Non-targeted and targeted protein movement through
819 plasmodesmata in leaves in different developmental and physiological states. Plant Physiology
820 **125**:1802–1812.

821 Crawford KM, Zambryski PC. 2000. Subcellular localization determines the availability of non-targeted
822 proteins to plasmodesmatal transport. Current Biology **10**:1032–1040. DOI:
823 https://doi.org/10.1016/S0960-9822(00)00657-6, PMID: 10996070

824 Cui H, Levesque MP, Vernoux T, Jung JW, Paquette AJ, Gallagher KL, Wang JY, Blilou I, Scheres B,
825 Benfey PN. 2007. An evolutionarily conserved mechanism delimiting SHR movement defines a
826 single layer of endodermis in plants. Science **316**:421–5. DOI:
827 https://doi.org/10.1126/science.1139531

828 del Viso F, Huang F, Myers J, Chalfant M, Zhang Y, Reza N, Bewersdorf J, Lusk CP, Khokha MK. 2016.
829 Congenital heart disease genetics uncovers context-dependent organization and function of
830 nucleoporins at cilia. Developmental Cell **38**:478–492. DOI:
831 https://doi.org/10.1016/j.devcel.2016.08.002

832 Deutsch EW, Bandeira N, Sharma V, Perez-Riverol Y, Carver JJ, Kundu DJ, García-Seisdedos D,
833 Jarnuczak AF, Hewapathirana S, Pullman BS, Wertz J, Sun Z, Kawano S, Okuda S, Watanabe Y,
834 Hermjakob H, MacLean B, MacCoss MJ, Zhu Y, Ishihama Y, Vizcaíno JA. 2020. The
835 ProteomeXchange consortium in 2020: enabling "big data" approaches in proteomics. Nucleic
836 Acids Research **48**:D1145–D1152. DOI: https://doi.org/10.1093/nar/gkz984, PMID: 31686107

837 Dickmanns M, Pöge M, Xu P, Gombos S, Miras M, Plitzko JM, Simon R, Schulze WX, Frommer WB,
838 Baumeister W. 2025. *In situ* architecture of plasmodesmata suggests mechanisms controlling
839 intercellular exchange. bioRxiv.

840 Dyachok J, Yoo C-M, Palanichelvam K, Blancaflor EB. 2010. Sample preparation for fluorescence
841 imaging of the cytoskeleton in fixed and living plant roots. In: Gavin RH (Ed). *Cytoskeleton*
842 *Methods and Protocols*, Methods in Molecular Biology. Humana Press. p. 157–169. DOI:
843 https://doi.org/10.1007/978-1-60761-376-3_8

844 Ejike JO, Davis GV, Restrepo-Escobar A, Dalal A, Nakamura M, Frommer WB, Schladt TM. 2025. The
845 role of phase separation for RNA and protein transport through the nuclear pore complex. J. Exp.
846 Bot. eraf271. DOI: https://doi.org/10.1093/jxb/eraf271

847 Epting D, Decker E, Ott E, Eisenberger T, Bader I, Bachmann N, Bergmann C. 2022. The ciliary transition
848 zone protein TMEM218 synergistically interacts with the NPHP module and its reduced dosage
849 leads to a wide range of syndromic ciliopathies. Human Molecular Genetics **31**:2295–2306. DOI:
850 https://doi.org/10.1093/hmg/ddac027

851 Faulkner C, Akman OE, Bell K, Jeffree C, Oparka K. 2008. Peeking into pit fields: a multiple twinning
852 model of secondary plasmodesmata formation in tobacco. The Plant Cell **20**:1504–1518. DOI:
853 https://doi.org/10.1105/tpc.107.056903, PMID: 18667640

854 Faulkner C, Bayer EM. 2017. Isolation of plasmodesmata. Methods in Molecular Biology **1511**:187–198.
855 DOI: https://doi.org/10.1007/978-1-4939-6533-5_15

856 Faulkner C, Petutschnig E, Benitez-Alfonso Y, Beck M, Robatzek S, Lipka V, Maule AJ. 2013. LYM2-
857 dependent chitin perception limits molecular flux via plasmodesmata. Proceedings of the National
858 Academy of Sciences **110**:9166–9170. DOI: https://doi.org/10.1073/pnas.1203458110

859 Fernandez-Calvino L, Faulkner C, Walshaw J, Saalbach G, Bayer EM, Benitez-Alfonso Y, Maule AJ.
860 2011. Arabidopsis plasmodesmal proteome. PloS One **6**:e18880. DOI:
861 https://doi.org/10.1371/journal.pone.0018880, PMID: 21533090

862 Fitzgibbon J, Bell K, King E, Oparka K. 2010. Super-resolution imaging of plasmodesmata using three-
863 dimensional structured illumination microscopy. Plant Physiology **153**:1453–63. DOI:
864 https://doi.org/10.1104/pp.110.157941

865 Frey S, Rees R, Schünemann J, Ng SC, Fünfgeld K, Huyton T, Görlich D. 2018. Surface properties
866 determining passage rates of proteins through nuclear pores. Cell **174**:202-217.e9. DOI:
867 https://doi.org/10.1016/j.cell.2018.05.045

868 Gadella TWJ, van Weeren L, Stouthamer J, Hink MA, Wolters AHG, Giepmans BNG, Aumonier S,
869 Dupuy J, Royant A. 2023. mScarlet3: a brilliant and fast-maturing red fluorescent protein. Nature
870 Methods **20**:541–545. DOI: https://doi.org/10.1038/s41592-023-01809-y

871 Gallemí M, Galstyan A, Paulišić S, Then C, Ferrández-Ayela A, Lorenzo-Orts L, Roig-Villanova I, Wang
872 X, Micol JL, Ponce MR, Devlin PF, Martínez-García JF. 2016. DRACULA2 is a dynamic
873 nucleoporin with a role in regulating the shade avoidance syndrome in Arabidopsis. Development
874 **143**:1623–1631. DOI: https://doi.org/10.1242/dev.130211

875 Giordano F, Saheki Y, Idevall-Hagren O, Colombo SF, Pirruccello M, Milosevic I, Gracheva EO,
876 Bagriantsev SN, Borgese N, De Camilli P. 2013. PI(4,5)P_2-dependent and Ca^{2+}-regulated ER-PM
877 interactions mediated by the extended synaptotagmins. Cell **153**:1494–1509. DOI:
878 https://doi.org/10.1016/j.cell.2013.05.026, PMID: 23791178

879 Gombos S, Miras M, Howe V, Xi L, Pottier M, Kazemein Jasemi NS, Schladt M, Ejike JO, Neumann U,
880 Hänsch S, Kuttig F, Zhang Z, Dickmanns M, Xu P, Stefan T, Baumeister W, Frommer WB,
881 Simon R, Schulze WX. 2023. A high-confidence *Physcomitrium patens* plasmodesmata proteome
882 by iterative scoring and validation reveals diversification of cell wall proteins during evolution.
883 New Phytologist **238**:637–653. DOI: https://doi.org/10.1111/nph.18730

884 Grison MS, Kirk P, Brault ML, Wu XN, Schulze WX, Benitez-Alfonso Y, Immel F, Bayer EM. 2019.
885 Plasma membrane-associated receptor-like kinases relocalize to plasmodesmata in response to
886 osmotic stress. Plant Physiology **181**:142–160. DOI: https://doi.org/10.1104/pp.19.00473, PMID:
887 31300470

888 Gu Y, Zebell SG, Liang Z, Wang S, Kang B-H, Dong X. 2016. Nuclear pore permeabilization is a
889 convergent signaling event in effector-triggered immunity. Cell **166**:1526-1538.e11. DOI:
890 https://doi.org/10.1016/j.cell.2016.07.042, PMID: 27569911

891 He M, Wang J, Herold S, Xi L, Schulze WX. 2022. A rapid and universal workflow for label-free-
892 quantitation-based proteomic and phosphoproteomic studies in cereals. Current Protocols **2**:e425.
893 DOI: https://doi.org/10.1002/cpz1.425

894 Hodel AE, Hodel MR, Griffis ER, Hennig KA, Ratner GA, Xu S, Powers MA. 2002. The three-
895 dimensional structure of the autoproteolytic, nuclear pore-targeting domain of the human
896 nucleoporin Nup98. Molecular Cell **10**:347–358. DOI: https://doi.org/10.1016/S1097-
897 2765(02)00589-0

898 Hoogenboom BW, Hough LE, Lemke EA, Lim RYH, Onck PR, Zilman A. 2021. Physics of the nuclear
899 pore complex: Theory, modeling and experiment. Physics Reports **921**:1–53. DOI:
900 https://doi.org/10.1016/j.physrep.2021.03.003, PMID: 35892075

901 Howell AH, Christensen AH, James V, Vasina VV, Jensen KH, Foley J, Evans JE, Stone HA, Peters WS,
902 Knoblauch M. 2024. Electric charge controls plasmodesma conductivity. DOI:
903 https://doi.org/10.1101/2024.04.02.587779

904 Huang C, Mutterer J, Heinlein M. 2022. In vivo aniline blue staining and semiautomated quantification
905 of callose deposition at plasmodesmata. In: Benitez-Alfonso Y, Heinlein M (Eds).
906 *Plasmodesmata: Methods and Protocols*, Methods in Molecular Biology. Springer US. p. 151–
907 165. DOI: https://doi.org/10.1007/978-1-0716-2132-5_9

908 Hughes CS, Moggridge S, Müller T, Sorensen PH, Morin GB, Krijgsveld J. 2019. Single-pot, solid-phase-
909 enhanced sample preparation for proteomics experiments. Nature Protocols **14**:68–85. DOI:
910 https://doi.org/10.1038/s41596-018-0082-x, PMID: 30464214

911 Johnson CA, Malicki JJ. 2019. The nuclear arsenal of cilia. Developmental Cell **49**:161–170. DOI:
912 https://doi.org/10.1016/j.devcel.2019.03.009

913 Johnston MG, Breakspear A, Samwald S, Zhang D, Papp D, Faulkner C, de Keijzer J. 2023. Comparative
914 phyloproteomics identifies conserved plasmodesmal proteins. Journal of Experimental Botany
915 **74**:1821–1835. DOI: https://doi.org/10.1093/jxb/erad022, PMID: 36639877

Jones DT, Taylor WR, Thornton JM. 1992. The rapid generation of mutation data matrices from protein sequences. Bioinformatics **8**:275–282. DOI: https://doi.org/10.1093/bioinformatics/8.3.275

Jumper J, Evans R, Pritzel A, Green T, Figurnov M, Ronneberger O, Tunyasuvunakool K, Bates R, Žídek A, Potapenko A, Bridgland A, Meyer C, Kohl SAA, Ballard AJ, Cowie A, Romera-Paredes B, Nikolov S, Jain R, Adler J, Back T, Petersen S, Reiman D, Clancy E, Zielinski M, Steinegger M, Pacholska M, Berghammer T, Bodenstein S, Silver D, Vinyals O, Senior AW, Kavukcuoglu K, Kohli P, Hassabis D. 2021. Highly accurate protein structure prediction with AlphaFold. Nature **596**:583–589. DOI: https://doi.org/10.1038/s41586-021-03819-2, PMID: 34265844

Kehlenbach RH, Neumann P, Ficner R, Dickmanns A. 2023. Interaction of nucleoporins with nuclear transport receptors: a structural perspective. Biological Chemistry **404**:791–805. DOI: https://doi.org/10.1515/hsz-2023-0155

Kessel RG. 1992. Annulate lamellae: a last frontier in cellular organelles. In: Jeon KW, Friedlander M (Eds). *Int. Rev. Cytol.* Academic Press. p. 43–120. DOI: https://doi.org/10.1016/S0074-7696(08)61858-6

Kirk P, Amsbury S, German L, Gaudioso-Pedraza R, Benitez-Alfonso Y. 2022. A comparative meta-proteomic pipeline for the identification of plasmodesmata proteins and regulatory conditions in diverse plant species. BMC biology **20**:128. DOI: https://doi.org/10.1186/s12915-022-01331-1, PMID: 35655273

Kohler A, Schwindling S, Conrath U. 2002. Benzothiadiazole-induced priming for potentiated responses to pathogen infection, wounding, and infiltration of water into leaves requires the *NPR1/NIM1* gene in Arabidopsis. Plant Physiology **128**:1046–1056. DOI: https://doi.org/10.1104/pp.010744

Koizumi K, Hayashi T, Wu S, Gallagher KL. 2012. The SHORT-ROOT protein acts as a mobile, dose-dependent signal in patterning the ground tissue. Proceedings of the National Academy of Sciences of the United States of America **109**:13010–13015. DOI: https://doi.org/10.1073/pnas.1205579109, PMID: 22826238

Kragler F, Monzer J, Shash K, Xoconostle-Cázares B, Lucas WJ. 1998. Cell-to-cell transport of proteins: Requirement for unfolding and characterization of binding to a putative plasmodesmal receptor. Plant Journal **15**:367–381. DOI: https://doi.org/10.1046/j.1365-313X.1998.00219.x

Kraner ME, Müller C, Sonnewald U. 2017. Comparative proteomic profiling of the choline transporter-like1 (CHER1) mutant provides insights into plasmodesmata composition of fully developed *Arabidopsis thaliana* leaves. The Plant Journal: For Cell and Molecular Biology **92**:696–709. DOI: https://doi.org/10.1111/tpj.13702, PMID: 28865150

Lampropoulos A, Sutikovic Z, Wenzl C, Maegele I, Lohmann JU, Forner J. 2013. GreenGate - a novel, versatile, and efficient cloning system for plant transgenesis. PLOS ONE **8**:e83043. DOI: https://doi.org/10.1371/journal.pone.0083043

Lee H, Xiong L, Gong Z, Ishitani M, Stevenson B, Zhu J-K. 2001. The Arabidopsis HOS1 gene negatively regulates cold signal transduction and encodes a RING finger protein that displays cold-regulated nucleo–cytoplasmic partitioning. Genes & Development **15**:912–924. DOI: https://doi.org/10.1101/gad.866801, PMID: 11297514

Lee JH, Kim JJ, Kim SH, Cho HJ, Kim J, Ahn JH. 2012. The E3 ubiquitin ligase HOS1 regulates low ambient temperature-responsive flowering in *Arabidopsis thaliana*. Plant and Cell Physiology **53**:1802–1814. DOI: https://doi.org/10.1093/pcp/pcs123

Lee J-Y, Wang X, Cui W, Sager R, Modla S, Czymmek K, Zybaliov B, van Wijk K, Zhang C, Lu H, Lakshmanan V. 2011. A plasmodesmata-localized protein mediates crosstalk between cell-to-cell communication and innate immunity in Arabidopsis. The Plant Cell **23**:3353–3373. DOI: https://doi.org/10.1105/tpc.111.087742, PMID: 21934146

Lee JY, Yoo BC, Lucas WJ. 2000. Parallels between nuclear-pore and plasmodesmal trafficking of information molecules. Planta **210**:177–187.

964 Lee J-Y, Yoo B-C, Rojas MR, Gomez-Ospina N, Staehelin LA, Lucas WJ. 2003. Selective trafficking of
965 non-cell-autonomous proteins mediated by NtNCAPP1. Science **299**:392–396. DOI:
966 https://doi.org/10.1126/science.1077813

967 Li C, Jensen VL, Park K, Kennedy J, Garcia-Gonzalo FR, Romani M, Mori RD, Bruel A-L, Gaillard D,
968 Doray B, Lopez E, Rivière J-B, Faivre L, Thauvin-Robinet C, Reiter JF, Blacque OE, Valente
969 EM, Leroux MR. 2016. MKS5 and CEP290 dependent assembly pathway of the ciliary transition
970 zone. PLOS Biology **14**:e1002416. DOI: https://doi.org/10.1371/journal.pbio.1002416

971 Li Z, Liu S-L, Montes-Serey C, Walley JW, Aung K. 2024. PLASMODESMATA-LOCATED PROTEIN
972 6 regulates plasmodesmal function in Arabidopsis vasculature. The Plant Cell **36**:3543–3561.
973 DOI: https://doi.org/10.1093/plcell/koae166

974 Lin DH, Hoelz A. 2019. The structure of the nuclear pore complex (an update). Annual review of
975 biochemistry **88**:725–783. DOI: https://doi.org/10.1146/annurev-biochem-062917-011901,
976 PMID: 30883195

977 Lu H, Ge P, Ma Y, Lin F, Jing D, Zhou T, Cui F. 2025. Loss-of-function of two PD-associated proteins
978 confers resistance to rice stripe virus. Molecular Plant Pathology **26**:e70121. DOI:
979 https://doi.org/10.1111/mpp.70121

980 Ma M, Li M, Zhou R, Yu J-B, Wu Y, Zhang X, Wang J, Zhou J-M, Liang X. 2023. CPR5 positively
981 regulates pattern-triggered immunity via a mediator protein. Journal of Integrative Plant Biology
982 **65**:1613–1619. DOI: https://doi.org/10.1111/jipb.13472

983 Makarov AA, Padilla-Mejia NE, Field MC. 2021. Evolution and diversification of the nuclear pore
984 complex. Biochemical Society Transactions **49**:1601–1619. DOI:
985 https://doi.org/10.1042/BST20200570, PMID: 34282823

986 Mansfeld J, Güttinger S, Hawryluk-Gara LA, Panté N, Mall M, Galy V, Haselmann U, Mühlhäusser P,
987 Wozniak RW, Mattaj IW, Kutay U, Antonin W. 2006. The conserved transmembrane nucleoporin
988 NDC1 is required for nuclear pore complex assembly in vertebrate cells. Molecular Cell **22**:93–
989 103. DOI: https://doi.org/10.1016/j.molcel.2006.02.015, PMID: 16600873

990 Miyashima S, Koi S, Hashimoto T, Nakajima K. 2011. Non-cell-autonomous microRNA165 acts in a
991 dose-dependent manner to regulate multiple differentiation status in the Arabidopsis root.
992 Development **138**:2303–2313. DOI: https://doi.org/10.1242/dev.060491, PMID: 21558378

993 Mosalaganti S, Obarska-Kosinska A, Siggel M, Taniguchi R, Turoňová B, Zimmerli CE, Buczak K,
994 Schmidt FH, Margiotta E, Mackmull M-T, Hagen WJH, Hummer G, Kosinski J, Beck M. 2022.
995 AI-based structure prediction empowers integrative structural analysis of human nuclear pores.
996 Science **376**:eabm9506. DOI: https://doi.org/10.1126/science.abm9506

997 Nakajima K, Sena G, Nawy T, Benfey PN. 2001. Intercellular movement of the putative transcription
998 factor SHR in root patterning. Nature **413**:307–311. DOI: https://doi.org/10.1038/35095061,
999 PMID: 11565032

1000 Narsai R, Law SR, Carrie C, Xu L, Whelan J. 2011. In-depth temporal transcriptome profiling reveals a
1001 crucial developmental switch with roles for RNA processing and organelle metabolism that are
1002 essential for germination in Arabidopsis. Plant Physiology **157**:1342–1362. DOI:
1003 https://doi.org/10.1104/pp.111.183129

1004 Ng SC, Biswas A, Huyton T, Schünemann J, Reber S, Görlich D. 2023. Barrier properties of NUP98 FG
1005 phases ruled by FG motif identity and inter-FG spacer length. Nature Communications **14**:747–
1006 747. DOI: https://doi.org/10.1038/s41467-023-36331-4

1007 Ng SC, Güttler T, Görlich D. 2021. Recapitulation of selective nuclear import and export with a perfectly
1008 repeated 12mer GLFG peptide. Nature Communications **12**:4047. DOI:
1009 https://doi.org/10.1038/s41467-021-24292-5

1010 Nicolas WJ, Grison MS, Trépout S, Gaston A, Fouché M, Cordelières FP, Oparka KJ, Tilsner J, Brocard
1011 L, Bayer EM. 2017. Architecture and permeability of post-cytokinesis plasmodesmata lacking

1012 cytoplasmic sleeves. Nature Plants **3**:17082. DOI: https://doi.org/10.1038/nplants.2017.82,
1013 PMID: 28604682

1014 Okuma E, Nozawa R, Murata Y, Miura K. 2014. Accumulation of endogenous salicylic acid confers
1015 drought tolerance to Arabidopsis. Plant Signaling & Behavior **9**:e28085. DOI:
1016 https://doi.org/10.4161/psb.28085, PMID: 24603484

1017 Otero S, Helariutta Y, Benitez-Alfonso Y. 2016. Symplastic communication in organ formation and tissue
1018 patterning. Current Opinion in Plant Biology **29**:21–28. DOI:
1019 https://doi.org/10.1016/j.pbi.2015.10.007

1020 Paultre DSG, Gustin M-P, Molnar A, Oparka KJ. 2016. Lost in transit: long-distance trafficking and
1021 phloem unloading of protein signals in Arabidopsis homografts. The Plant Cell **28**:2016–2025.
1022 DOI: https://doi.org/10.1105/tpc.16.00249

1023 Pendle A, Benitez-Alfonso Y. 2015. Immunofluorescence detection of callose deposition around
1024 plasmodesmata sites. Methods in Molecular Biology (Clifton, N.J.) **1217**:95–104. DOI:
1025 https://doi.org/10.1007/978-1-4939-1523-1_6, PMID: 25287198

1026 Peng S, Guo D, Guo Y, Zhao H, Mei J, Han Y, Guan R, Wang T, Song T, Sun K, Liu Y, Mao T, Chang
1027 H, Xue J, Cai Y, Chen D, Wang S. 2022. CONSTITUTIVE EXPRESSER of PATHOGENESIS-
1028 RELATED GENES 5 is an RNA-binding protein controlling plant immunity via an RNA
1029 processing complex. Plant Cell **34**:1724–1744. DOI: https://doi.org/10.1093/plcell/koac037

1030 Penzo A, Palancade B. 2023. Puzzling out nuclear pore complex assembly. FEBS Letters **597**:2705–2727.
1031 DOI: https://doi.org/10.1002/1873-3468.14713

1032 Pletan M, Wang E, Gohmann L, Tsai B. 2025. An ER-associated structure sequesters misassembled FG-
1033 rich nucleoporins to help maintain nuclear pore complex function. Journal of Cell Science
1034 **138**:jcs263659. DOI: https://doi.org/10.1242/jcs.263659

1035 Pöge M, Dickmanns M, Xu P, Li M, Schiøtz OH, Kaiser CO, Ma J, Bieber A, Capitanio C, Brenner J,
1036 Riggi M, Klumpe S, Miras M, Jasemi NSK, Schulze WX, Simon R, Frommer WB, Plitzko JM,
1037 Baumeister W. 2025. Making plant tissue accessible for cryo-electron tomography. eLife **14**.
1038 DOI: https://doi.org/10.7554/eLife.106455.1

1039 Qu F, Morris TJ. 2002. Efficient infection of *Nicotiana benthamiana* by tomato bushy stunt virus Is
1040 facilitated by the coat protein and maintained by p19 through suppression of gene silencing.
1041 Molecular Plant-Microbe Interactions® **15**:193–202. DOI:
1042 https://doi.org/10.1094/MPMI.2002.15.3.193

1043 Rappsilber J, Ishihama Y, Mann M. 2003. Stop and go extraction tips for matrix-assisted laser
1044 desorption/ionization, nanoelectrospray, and LC/MS sample pretreatment in proteomics.
1045 Analytical Chemistry **75**:663–670. DOI: https://doi.org/10.1021/ac026117i, PMID: 12585499

1046 Ross-Elliott TJ, Jensen KH, Haaning KS, Wager BM, Knoblauch J, Howell AH, Mullendore DL,
1047 Monteith AG, Paultre D, Yan D, Otero S, Bourdon M, Sager R, Lee J-Y, Helariutta Y, Knoblauch
1048 M, Oparka KJ. 2017. Phloem unloading in Arabidopsis roots is convective and regulated by the
1049 phloem-pole pericycle. eLife **6**:e24125. DOI: https://doi.org/10.7554/eLife.24125, PMID:
1050 28230527

1051 Sakulkoo W, Osés-Ruiz M, Oliveira Garcia E, Soanes DM, Littlejohn GR, Hacker C, Correia A, Valent
1052 B, Talbot NJ. 2018. A single fungal MAP kinase controls plant cell-to-cell invasion by the rice
1053 blast fungus. Science **359**:1399–1403. DOI: https://doi.org/10.1126/science.aaq0892

1054 Scheer U, Franke WW. 1972. Annulate lamellae in plant cells: Formation during microsporogenesis and
1055 pollen development in Canna generalis Bailey. Planta **107**:145–159. DOI:
1056 https://doi.org/10.1007/BF00387720

1057 Schindelin J, Arganda-Carreras I, Frise E, Kaynig V, Longair M, Pietzsch T, Preibisch S, Rueden C,
1058 Saalfeld S, Schmid B, Tinevez JY, White DJ, Hartenstein V, Eliceiri K, Tomancak P, Cardona

1059 A. 2012. Fiji: an open-source platform for biological-image analysis. Nature Methods **9**:676–82.
1060 DOI: https://doi.org/10.1038/nmeth.2019

1061 Shimada TL, Shimada T, Hara-Nishimura I. 2010. A rapid and non-destructive screenable marker, FAST,
1062 for identifying transformed seeds of *Arabidopsis thaliana*. The Plant Journal **61**:519–528. DOI:
1063 https://doi.org/10.1111/j.1365-313X.2009.04060.x

1064 Shimozono S, Miyawaki A. 2008. Engineering FRET constructs using CFP and YFP. *Methods in Cell*
1065 *Biology*, Fluorescent Proteins. Academic Press. p. 381–393. DOI: https://doi.org/10.1016/S0091-
1066 679X(08)85016-9

1067 Song L i, Zhou X-Y, Li L i, Xue L-J, Yang X i, Xue H-W. 2009. Genome-wide analysis revealed the
1068 complex regulatory network of brassinosteroid effects in photomorphogenesis. Molecular Plant
1069 **2**:755–772. DOI: https://doi.org/10.1093/mp/ssp039, PMID: 19825654

1070 Takao D, Wang L, Boss A, Verhey KJ. 2017. Protein interaction analysis provides a map of the spatial
1071 and temporal organization of the ciliary gating zone. Current Biology **27**:2296-2306.e3. DOI:
1072 https://doi.org/10.1016/j.cub.2017.06.044

1073 Tamura K, Fukao Y, Iwamoto M, Haraguchi T, Hara-Nishimura I. 2010. Identification and
1074 characterization of nuclear pore complex components in *Arabidopsis thaliana*. The Plant Cell
1075 **22**:4084–4097. DOI: https://doi.org/10.1105/tpc.110.079947

1076 Tamura K, Stecher G, Kumar S. 2021. MEGA11: Molecular Evolutionary Genetics Analysis Version 11.
1077 Molecular Biology and Evolution **38**:3022–3027. DOI: https://doi.org/10.1093/molbev/msab120

1078 Tang Y, Huang A, Gu Y. 2020. Global profiling of plant nuclear membrane proteome in Arabidopsis.
1079 Nature Plants **6**:838–847. DOI: https://doi.org/10.1038/s41477-020-0700-9, PMID: 32601417

1080 Tee EE, Faulkner C. 2024. Plasmodesmata and intercellular molecular traffic control. New Phytologist
1081 **243**:32–47. DOI: https://doi.org/10.1111/nph.19666

1082 Tee EE, Samwald S, Faulkner C. 2022. Quantification of cell-to-cell connectivity using particle
1083 bombardment. Methods in Molecular Biology (Clifton, N.J.) **2457**:263–272. DOI:
1084 https://doi.org/10.1007/978-1-0716-2132-5_17, PMID: 35349146

1085 Terry LJ, Wente SR. 2009. Flexible gates: dynamic topologies and functions for FG nucleoporins in
1086 nucleocytoplasmic transport. Eukaryotic Cell **8**:1814–1827. DOI:
1087 https://doi.org/10.1128/EC.00225-09, PMID: 19801417

1088 Thomas CL, Bayer EM, Ritzenthaler C, Fernandez-Calvino L, Maule AJ. 2008. Specific targeting of a
1089 plasmodesmal protein affecting cell-to-cell communication. PLoS Biology **6**:e7. DOI:
1090 https://doi.org/10.1371/journal.pbio.0060007

1091 Usadel B, Nagel A, Thimm O, Redestig H, Blaesing OE, Palacios-Rojas N, Selbig J, Hannemann J, Piques
1092 MC, Steinhauser D, Scheible W-R, Gibon Y, Morcuende R, Weicht D, Meyer S, Stitt M. 2005.
1093 Extension of the visualization tool MapMan to allow statistical analysis of arrays, display of
1094 corresponding genes, and comparison with known responses. Plant Physiology **138**:1195–1204.
1095 DOI: https://doi.org/10.1104/pp.105.060459, PMID: 16009995

1096 Wang F, Wang L, Qiao L, Chen J, Pappa MB, Pei H, Zhang T, Chang C, Dong C-H. 2017. Arabidopsis
1097 CPR5 regulates ethylene signaling via molecular association with the ETR1 receptor. Journal of
1098 Integrative Plant Biology **59**:810–824. DOI: https://doi.org/10.1111/jipb.12570

1099 Wang S, Gu Y, Zebell SG, Anderson LK, Wang W, Mohan R, Dong X. 2014. A noncanonical role for
1100 the CKI-RB-E2F cell-cycle signaling pathway in plant effector-triggered immunity. Cell Host &
1101 Microbe **16**:787–794. DOI: https://doi.org/10.1016/j.chom.2014.10.005, PMID: 25455564

1102 Winter CM, Szekely P, Popov V, Belcher H, Carter R, Jones M, Fraser SE, Truong TV, Benfey PN. 2024.
1103 SHR and SCR coordinate root patterning and growth early in the cell cycle. Nature 1–6. DOI:
1104 https://doi.org/10.1038/s41586-023-06971-z

Xiao L, Jiang S, Huang P, Chen F, Wang X, Cheng Z, Miao Y, Liu L, Searle I, Liu C, Wu X-X, Fu Y-F, Chen Q, Zhang X-M. 2020. Two *Nucleoporin98* homologous genes jointly participate in the regulation of starch degradation to repress senescence in Arabidopsis. BMC Plant Biology **20**:292. DOI: https://doi.org/10.1186/s12870-020-02494-1

Xie W, Nielsen ME, Pedersen C, Thordal-Christensen H. 2017. A split-GFP gateway cloning system for topology analyses of membrane proteins in plants. PLOS ONE **12**:e0170118. DOI: https://doi.org/10.1371/journal.pone.0170118

Yu M, Heidari M, Mikhaleva S, Tan PS, Mingu S, Ruan H, Reinkemeier CD, Obarska-Kosinska A, Siggel M, Beck M, Hummer G, Lemke EA. 2023. Visualizing the disordered nuclear transport machinery *in situ*. Nature **617**:162–169. DOI: https://doi.org/10.1038/s41586-023-05990-0

Zavaliev R, Epel BL. 2015. Imaging callose at plasmodesmata using aniline blue: quantitative confocal microscopy. Methods in Molecular Biology (Clifton, N.J.) **1217**:105–119. DOI: https://doi.org/10.1007/978-1-4939-1523-1_7, PMID: 25287199

Zhang C, An N, Jia P, Zhang W, Liang J, Zhang X, Zhou H, Ma W, Han M, Xing L, Ren X. 2020. Genomic identification and expression analysis of nuclear pore proteins in *Malus domestica*. Scientific Reports **10**:17426. DOI: https://doi.org/10.1038/s41598-020-74171-0

Zimmerli CE, Allegretti M, Rantos V, Goetz SK, Obarska-Kosinska A, Zagoriy I, Halavatyi A, Hummer G, Mahamid J, Kosinski J, Beck M. 2021. Nuclear pores dilate and constrict *in cellulo*. Science **374**:eabd9776. DOI: https://doi.org/10.1126/science.abd9776

Acknowledgments

We would like to dedicate this manuscript to the 'champion of plasmodesmata', William J. (Bill) Lucas (UC Davis). We thank Madlen Somsich (HHU) for project coordination and management. This work has received funding from the European Research Council (ERC) and the Marie Skłodowska-Curie Actions under the European Union's Horizon 2020 research and innovation program (Grant agreements 'SymPore' No. 951292 to WBF and "PDgate" No. 101023981 to MM, respectively). ARE was supported in part by funds from the Interdisciplinary Graduate and Research Academy (iGRAD) Düsseldorf (Deutsche Forschungsgemeinschaft (DFG, German Research Foundation), DFG, project ID 391465903/GRK 2466). Research was also supported by the Deutsche Forschungsgemeinschaft (DFG, German Research Foundation) under Germany´s Excellence Strategy – EXC-2048/1 – project ID 390686111, and the Alexander von Humboldt Professorship, to WBF.

Data availability

Source data have been assigned a DOI (http://doi.org/10.60534/46qra-6bw98) and are accessible via https://git.nfdi4plants.org/projects/2188. Materials will be made available under MTA; some materials were obtained from others as marked and require permission from the respective authors.

Contributions

WBF conceived of the study. J.E. performed the bioinformatic analyses; L.X., S.G. and W.S. performed proteomics and data analysis; M.D. analyzed the structure and generated Figure 2-figure supplement 1; S.H. helped to establish and advised on SIM. T.M.S, M.P., M.M., J.O.E., N.P., M.N., G.V.D, C.G. and A.D. performed imaging and/or transport studies; R.S. advised on imaging and data analyses; M.M. and A.R-E. performed split GFP studies, T.M.S, M.M., M.P., J.O.E., B.S., and W.B.F. analyzed the data; T.M.S., M.M., M.P., J.O.E., G.V.D, R.S. and W.B.F. wrote the manuscript.

Competing interests

We declare no competing interests.

Supplementary Materials

- 8 Supplementary Tables
- 9 Supplementary Figures
- 3 Supplementary files
- 2 Supplemental scripts

Figures with supplements and legends

Figure 1 with 1 supplement

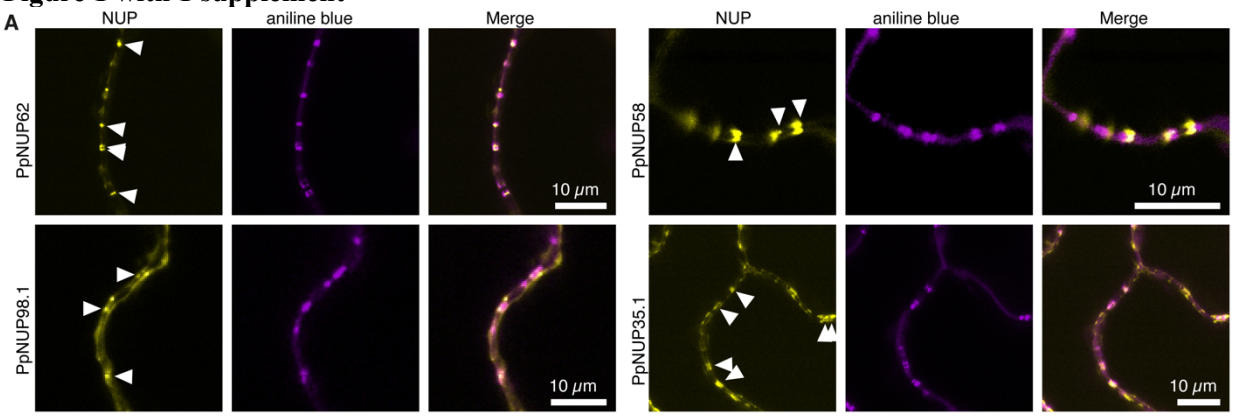

Figure 1. Identification of NUPs at PD. (A) Localization of NUPs from *Physcomitrium patens* at PD transiently expressed in *N. benthamiana* epidermal cells visualized by a single confocal optical section.

1161

1162

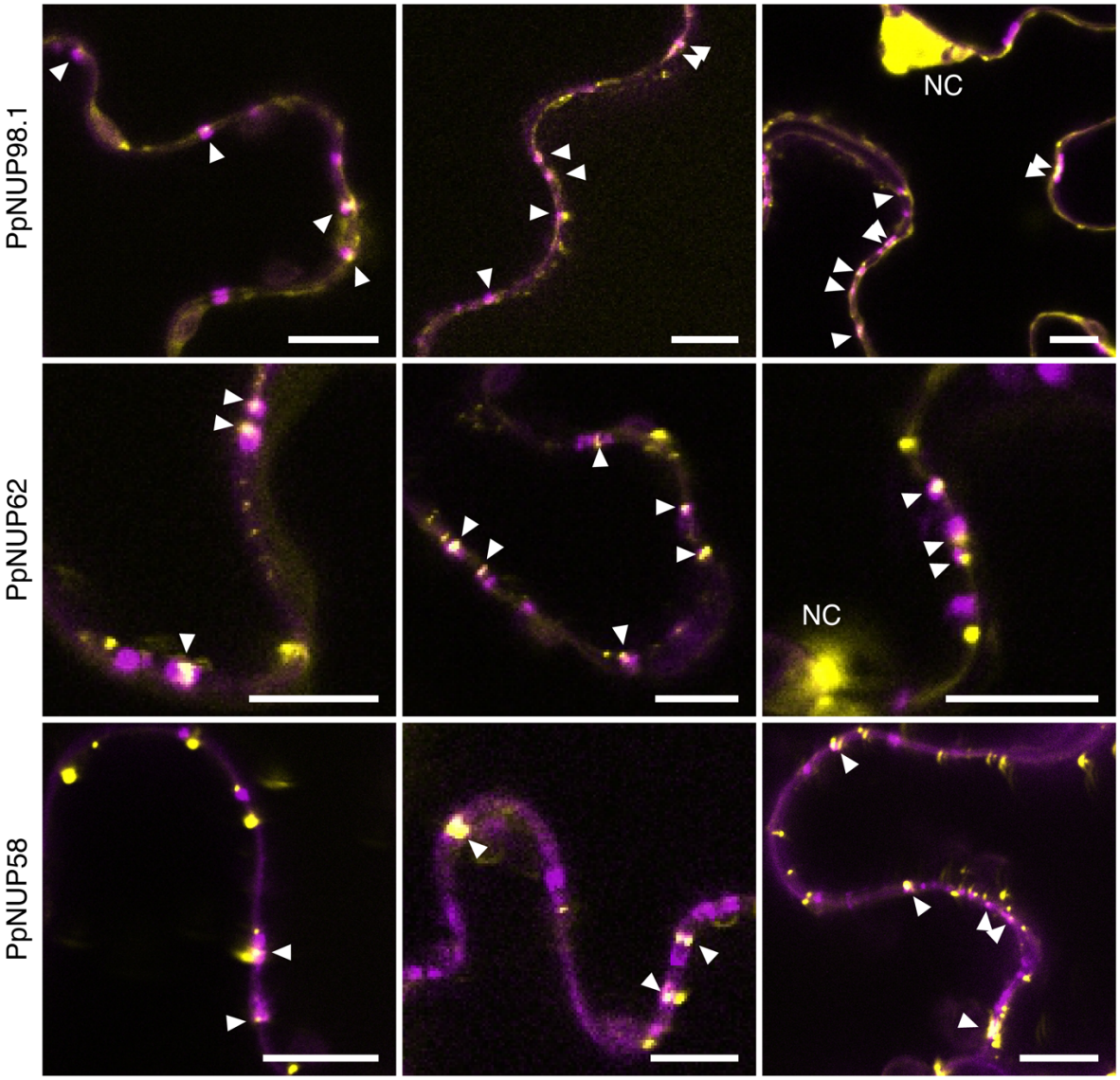

1163

1164

1165 **Figure 1-figure supplement 1. Overlay of *Physcomitrium patens* FG-NUPs with the PD marker**
1166 **aniline blue.** Localization of FG-NUPs from *P. patens* transiently expressed in *N. benthamiana* epidermal
1167 cells visualized by a single confocal optical section. FG-NUPs were fused at their C-terminus to mVenus
1168 (yellow) and expressed transiently under the control of the inducible XVE promotor. Aniline blue (purple)
1169 was infiltrated to stain callose, which accumulates in pit fields. Arrowheads indicate overlay between
1170 NUPs and aniline blue. For each NUP, a similar localization pattern appeared in at least three independent
1171 experiments. NC = nucleus. Scale bar: 10 µm.

1172

Figure 2 with 2 supplement

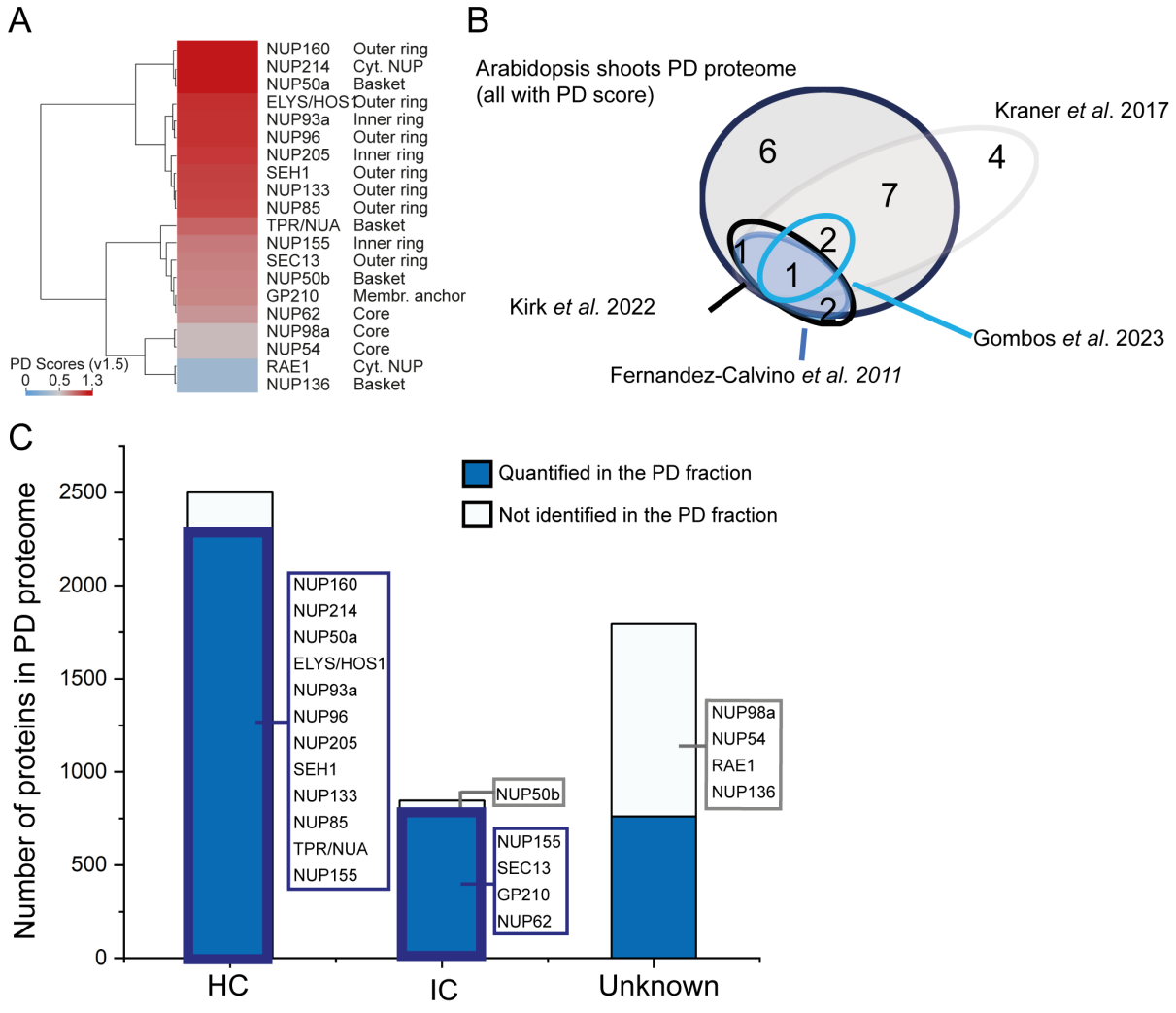

Figure 2. NUPs are found in Arabidopsis shoot proteome and other PD proteomes. (A), Hierarchical clustering of PD scores of Arabidopsis NPC components found in PD proteome preparations from 5-week-old Arabidopsis shoot tissues. Clustering based on Euclidean distance of PD scores (v1.5), which were averages of at least three replicate scores from separate tissue preparations. Color scale represents PD score values. PD scores above the high-confidence threshold of 0.5 are indicated in shades of red. (**B**), Comparison of NUPs in Arabidopsis shoot PD proteomes with published PD proteomes. Among the NUPs identified in the Arabidopsis shoot PD proteome, 73.3% (11 out of 15) were also detected in previously published PD proteomes. (**C**), Overview of identified proteins in the PD proteome. High confidence (HC) (PD score > 0.83), intermediate confidence (IC) (0.83 > PD score > 0.63), and Unknown (PD score < 0.63). Purple-edged boxes in HC and MC mark proteins that meet Arabidopsis shoot PD proteome criteria (PD score > 0.63, quantifiable in PD fraction). Blue-edged boxes denote 16 NUPs within the Arabidopsis shoot PD proteome; Gray-edged boxes represent NUPs found also in other proteomes.

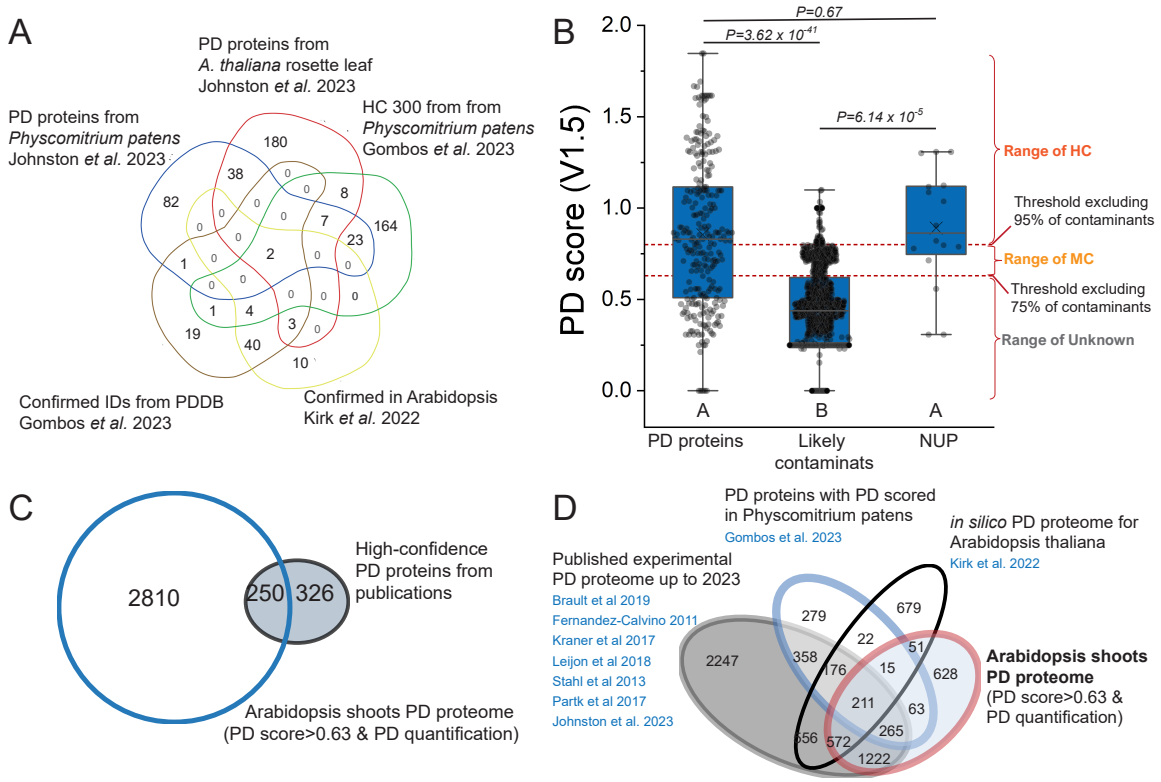

Figure 2-figure supplement 1. Arabidopsis shoot proteome and the comparison to other PD proteomes. (**A**), Venn diagram defining high-confidence PD proteins from previous publications, e.g., confirmed Arabidopsis PD proteins, and high confidence PD proteins identified in *Physcomitrium*, and in both *Physcomitrium* and Arabidopsis leaves (Gombos et al., 2023; Johnston et al., 2023; Kirk et al., 2022). These proteins were then used as high-confidence data set to establish the PD probability threshold and were labelled as 'PD proteins' in file S3. 43% of these proteins were quantified in our Arabidopsis shoot PD proteome. (**B**), PD Scores of nuclear pore components. PD Scores (v 1.5) are shown as box plots for high-confidence PD proteins (PD proteins), typical co-purifying proteins from plastid and mitochondria identified in Arabidopsis PD preparations (likely contaminants) and proteins of the nuclear pore complex (NUP). Dotted lines indicate two thresholds based on the frequency distribution for contaminant proteins and PD proteins. The median is shown as a gray line, the mean value is denoted by a + symbol, and the whiskers cover the 95thpercentile. PD Scores above 0.83 (the upper dotted line) indicate high-confidence (HC) PD proteins; scores between 0.63 and 0.83 (between the two dotted lines) signify medium-confidence (MC) PD proteins; and scores below 0.63 are considered low confidence (LC) as their PD Scores overlapped with 75% of the contaminants. These confidence clusters were annotated in file S3. The final Arabidopsis shoot PD proteome consists of proteins with PD scores above 0.63, which are also quantifiable in the PD fraction. Capital letters represent group statistical comparisons determined by one-way ANOVA. The p-values of pairwise comparison using Student's t-test, are indicated on the top of the boxes. (**C**), Overlap between the Arabidopsis shoot PD proteome and other PD proteomes. Proteins with a PD score >0.63 and quantifiable in PD fraction (Arabidopsis shoot PD proteome) were compared with nine representative PD proteome studies. In the current Arabidopsis shoot PD proteome, 80% of the proteins were previously identified in published PD proteomes. Combining PD enrichment and data analysis thresholding allowed us to determine the confidence levels of PD proteins and obtain a "cleaner" PD proteome. In total, we identified 5145 proteins from PD, CW, and TC fractions, with 3347 proteins having a PD score >0.63. Among them, 3062 proteins are quantifiable in the PD fraction, constituting our Arabidopsis shoot PD proteome. Among these, 2268 proteins are categorized as high-confidence PD proteins, while 792 proteins fall into the medium-confidence category (file S3). Additionally, we discovered 20 nuclear pore proteins (NUPs), with 15 of them surpassing the threshold and being included in the final PD proteome. Among these, 11 are classified as high-confidence PD proteins, while 4 are medium-confidence PD proteins (file S3, Figure 1-figure supplement 2B). (**D**)

1221 Comparison of Arabidopsis shoot PD proteomes with various published PD proteomes. 80% of the
1222 proteins had been identified in previous studies.
1223
1224
1225
1226

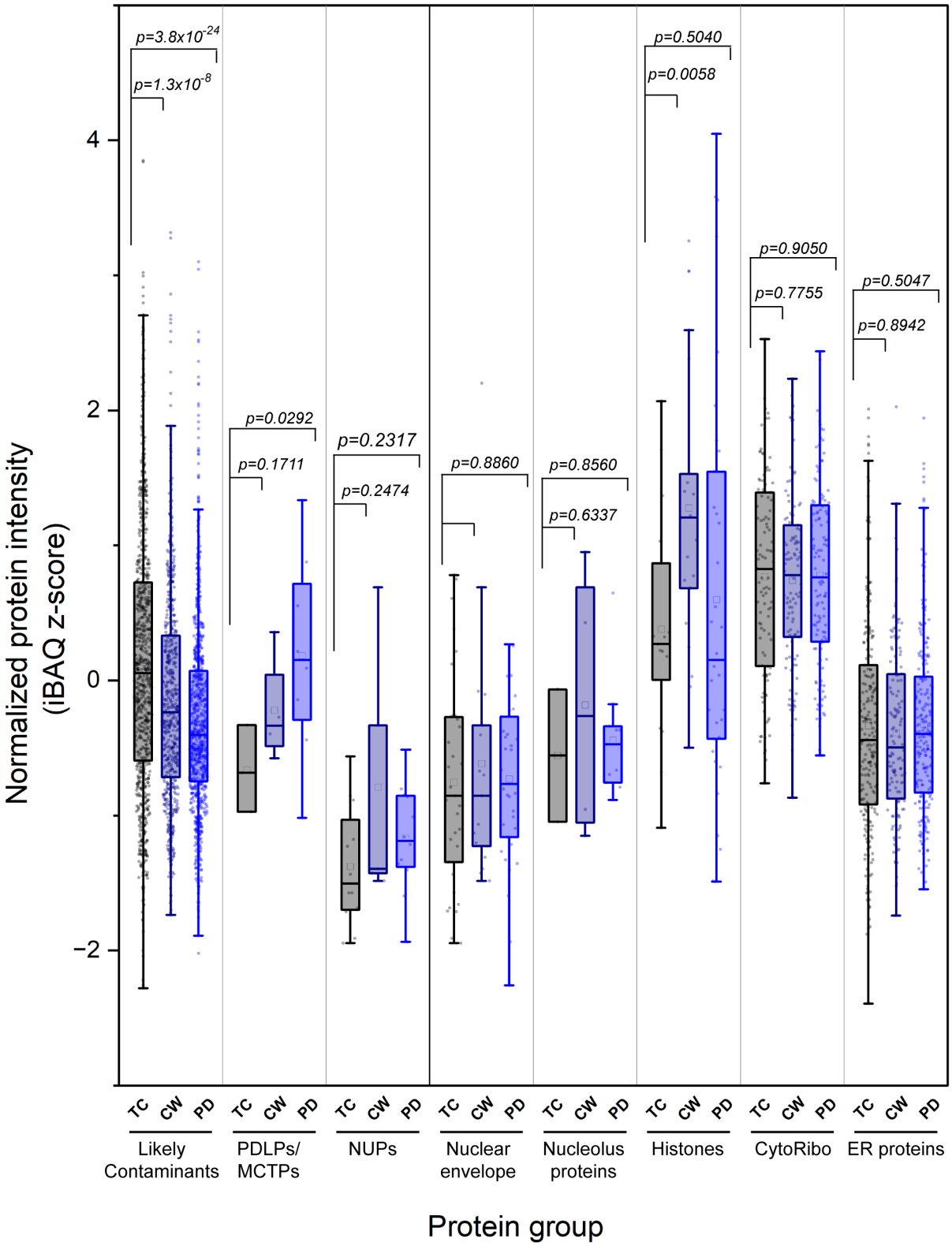

Figure 2-figure supplement 2. Normalized protein intensities of different protein groups in total extract (TC), cell wall fraction (CW) and PD enrichment (PD). The group of likely contaminants contains plastidic and mitochondrial proteins. *Bona fide* PD proteins are PDLPs and MCTPs. Protein categorization was based on Mapman (Usadel et al., 2005). A Student's t-test was used for statistical analysis.

1234 **Figure 3 with 1 supplement**

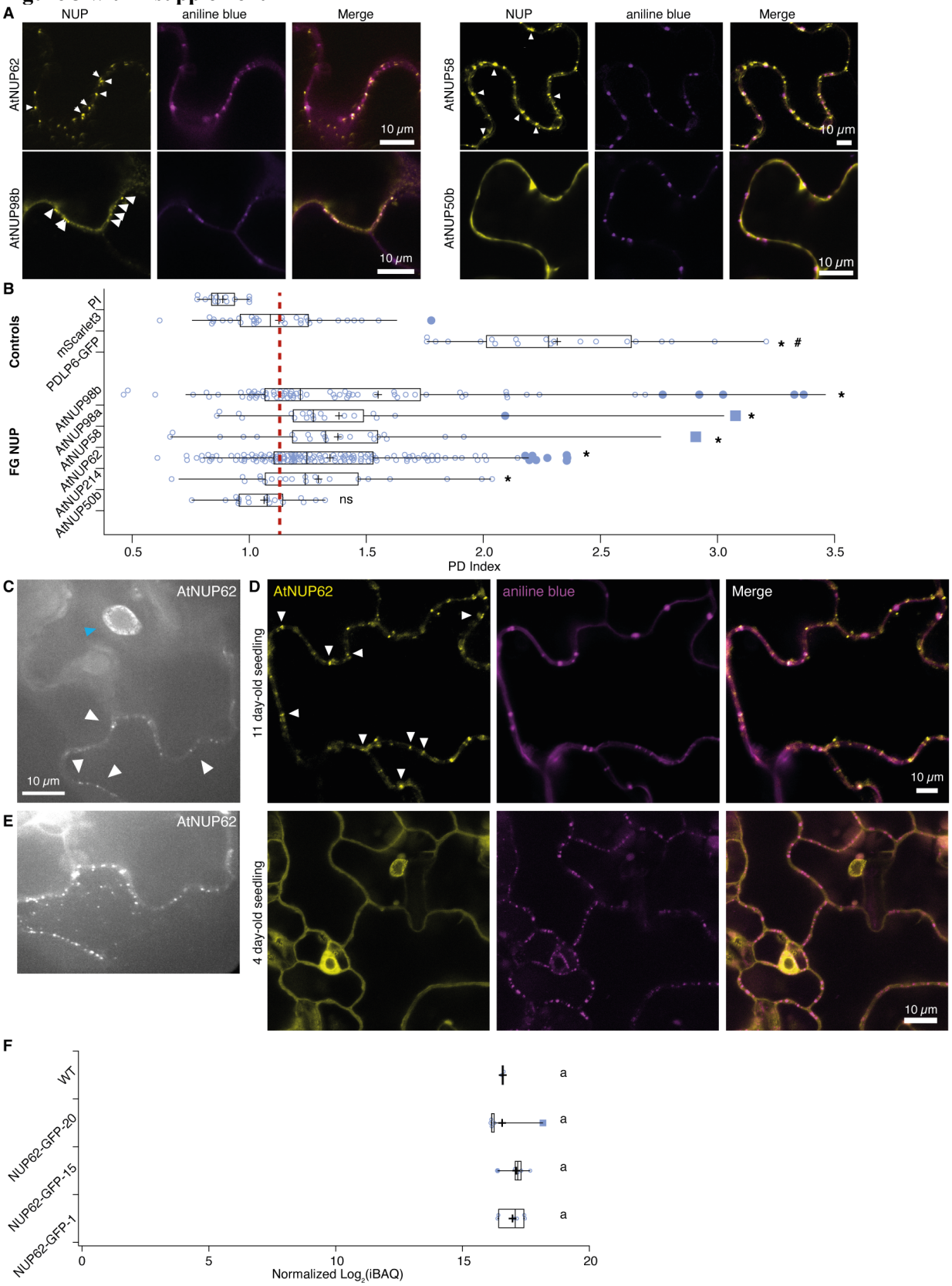

1235

1236 **Figure 3. Dual localization of Arabidopsis FG NUPs. (A)** Localization of selected Arabidopsis FG-
1237 NUPs after transient expression under the control of the β-estradiol-inducible XVE promotor in *N.*
1238 *benthamiana* epidermal cells visualized by a single confocal optical section. mVenus was fused to the C-
1239 terminus of different NUPs, except for NUP98a for which GFP was fused both N- and C-terminally (GFP-

1240 NUP98a-GFP). Aniline blue was infiltrated to detect callose in pit fields as a PD marker. Localization
1241 was repeated in three independent experiments with similar results. (**B**) Quantification of the PD
1242 localization by PD index. Red dashed line indicates the mean PD index of mScarlet3 (cytoplasmic
1243 control). PI, propidium iodide ('membrane impermeant dye'). Significantly ($p < 0.05$) increased PD
1244 indices compared to the cell wall or cytoplasmic controls are indicated by * and #, respectively. Kruskal-
1245 Wallis Test $p < 0.001$, p-values of Bonferroni-corrected Dunn´s test for pairwise comparison are
1246 summarized in table S2. Median is represented by vertical line inside the box, mean is represented by the
1247 bold +. Values between quartiles 1 and 3 are represented by box ranges, and 5th and 95th percentile are
1248 represented by error bars. At least 15 images from 3 biological replicates were analyzed for each NUP.
1249 Independent localization data are shown in Figure 1-figure supplement 3. (**C-E**) Arabidopsis NUP62-GFP
1250 plants expressing NUP62 fused to GFP under its own promoter. (**C**) The localization of NUP62-GFP in
1251 11-day-old cotyledon epidermal cells was visualized by a single confocal optical section (CSU10; 100x
1252 oil-immersion objective). Arrowhead: blue nucleus, white peripheral NUP62-GFP. **(D)** Localization of
1253 NUP62-GFP in cotyledonar epidermal cells of stably transformed 11-day-old (*top*) and 4-day-old
1254 (*bottom*) Arabidopsis lines. Cotyledons were immersed in aniline blue to detect callose in pit fields as PD
1255 markers. White arrowheads in D indicate overlay of NUPs and aniline blue. Scale bar: 10 µm. **(E)**
1256 Maximum intensity projection of 20 optical cross-sections taken at 1µm intervals of epidermal cotyledon
1257 cells expressing NUP62 fused to GFP under its own promoter (11-day-old seedling). Punctate localization
1258 of NUP62-GFP can also be found at the epidermis cell surface on the adaxial side of the cell. **(F)**
1259 Quantification of NUP62 protein abundance by MS analysis in cotyledons of 14-day old Arabidopsis
1260 seedlings. Normalized iBAQ values were used to compare transgenic lines with wild-type (Col-0), n=2-
1261 6 technical repeats based on 2-3 independent biological sample preparations. Statistical significance was
1262 determined by one-way ANOVA: $p = 0.5$. Different letters indicate statistically significant differences at
1263 $p < 0.05$. Mean normalized $\log_2$ (iBAC) ± SEM: *WT*: 16.58 ± 0.04; *NUP62-GFP-1*: 16.97 ± 0.2; *NUP62-*
1264 *GFP-15*: 17.12 ± 0.2; *NUP62-GFP*-20: 16.56 ± 0.4.

1265

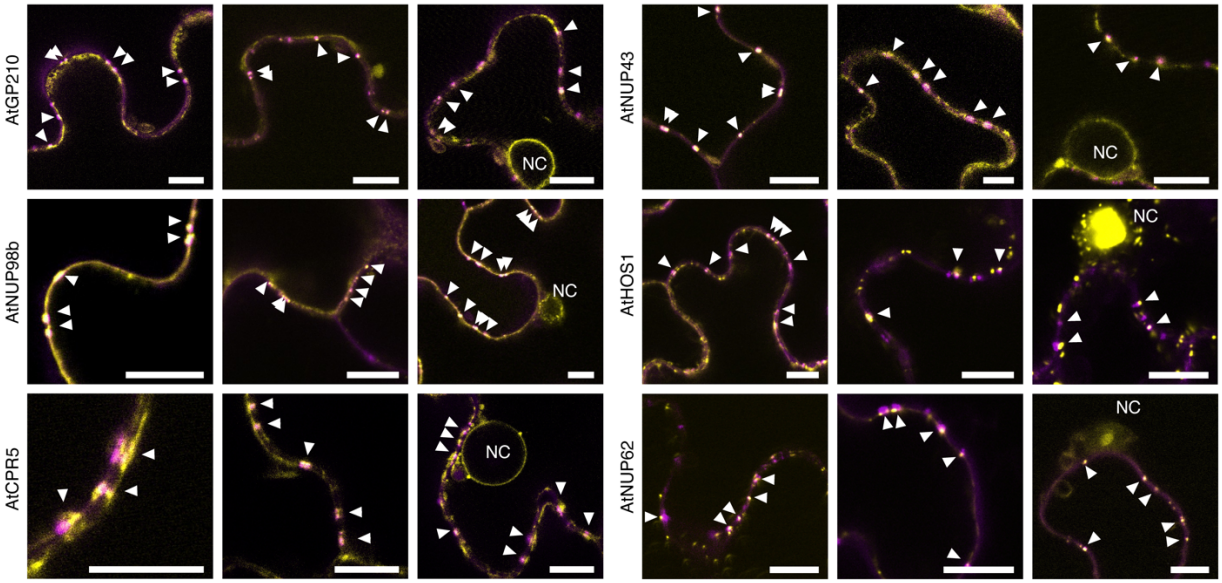

Figure 3-figure supplement 1. Arabidopsis NUP-FP localization overlays with a PD marker. Localization of Arabidopsis NUPs transiently expressed in *N. benthamiana* epidermal cells visualized by a single confocal optical section. NUPs were fused at their C-terminus to mVenus or mCitrine (yellow) and expressed transiently under the control of the inducible XVE promotor. Aniline blue (purple) was infiltrated to stain callose that accumulates in pit fields. Arrowheads indicate overlay between NUPs and aniline blue. NUPs shown here were found to have a significant increased PD index values compared to negative controls in Figure 2. For each NUP, the localization pattern was reproducible in at least in three independent experiments. NC, nuclei. Note that for comparison, we here show the same images for NUP98B and NUP62 from Figure 2A again. Scale bar: 10 µm.

Figure 4

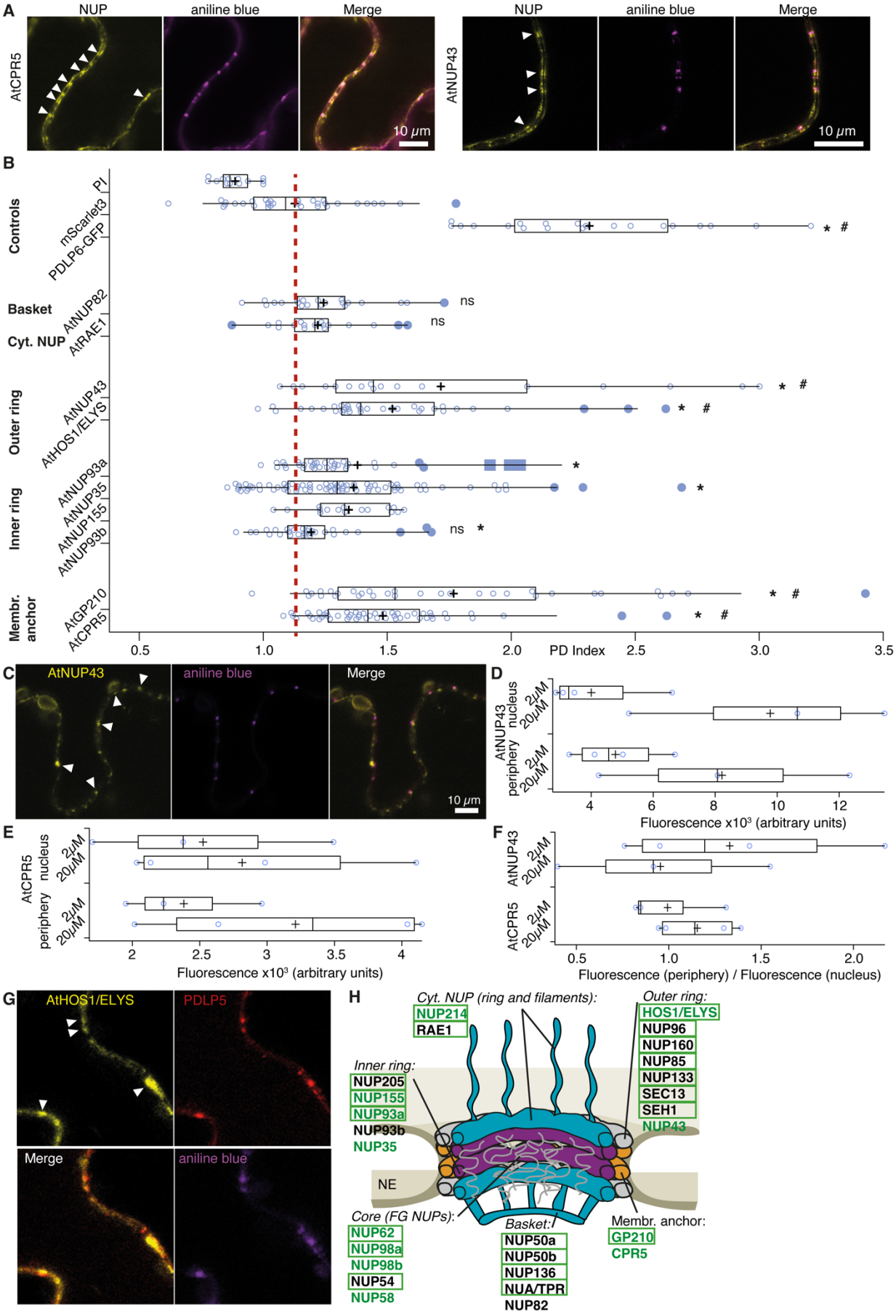
A
NUP
aniline blue
Merge
AtCPR5
AtNUP43
10 µm
B
Controls
PI
mScarlet3
PDLP6-GFP
Basket
AtNUP82
Cyt. NUP
AtRAE1
Outer ring
AtNUP43
AtHOS1/ELYS
Inner ring
AtNUP93a
AtNUP35
AtNUP155
AtNUP93b
Membr. anchor
AtGP210
AtCPR5
ns
*
#
0.5
1.0
1.5
2.0
PD Index
2.5
3.0
3.5
C
AtNUP43
aniline blue
Merge
10 µm
D
AtNUP43
nucleus
periphery
2µM
20µM
4
6
8
10
12
Fluorescence x10³ (arbitrary units)
E
AtCPR5
nucleus
periphery
2µM
20µM
2
2.5
3
3.5
4
Fluorescence x10³ (arbitrary units)
F
AtNUP43
AtCPR5
2µM
20µM
0.5
1.0
1.5
2.0
Fluorescence (periphery) / Fluorescence (nucleus)
G
AtHOS1/ELYS
PDLP5
Merge
aniline blue
H
Cyt. NUP (ring and filaments):
NUP214
RAE1
Outer ring:
HOS1/ELYS
NUP96
NUP160
NUP85
NUP133
SEC13
SEH1
NUP43
Inner ring:
NUP205
NUP155
NUP93a
NUP93b
NUP35
NE
Core (FG NUPs):
NUP62
NUP98a
NUP98b
NUP54
NUP58
Basket:
NUP50a
NUP50b
NUP136
NUA/TPR
NUP82
Membr. anchor:
GP210
CPR5

1280 **Figure 4. Dual localization of Arabidopsis scaffold and transmembrane NUPs. (A)** Localization of
1281 Arabidopsis transmembrane (CPR5) and scaffold (NUP43) NUPs after transient expression under the
1282 control of the β-estradiol-inducible XVE promotor in *N. benthamiana* epidermal cells. mVenus was fused
1283 to the C-terminus of different NUPs. Aniline blue was infiltrated to detect callose in pit fields as PD
1284 marker. White arrowheads indicate overlay with aniline blue. Localization was repeated in three
1285 independent experiments with similar results. (**B**) Quantification of the Arabidopsis NUPs PD localization
1286 by PD index. Red dashed line indicates the mean PD index of mScarlet3 (cytoplasmic control). PI,
1287 propidium iodide ('membrane impermeant dye'). Significantly ($p < 0.05$) increased PD indices compared
1288 to cell wall or cytoplasmic controls indicated by * and #, respectively. Kruskal-Wallis Test $p < 0.001$, *p*-
1289 values of Bonferroni-corrected Dunn´s test for pairwise comparison are summarized in table S2. Median:
1290 vertical line inside box, mean: +. Values between quartiles 1 and 3: box ranges, and 5th and 95th percentile
1291 are represented by error bars. At least 15 images from 3 biological replicates were analyzed for each NUP.
1292 Independent data in Figure 1-figure supplement 3. Control identical to Figure 2B. (**C**) NUP43-mCitrine
1293 localization at PD transiently expressed in *N. benthamiana* epidermal cells at 1/10 β-estradiol
1294 concentration and shortened induction time (not exceeding 10h), visualized by a single confocal optical
1295 section. White arrowheads: overlay with aniline blue. **(D and E)** Quantification of the fluorescence
1296 intensity of NUP43-mCitrine (D) and CPR5-FP fusions (mVenus and mCitrine) (E) in the periphery and
1297 the nucleus after induction by 20µM or 2µM β-estradiol. **(F)** Periphery/nucleus fluorescence ratios in *N.*
1298 *benthamiana* epidermal cells transiently expressing NUP43-mCitrine or CPR5-FP fusions after
1299 expression is induced by 2 or 20µM β-estradiol. Box plots in (D-F) are based on a smaller subset of
1300 confocal images that show nucleus and peripheral fluorescence in one image; for individual conditions: n
1301 ≥ 3 images from at least 2 independent repeats. Student´s t-test in (F) 2µM vs. 20µM estradiol: for NUP43,
1302 p = 0.26 and for CPR5, p = 0.45. (**G**) Localization of HOS1/ELYS-mCitrine and PDLP5-mScarlet3 co-
1303 expressed transiently under the control of the inducible XVE promoter in *N. benthamiana* epidermal cells.
1304 Aniline blue was infiltrated to stain callose that accumulates in pit fields. White arrowheads: overlay of
1305 HOS1/ELYS-mCitrine and PDLP5-mScarlet3 channels. Localization repeated in three independent
1306 experiments with comparable results. All confocal images in Figure3 are single confocal optical sections.
1307 **(H)** Scheme of an NPC embedded in the nuclear envelope with all NUPs studied in this work. NUPs listed
1308 in B are green boxed. Green letters: NUPs significantly enriched at PD in transient localization assays
1309 (Figure 2B, 3B). Green boxed black letters: NUP was identified in the proteome, but was not enriched at
1310 PD in transient localization assays. Corresponding AGI locus identifiers in table S2. Cytoplasmic NUP is
1311 abbreviated as Cyt. NUP, and membrane anchor as Membr. anchor.

1312

1313

1314 **Figure 5 with 1 supplement**

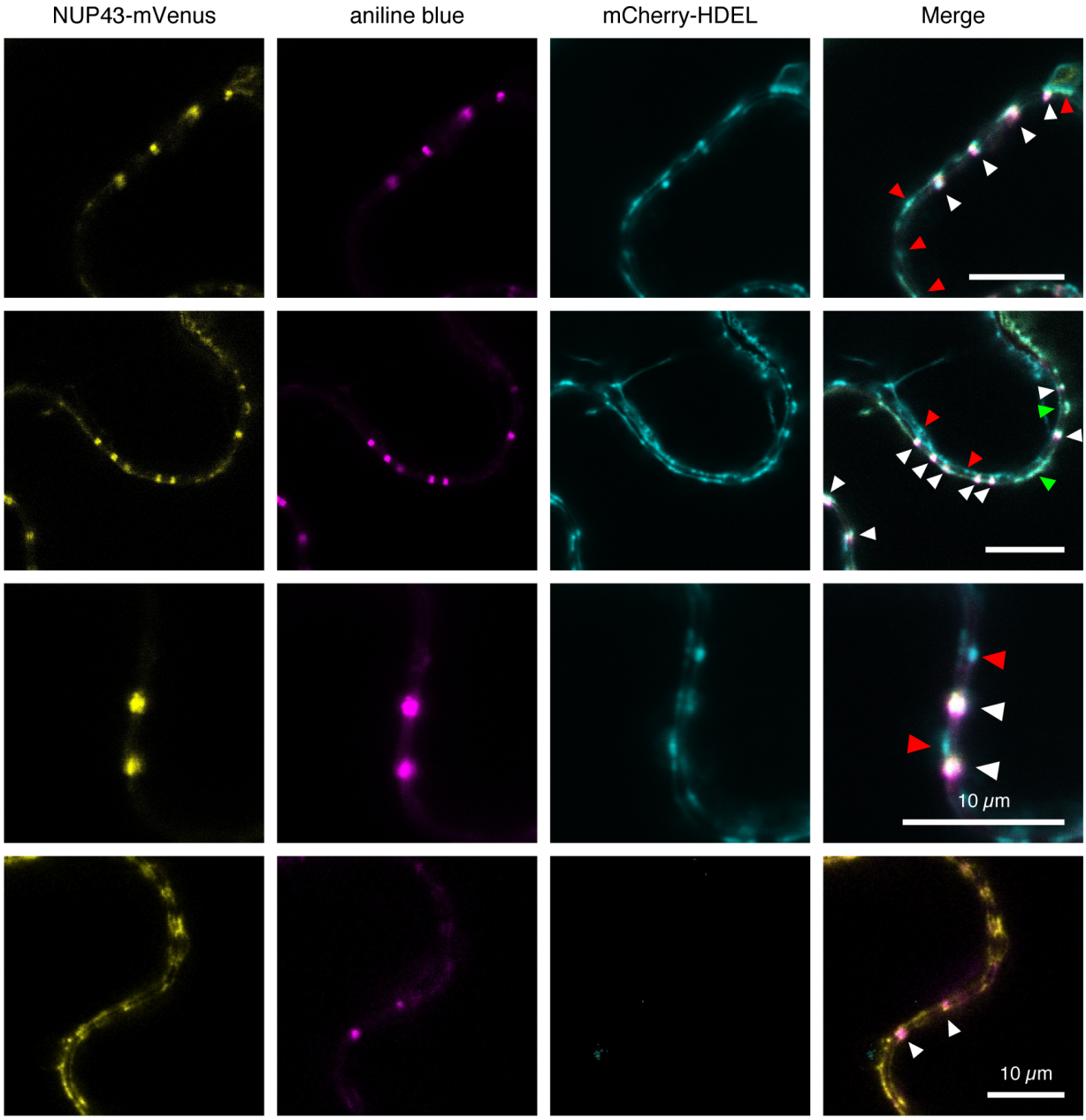

1315

1316 **Figure 5. Distinct localization patterns of Arabidopsis NUP43-mVenus and luminal ER marker.**
1317 Transient co-expression of NUP43-mVenus and mCherry-HDEL in *N. benthamiana* leaf epidermal cells,
1318 visualized by a single confocal optical section. Aniline blue was infiltrated to detect callose in pit fields
1319 as PD marker. *Bottom,* transient co-expression of NUP43-mVenus without mCherry-HDEL to test for
1320 crosstalk. White arrowheads indicate overlay of NUP43-mVenus, mCherry-HDEL. And aniline blue. Red
1321 arrows indicate mCherry-HDEL specific localization., without overly with other markers. White arrows
1322 (*middle right* panel) indicate overlay of NUP43-mVenus and mCherry-HDEL but absent aniline blue
1323 staining. Scale bar indicates 10 µm.

1324

1325

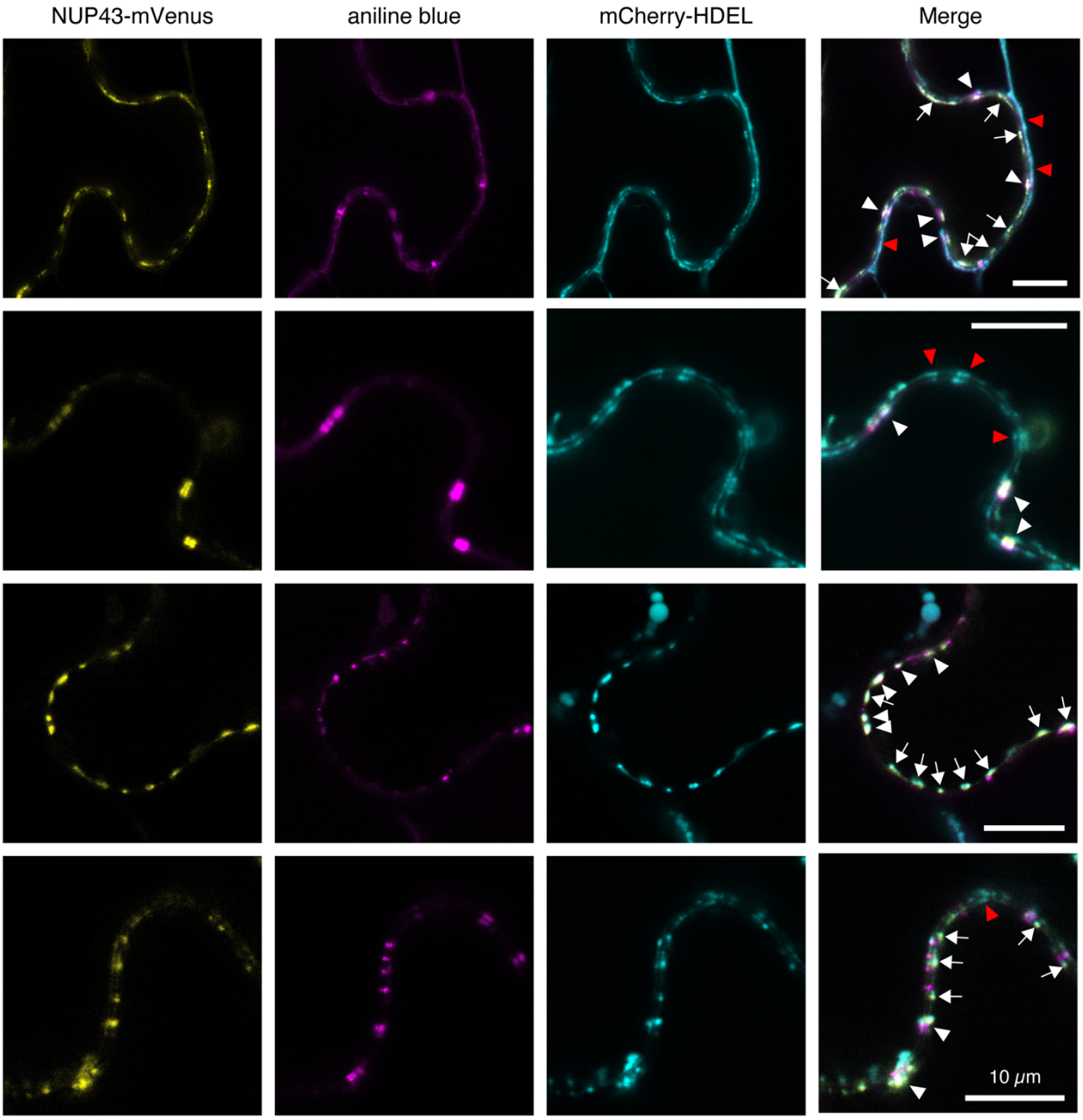

Figure 5- figure supplement 1. Arabidopsis NUP43 partially co-localizes with ER marker. Transient co-expression of NUP43-mVenus and mCherry-HDEL in *N. benthamiana* leaf epidermal cells, visualized by a single confocal optical section. Aniline blue was infiltrated to detect callose in pit fields as PD marker. White arrowheads indicate overlay of NUP43-mVenus, mCherry-HDEL. And aniline blue. Red arrows indicate mCherry-HDEL specific localization., without overly with other markers. White arrows (*middle right* panel) indicate overlay of NUP43-mVenus and mCherry-HDEL but absent aniline blue staining. Scale bar indicates 10 µm.

Figure 6 with 4 supplements

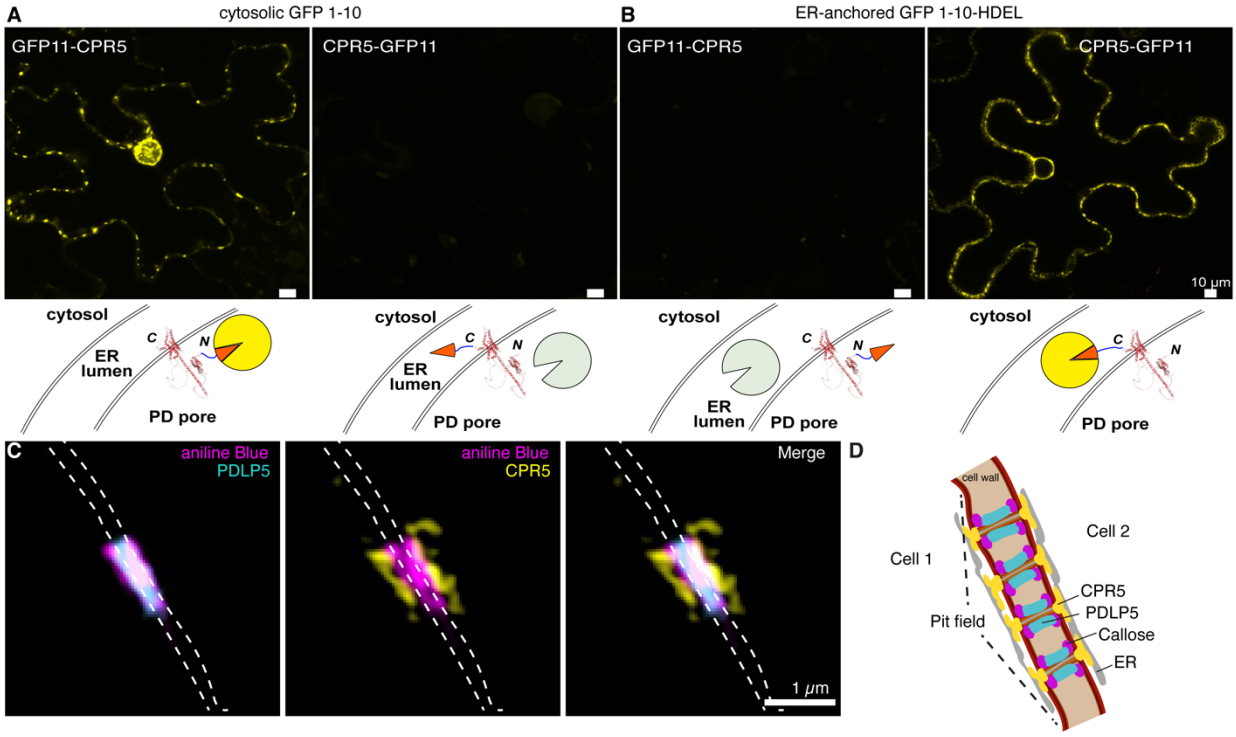

Figure 6. Arabidopsis CPR5 topology and localization of CPR5 near PD orifices. (A and B) Split-GFP membrane topology to test for the orientation of CPR5 in the nuclear pore membrane and the ER at PD by transiently expressing split-GFP fusions in *N. benthamiana,* visualized by single optical sections. (**A**) *(left)* Fluorescence reconstitution at PD between a cytosolic non-fluorescent GFP domain lacking β-sheet 11 (GFP1-10; the circle missing a wedge) and a fusion of the GFP11 to the N-terminus of CPR5 (the red wedge). Since reconstitution occurs at PD, each cartoon indicates reconstitution in the intermembrane space between ER/desmotubule and plasma membrane. *(right)* Cytosolic GFP1-10 and GFP11fusion to C-terminus of CPR5. (**B**) *(left)* ER-retained GFP1-10-HDEL and GFP11 fused to N-terminus of CPR5. *(right)* ER-retained GFP1-10-HDEL and fusion of GFP11 to C-terminus of CPR5. Repeated independently 3 times with comparable results. (**C**) CPR5-mCitrine close to the orifices of PD visualized by a single optical section recorded using Structured Illumination Microscopy in *N. benthamiana* leaves co-infiltrated with XVE:PDLP5-mScarlet3 and XVE:CPR5-mCitrine. Prior to imaging, leaves were infiltrated with aniline blue. PDLP5-mScarlet3: turquoise, CPR5-mCitrine: yellow, aniline blue: magenta. Repeated independently four times with comparable results. **(D)** Cartoon approximately to scale, illustrating PD in pit field between adjacent cells with callose marked magenta, PDLP5 turquoise, CPR5 yellow.

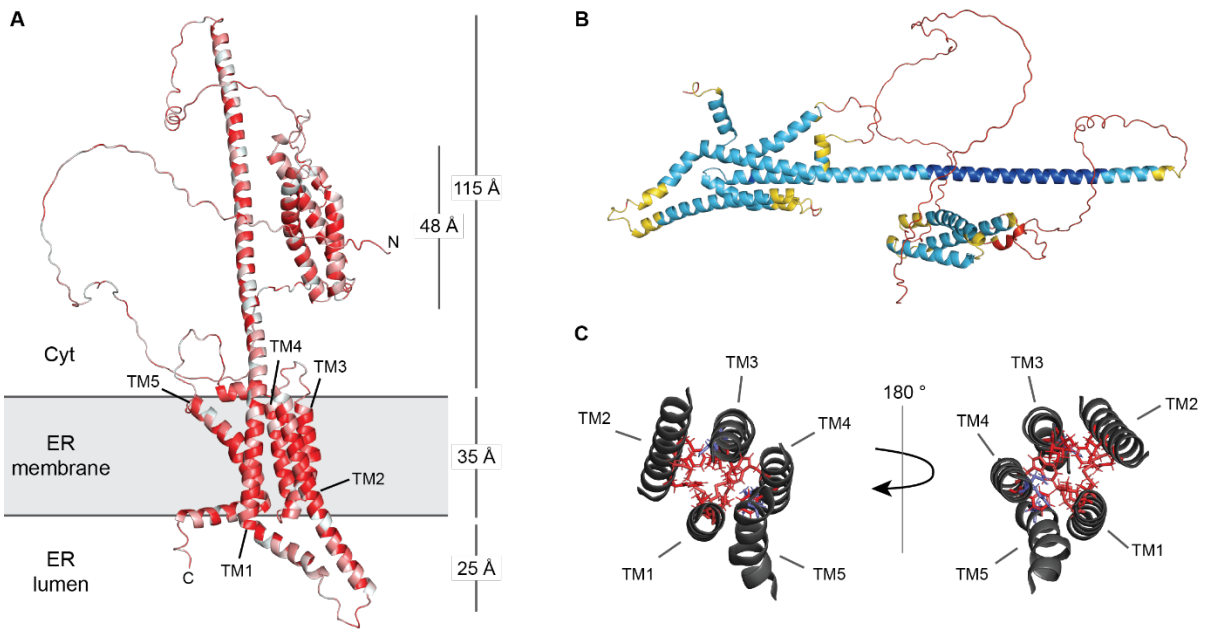

Figure 6-figure supplement 1. Predicted structure of monomeric CPR5 and model for integration into ER-derived membranes. Topological studies using the split-GFP system (Figure 4A,B, Figure 4-figure supplement 3) are consistent with a localization of the CPR5 C-terminus in the ER lumen, while its N-terminus extends into the cytoplasm. (**A**), CPR5 is composed of a N-terminal, disordered region (residues 1-106), a soluble domain formed by 3 α-helices (107-192), linked by a second disordered region (193- 265) to an approx. 115 Å long, central α-helix (266-342). Hydrophobic residues (red) of the central helix (TM1) and 4 shorter helices (TM2-TM5) form a transmembrane domain spanning approx. 35 Å, consistent with the expected thickness for ER-derived membranes. C-terminus and helical extensions of TM1 and TM2 reach into the ER lumen. (**B**), Structure colored by per-residue prediction confidence (pLDDT; dark blue: 90-100, light blue: 50-70, yellow: 50-70, red: < 50). Low confidence values (red) may indicate regions that are either intrinsically disordered or assume a structure when interacting with other proteins and therefore could partake in formation of complexes with NUPs. (**C**), View of transmembrane helical bundle from ER lumen (left) and cytoplasm (right). Amino acid side chains spanning between transmembrane helices are colored by hydrophobicity (blue: hydrophilic, red: hydrophobic). The CPR5 transmembrane domain is not predicted to form a solvent-accessible pore.

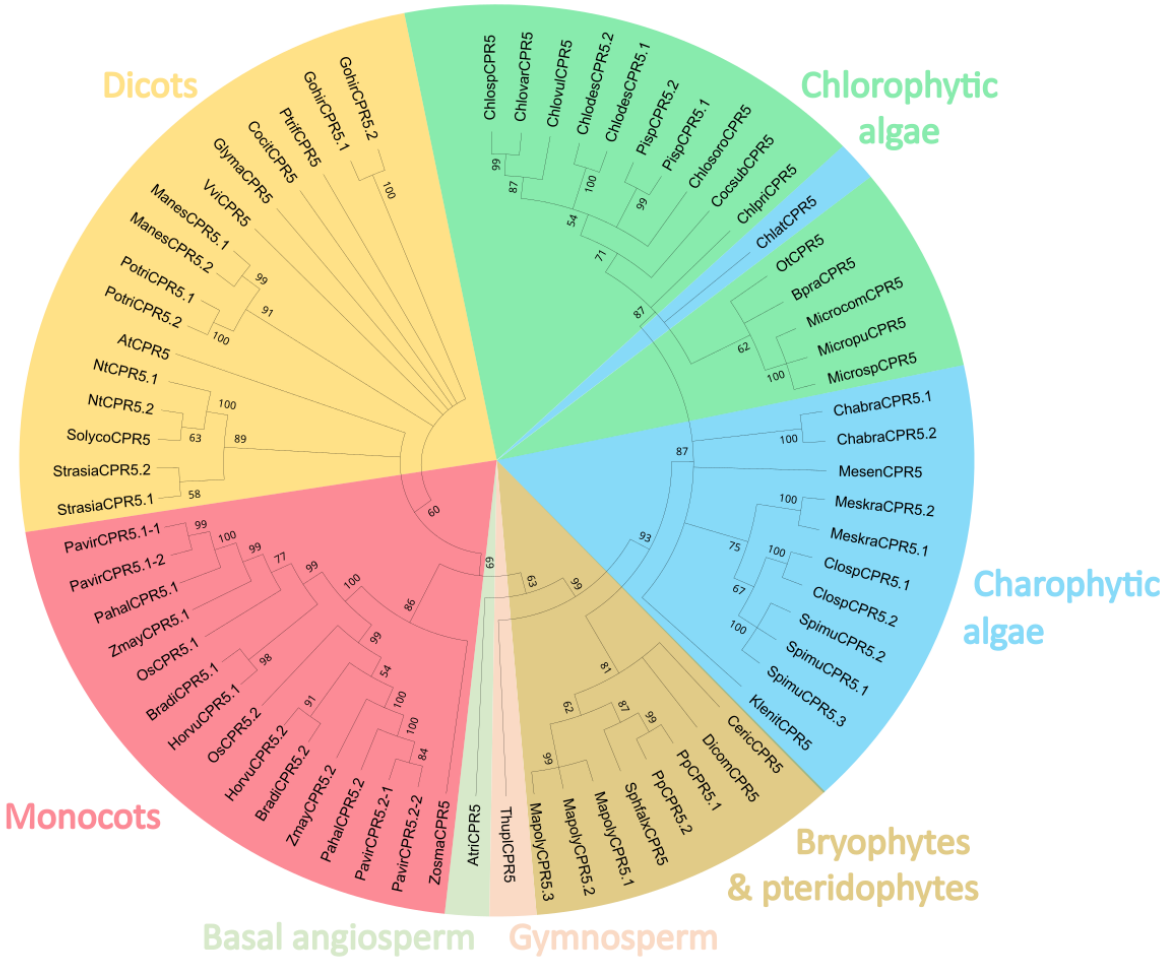

Figure 6-figure supplement 2: Phylogenetic analysis of CPR5 sequences. The accession numbers and the abbreviations corresponding to the mature protein sequences used for this analysis are given in table S7. The analysis was performed as described in the "Materials and Methods" section.

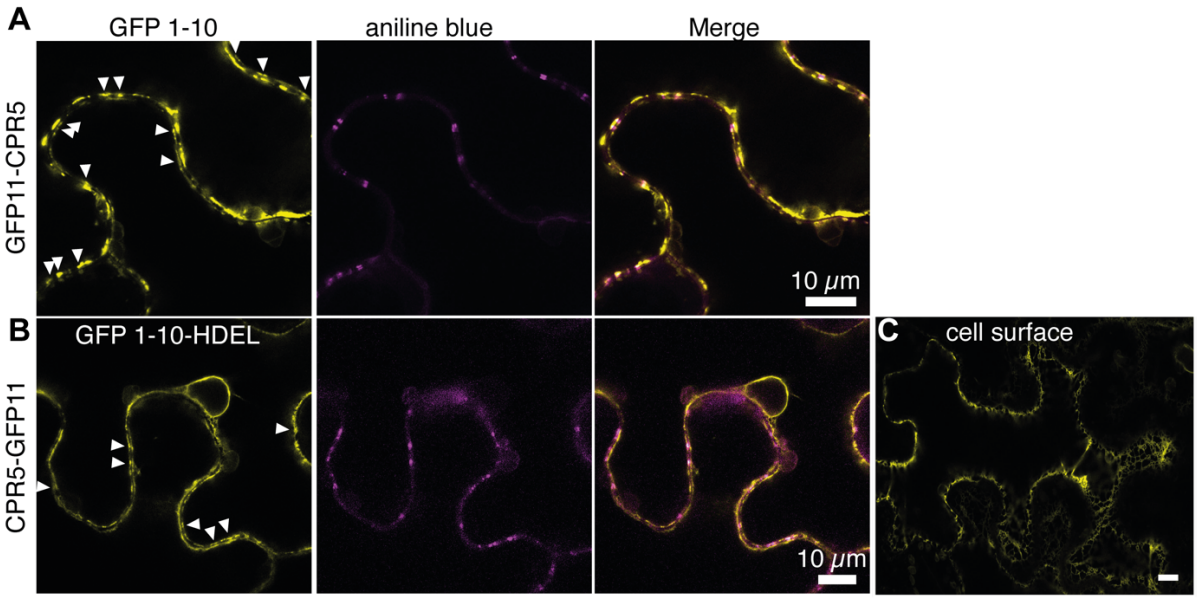

Figure 6-figure supplement 3. The C-terminus of Arabidopsis CPR5 faces ER lumen. (A), Transient co-expression of GFP11-CPR5 and cytosolic GFP1-10 in *N. benthamiana* leaves, same cell as shown in Figure 4. *Left*, GFP channel. Reconstitution can be observed also at PD (arrowheads). *Middle*, aniline blue. *Right,* merge. (**B**), *N. benthamiana* epidermal cells transiently expressing CPR5-GFP11 and ER luminal GFP1-10-HDEL, same cell as shown in Figure 4. *Left*, GFP channel. Reconstitution can be observed also at PD (arrowheads); *middle*, aniline blue*; right,* merge. (**C**), Surface view of the same cell as in B, showing reconstitution in the ER. Confocal images in Figure 6-figure supplement 3 are single optical sections.

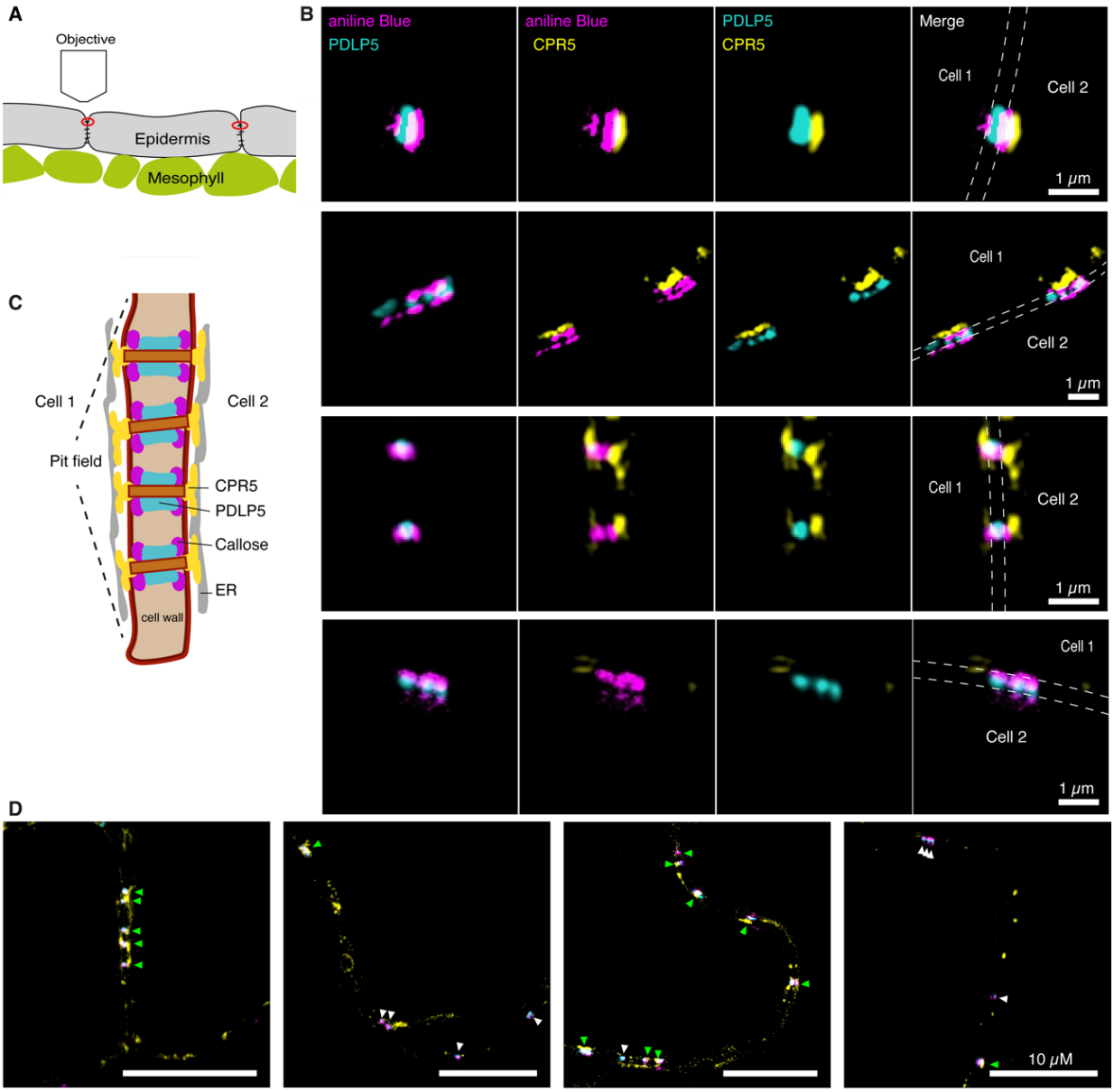

Figure 6-figure supplement 4. **Arabidopsis CPR5-mCitrine localizes at the orifices of PD**. (**A),** Cartoon showing analyzed PD: only PD most proximal to the cover glass and objective were analyzed to reduce effects caused by scattering of light due to cell wall. (**B),** single optical sections recorded using Structured Illumination Microscopy (SIM) in *N. benthamiana* leaves co-infiltrated with XVE:PDLP5-mScarlet3 and XVE:CPR5-mCitrine. Prior to the imaging, leaves were infiltrated with aniline blue. PDLP5-mScarlet3 in turquoise, CPR5-mCitrine in yellow, and aniline blue in magenta. Comparable results were obtained in four independent experiments. Dashed lines indicate approximation of cell wall boundaries. (**C),** Cartoon of pit field and localization of PDLP5 and CPR5. Fluorescence reporting on CPR5 in (B) extends laterally 200-1000 nm in the epidermal cell wall. Previously, the lateral extension of individual PD pores in the cell wall was estimated to 100 nm for basal trichome cell walls and 187 nm for epidermal cell walls (Faulkner et al., 2008; Fitzgibbon et al., 2010). The resolution achieved with SIM was not high enough to resolve single PD or determine whether pit fields consist of several simple PD (as shown in C) or a few complex (H-shaped/twinned) PD. (**D**), single optical sections recorded using SIM in *N. benthamiana* leaves co-infiltrated with XVE:PDLP5-mScarlet3 and XVE:CPR5-mCitrine. Green arrowheads indicate overlay between CPR5-mCitrine, PDLP5-mScarlet3 and aniline blue; white arrowheads indicate overlay between PDLP5-mScarlet3 and aniline blue, without CPR5-mCitrine. PDLP5-mScarlet3 in turquoise, CPR5-mCitrine in yellow, and aniline blue in magenta.

Figure 7 with 1 supplement

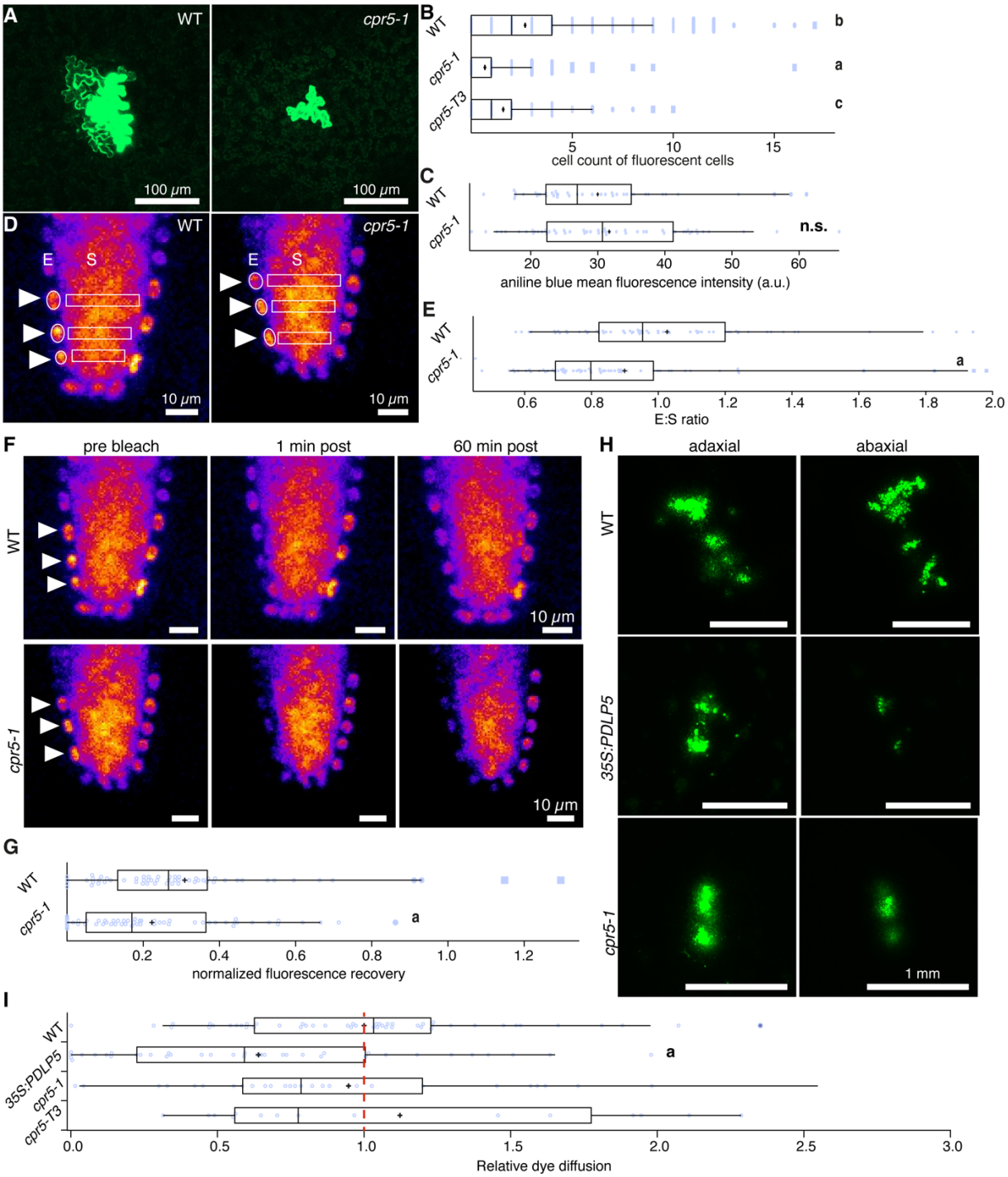

Figure 7. Defects in cell-to-cell transport of kDa-sized cargo in *cpr5* mutants. (A) Example maximum intensity projection of 32 optical cross-sections taken at 2.5 µm intervals with intercellular 2xmEGFP movement in wild type (WT, *left*) and *cpr5-1* (*right*) Arabidopsis leaves. Leaves were bombarded with gold particles coated with p35S:mEGFP-mEGFP DNA plasmids 24 h prior to the analysis by confocal microscopy (fusion protein abbreviated as 2xmEGFP). **(B)** Quantification of the mean intercellular spread of mEGFP by counting fluorescent cells in the GFP channel. $n_{(WT)}$ = 594 bombarded cells, 17 independent biological replicates; $n_{(cpr5\text{-}1)}$ = 278 bombarded cells, 6 independent biological replicates; $n_{(cpr5\text{-}T3)}$ = 99 bombarded cells, four independent biological replicates. Mean fluorescent cell counts: $n_{(WT)}$ = 2.67, $n_{(cpr5\text{-}T3)}$ = 1.59, $n_{(cpr5\text{-}1)}$ = 0.68; median fluorescence cell counts: $n_{(WT)}$ = 2, $n_{(cpr5\text{-}1)}$ = 0, $n_{(cpr5\text{-}T3)}$ = 1. Based on

Bonferroni-corrected Dunn´s test for pairwise comparison after Kruskal-Wallis test: **a** indicates significant difference to WT with $p_{(cpr5\text{-}1)} < 10^{-15}$; **b** indicates significant difference to WT with $p_{(cpr5\text{-}T3)} = 0.0004$; **c** indicates $p_{(cpr5\text{-}1 \text{ vs. } cpr5\text{-}T3)} = 0.0002$. Mean bootstrap analysis with 95% confidence interval (CI) and bootstrap resampling of $B = 5000$: $CI_{WT \text{ vs. } cpr5\text{-}1}$ [1 x 10^{-5} , 0.001], $p_{(cpr5\text{-}1)} = 0002$ **;** $CI_{WT \text{ vs. } cpr5\text{-}T3}$ [1 x 10^{-5} , 0.001], $p_{(cpr5\text{-}T3)} = 0.0002$**;** $CI_{cpr5\text{-}1 \text{ vs. } cpr5\text{-}T3}$, $p_{(cpr5\text{-}1 \text{ vs. } cpr5\text{-}T3)} = 0.0002$ [1 x 10^{-5} , 0.001]. **(C)** Callose quantification. $n_{(WT)} = 4$ independent experiments, $n_{(cpr5\text{-}1)} = 5$ independent experiments, graph summarizes all experiments. Student´s *t*-test $p = 0.48$. **(D)** Sum projections showing SHR–GFP distribution in WT (*left*) and *cpr5-1* mutant (*right*) Arabidopsis root. White circles and boxes indicate positions of endodermis nuclei (E, arrows) and corresponding regions in the stele (S, white boxes). **(E)** Quantification of SHR–GFP endodermis:stele ratio (E:S) for WT and *cpr5-1* mutant. $n_{(WT)} = 62$ nuclei, $n_{(cpr5\text{-}1)} = 62$ nuclei, with 3-4 nuclei analyzed per root. **a** indicates significantly decreased E:S in *cpr5-1* mutant, based on Mann-Whitney U test with $p = 0.0006$. **(F)**, Sum projections showing SHR–GFP distribution in WT (*top*) and *cpr5-1* mutant (*bottom*) Arabidopsis root. **(G)**, Quantification of relative SHR–GFP fluorescence recovery for WT and *cpr5-1* mutant after 1 h. Fluorescence recovery was normalized to a control nucleus in the endodermis (see Methods and Figure 5-figure supplement 1F). n(WT) = 59 bleached nuclei, n(*cpr5-1*) = 59, per root 3-4 nuclei were bleached. Student´s t-test p = 0.037 indicating significantly decreased fluorescence recovery after 60 min. **(H and I)** PD permeabilities examined by CFDA/CFSE-based DANS dye loading assays. **(H)** Epifluorescence reporting on CF diffusion in the epidermis of the adaxial (*left*) and abaxial (*right*) side of the Arabidopsis leaf. WT *(top), 35S*:*PDLP5* (*middle*), and *cpr5-1* (*bottom*). Bars, 1 mm. **(I)** Quantification of CF diffusion in WT and mutant lines. $n_{(WT)} = 49$ plants, 7 independent biological replicates; $n_{(35S:PDLP5)} = 38$ plants, 5 independent biological replicates; $n_{(cpr5\text{-}1)} = 29$ plants, 5 independent biological replicates; $n_{(cpr5\text{-}T3)} = 15$ plants, 5 independent biological replicates. Fluorescent areas on the abaxial side were identified using auto threshold and Fiji YEN-algorithm with user modifications. The same threshold setting was used for the adaxial side. The extent of dye diffusion was quantified by the ratio between the areal spread of fluorescence on the abaxial side and the areal spread of fluorescence on the adaxial side. **a** indicates significantly different on the basis of $p = 0.032$ level according to Bonferroni-corrected Dunn´s test for pair wise comparison following Kruskal-Wallis analysis.

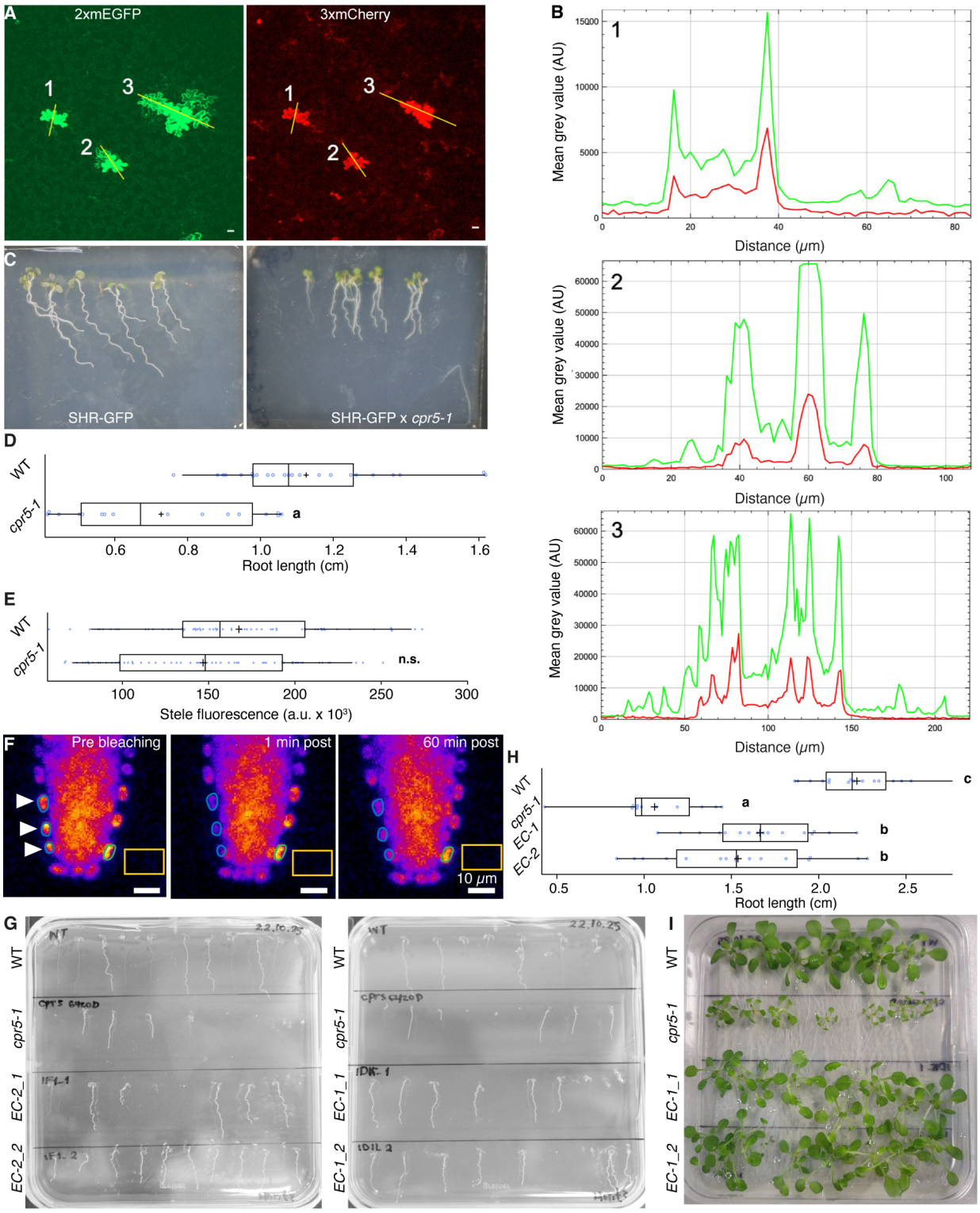

Figure 7-figure supplement 1. Intercellular transport assays in *cpr5-1* mutants. (A), Example of maximum intensity projection of 32 optical cross-sections taken at 2.5 µm intervals with three different clusters (1, 2, and 3) of fluorescent cells after bombardment in a WT Arabidopsis leaf. Each cluster reports a successful bombardment event. Left, GFP channel, right, mCherry channel. 24 h prior to the experiment, leaves were co-bombarded with gold particles coated with p35S:mEGFP-mEGFP (2xmEGFP). DNA plasmids and gold particles coated with p35S:mCherry-mCherry-mCherry (3xmCherry). **(B),** Profile plots across the different clusters, 1, 2, and 3 as shown in A. Yellow lines in A indicate the position for the profile. The bombarded cell marked with 3xmCherry overlays with the brightest cell in the GFP channel. **(C),** Six-day old Arabidopsis seedlings with *shr*/pSHR:SHR-GFP in WT Col-0 background *(left)* and

shr/pSHR:SHR-GFP in the *cpr5-1* background (*right*) grown on ½ MS agar. **(D),** Quantification of the root length of 6-day old WT and *cpr5-1* mutant background seedlings. $n_{(WT)}$ = 23 roots, four independent experiments, $n_{(cpr5\text{-}1)}$ = 16 roots, three independent experiments. **a** Significantly decreased root length in *cpr5-1* mutant, based on Student´s *t*-test with $p = 0.00002$. **(E),** Quantification of SHR-GFP stele baseline fluorescence in *cpr5-1* mutant and WT background. $n_{(WT)}$ = 62 stele ROIs, $n_{(cpr5\text{-}1)}$ = 62 stele ROIs, with 3-4 ROIs analyzed per root. **n.s.,** no significant difference in fluorescence intensity based on Mann-Whitney U test with $p = 0.074$. **(F)**, SHR–GFP fluorescence recovery after photobleaching (FRAP) in homozygous *shr*/pSHR:SHR-GFP root endodermal cells (arrow heads). Note that for comparison, we here show the same sum projections as in Figure 5F (*top*). Blue circles show the position of ROIs for FRAP. Green circle shows the position of ROI for control nucleus used for normalization (see Methods). Yellow square shows the position for mean background fluorescence used for correction (see Methods). **(G)**, Seven-day old Arabidopsis WT Col-0 and *cpr5-1* mutant seedlings (*left* and *right*), and *cpr5-1*/pCPR5:CPR5-mCitrine independent expression complementation (EC) lines (*EC-1 and EC-2*). For each complementation line, two sublines are shown (*left*: *EC-1_1* and *EC-1_2*; *right: EC-2_1, EC-2_2*), grown on ½ MS agar. **(H),** Quantification of the root length of 7-day old WT and *cpr5-1* mutant background, as well as pooled *EC-1* lines and *EC-2* lines. Quantification is based on two independent experiments with $n_{(WT)}$ = 16 roots, $n_{(cpr5\text{-}1)}$ = 11 roots, $n_{(IF_1)}$ = 16 roots, $n_{(EC\text{-}1)}$ = 16 roots. Different letters indicate significant difference tested by one-way ANOVA ($p = 5 \times 10^{-11}$) and Tukey *post hoc* analysis. $p_{(WT\ vs.\ cpr5\text{-}1)} = 2 \times 10^{-11}$, $p_{(EC\text{-}2\ vs.\ cpr5\text{-}1)} = 0.003$, $p_{(EC\text{-}1\ vs\ cpr5\text{-}1)} = 0.0001$, $p_{(WT\ vs\ EC\text{-}2)} = 0.000002$, $p_{(WT\ vs\ EC\text{-}1)} = 0.0001$. **(I),** same plate as in (G) *right* but 3 weeks later, with seedlings grown 4-weeks in total.

Supplementary Tables

table S1. Genome-wide search for potential phase-separating proteins with FG repeats. The 15 genes with the highest number of FG motifs within a 200-amino acid window in the *Physcomitrium* genome. For the list summarizing the genome-wide search for FG containing genes, see file S1. For Arabidopsis NUPs see file S2.

Gene	max #FG in 200 aa window	Predicted function
Pp3c26_7720	28	NUP96
Pp3c3_17910	28	NUP 98.1
Pp3c3_28570	25	NUP 98.2
Pp3c26_7680	25	NUP 98.3
Pp3c8_3950	21	NUP 98.4
Pp3c15_14630	19	NUP62
Pp3c14_14130	17	NUP54.1
Pp3c17_4470	16	inter-alpha-trypsin inhibitor heavy chain-related
Pp3c24_6760	14	NUP58
Pp3c13_12950	14	NUP214
Pp3c10_15930	13	NUP54.2
Pp3c10_15937	13	NUP54.3
Pp3c7_12210	12	zinc finger (CCCH-type) family protein
Pp3c24_6760	11	NUP58
Pp3c13_24530	10	Epidermal growth factor receptor substrate 15-like 1

table S2. List of known Arabidopsis NUPs and summary of localization results. *p*-values calculated from Bonferroni-corrected pairwise comparison between the tested NUP with propidium iodide marked by *; *p*-values calculated from Bonferroni-corrected pairwise comparison between the tested NUP and free mScarlet3 marked by #. Index is short for PD index (see also Figure 2 and 3). NA: not assessed. FG-NUPs in red.

NUP	AGI	Localization at NPC	Tested for localization
NDC1	AT1G73240	membrane anchor	NA
Gp210	AT5G40480	membrane anchor	index = 1.77, *** = 2x10^{-9}; # = 3x10^{-6}**
CPR5	AT5G64930	membrane anchor	index = 1.48, *** = 7x10^{-8}; # = 0.0001**
PNET1	AT1G07970	membrane anchor	NA
NUP155	AT1G14850	inner ring	index = 1.34, *** = 0.002**; # = 1.0
NUP93a	AT2G41620	inner ring	index = 1.38, *** = 0.001**; # = 1.0
NUP35/MPPN	AT3G16310	inner ring	index = 1.36, *** = 0.0002**; # = 0.549
NUP93b	AT3G57350	inner ring	index = 1.19, * = 0.43; # = 1.0
NUP188	AT4G38760	inner ring	NA
NUP205	AT5G51200	inner ring	NA
NUP160	AT1G33410	outer ring	NA
Seh1	AT1G64350	outer ring	NA
NUP96	AT1G80680	outer ring	NA
NUP133	AT2G05120	outer ring	NA
Sec13	AT2G30050	outer ring	NA
Elys/HOS1	AT2G39810	outer ring	index = 1.52, *** = 3x10^{-7}; # = 0.001**
NUP107	AT3G14120	outer ring	NA
NUP43	AT4G30840	outer ring	index = 1.72, *** = 3x10^{-6}; # = 0.006**
NUP75/85/SBB1	AT4G32910	outer ring	NA
NUP98a	AT1G10390	core FG-NUP	index = 1.38, *** = 0.006**; # = 1.0
NUP54	AT1G24310	core FG-NUP	NA
NUP98b	AT1G59660	core FG-NUP	index = 1.55, *** = 0.0001;** # = 0.276
NUP62	AT2G45000	core FG-NUP	index = 1.34, *** = 0.0001;** # = 0.357
NUP58	AT4G37130	core FG-NUP	index = 1.37, *** = 0.001;** # = 1.0
CG1	AT1G75340	cytoplasmic FG-NUP	NA
GLE1	AT1G13120	cytoplasmic NUP	NA
NUP214	AT1G55540	cytoplasmic FG-NUP	index = 1.29, *** = 0.041;** # = 1.0
Rae1	AT1G80670	cytoplasmic NUP	index = 1.22, * = 0.301; # = 1.0
Aladin	AT3G56900	cytoplasmic NUP	NA
MOS7/NUP88	AT5G05680	cytoplasmic NUP	NA
NUP50a	AT1G52380	basket FG-NUP	NA
NUA/TPR/ATTPR	AT1G79280	basket	NA
NUP1/NUP136	AT3G10650	basket FG-NUP	NA
NUP50b	AT3G15970	basket FG-NUP	index = 1.06, * = 1.0; # = 1.0
NUP82	AT5G20200	basket	index = 1.24, * = 0.1; # = 1.0

table S4. NPC components identified in published cell wall/PD proteomes

NUP	Reference
CPR5	(Kraner et al., 2017)
NUP93a	(Kirk et al., 2022)
NUP155	(Bayer et al., 2006; Fernandez-Calvino et al., 2011; Kraner et al., 2017)
SEC13	(Bayer et al., 2006; Gombos et al., 2023; Kraner et al., 2017)
NUP205	(Kirk et al., 2022)
NUA	(Gombos et al., 2023)
NUP50a *	(Gombos et al., 2023; Kraner et al., 2017; Li et al., 2024)
GP210	(Kraner et al., 2017)
NUP35	(Kraner et al., 2017)
HOS1	(Kraner et al., 2017)
NUP43	(Kraner et al., 2017)
NUP62	(Kraner et al., 2017)
NUP214	(Kraner et al., 2017)
NUP82	(Kraner et al., 2017)
NDC1 *	(Li et al., 2024)

* identified by TURBO-ID using PD proteins

table S5. Nuclear localization and observation of puncta in the cell periphery, consistent with PD localization by other laboratories

NUP	Transient expression	Stable transformation/ promoter	Reference
CPR5	*p35S:YFP-CPR5*	*p35S:GFP-CPR5/cpr5-1*	(Gu et al., 2016)
CPR5*	*p35S:CFP-CPR5*		(Peng et al., 2022)
NUP98a	*p35S:GFP-Dra2-GFP*	*p35S:NtDra2-GFP*	(Gallemí et al., 2016)
NUP155	*p35S:Nup155-cYFP+p35S:nYFP-CPR5*		(Gu et al., 2016)
HOS1	*p35S:HOS1-GFP*		(Lee et al., 2012)
NUP62	*p35S:Nup62-nYFP+p35S:FLC-cYFP*		(Chen et al., 2023)

* split-FP analysis indicated interaction of CPR5 with PRL1 and FIP1

table S6. Membrane/microtubule anchor proteins in NPC and ciliary gates across kingdoms

Organism/ location	# TM	Yeast	Mammalian	Chlamydomonas	Arabidopsis	*P. patens*	Ref.
NPC lumenal ring	1	POM152	GP210	n.p.	GP210	*Pp3c27_1470V3.1*	(Collins et al., 2023; Tamura et al., 2010)
NPC	1	POM121	POM121	n.p.	n.p.	n.p.	
NPC	6	NDC1	NDC1	*Cre03.g197550.t1.2*	NDC1	*Pp3c23_16320V3.1*	(Collins et al., 2023; Mansfeld et al., 2006)
NPC	3	POM33	TMEM33	*Cre02.g099650.t1.2*	*At3g02420*	*Pp3c7_9290V3.1*	this work
Ciliary gate	3	NPHP	TMEM218	*CEP290*	n.p.	n.p.	(Blasius et al., 2019; Craige et al., 2010; Epting et al., 2022; Li et al., 2016; Tang et al., 2020)
NPC	2	POM34	TMEM209	n.p.	PNET1 (*At1g07970*)	*Pp3c12_22070V3.1*	[48]
NPC green lineage	5	n.p.	n.p.	n.p.	CPR5	*Pp3c21_530V3.1* *Pp3c22_5670V3.1*	(Arra et al., 2024; Gu et al., 2016)

n.p. not present based on database searches

table S7. Accession numbers of CPR5 homologs used for the phylogenetic analysis shown in figure S6.

Protein name	Accession number	Species	Phylogeny	
ChabraCPR5.1	GBG69762.1	*Chara braunii*	Charophyta	Charophyceae
ChabraCPR5.2	GBG89669.1	*Chara braunii*	Charophyta	Charophyceae
ChlatCPR5	jgi|Chlat1|5100|Chrsp33S05109	*Chlorokybus atmophyticus*	Charophyta	Chlorokybophy-ceae
ClospCPR5.1	GJP55885.1	*Closterium*	Charophyta	Zygnemo-phyceae
ClospCPR5.2	GJP75531.1	*Closterium*	Charophyta	Zygnemo-phyceae
KlenitCPR5	GAQ84352.1	*Klebsormidium nitens*	Charophyta	Klebsormidio-phyceae
MesenCPR5	jgi|Mesen1|2959|ME000176S02004	*Mesotaenium endlicherianum SAG 12.97*	Charophyta	Zygnemo-phyceae
MeskraCPR5.1	jgi|Meskra657_3|1148962|CE1148961_11182	*Mesotaenium kramstae Lemmermann NIES-657 v3.0*	Charophyta	Zygnemo-phyceae
MeskraCPR5.2	jgi|Meskra657_3|1148923|CE1148922_14999	*Mesotaenium kramstae Lemmermann NIES-657 v3.0*	Charophyta	Zygnemo-phyceae
SpimuCPR5.1	jgi|Spimu1|7829|SM000018S03736	*Spirogloea muscicola CCAC 0214*	Charophyta	Spiroglo-eophycidae
SpimuCPR5.2	jgi|Spimu1|5703|SM000152S01566	*Spirogloea muscicola CCAC 0215*	Charophyta	Spiroglo-eophycidae
SpimuCPR5.3	jgi|Spimu1|9349|SM000020S05962	*Spirogloea muscicola CCAC 0216*	Charophyta	Spiroglo-eophycidae
BpraCPR5	BPRRCC1105_03G01860	*Bathycoccus prasinos*	Chlorophyta	Mamiello-phyceae
ChlodesCPR5.1	KAH7624053.1	*Chlorella desiccata (nom. nud.)*	Chlorophyta	Trebouxio-phyceae
ChlodesCPR5.2	KAG7670930.1	*Chlorella desiccata (nom. nud.)*	Chlorophyta	Trebouxio-phyceae
ChlosoroCPR5	PRW44950.1	*Chlorella sorokiniana*	Chlorophyta	Trebouxio-phyceae
ChlospCPR5	CNC64A_008G01100	*Chlorella sp NC64A*	Chlorophyta	Trebouxio-phyceae
ChlovarCPR5	XP_005848448.1	*Chlorella variabilis*	Chlorophyta	Trebouxio-phyceae
ChlovulCPR5	KAI3426217.1	*Chlorella vulgaris*	Chlorophyta	Trebouxio-phyceae
ChlpriCPR5	QDZ25445.1	*Chloropicon primus*	Chlorophyta	Chloropico-phyceae
CocsubCPR5	CV00G07110	*Coccomyxa sub-ellipsoidea C-169*	Chlorophyta	Trebouxio-phyceae
MicrocomCPR5	XP_002502434.1	*Micromonas commoda*	Chlorophyta	Mamiello-phyceae
MicropuCPR5	EuGene.0500010166|58433	*Micromonas pusilla strain CCMP1545*	Chlorophyta	Mamiello-phyceae
MicrospCPR5	M.spRCC299 v3.0|58433	*Micromonas sp or commoda RCC299 v3.0*	Chlorophyta	Mamiello-phyceae
OtCPR5	OT_02G03660	*Ostreococcus tauri*	Chlorophyta	Mamiello-phyceae
PispCPR5.1	KAI8111799.1	*Picochlorum*	Chlorophyta	Trebouxio-

		sp. BPE23		phyceae
PispCPR5.2	KAI8109780.1	*Picochlorum sp. BPE23*	Chlorophyta	Trebouxio-phyceae
MapolyCPR5.1	Mapoly0107s0002.1.p	*Marchantia polymorpha_320_v3.1*	Seedless non-tracheophyte	Marchantiopsida
MapolyCPR5.2	Mapoly0483s0001.1.p	*Marchantia polymorpha_320_v3.1*	Seedless non-tracheophyte	Marchantiopsida
MapolyCPR5.3	Mapoly0002s0001.1.p	*Marchantia polymorpha_320_v3.1*	Seedless non-tracheophyte	Marchantiopsida
PpCPR5.1	Pp3c21_530V3.1.p	*Physcomitrium patens_318_v3.3*	Seedless non-tracheophyte	Bryopsida
PpCPR5.2	Pp3c22_5670V3.1.p	*Physcomitrium patens_318_v3.3*	Seedless non-tracheophyte	Bryophyta
SphfalxCPR5	Sphfalx02G141400.1.p	*Sphagnum fallax v1.1*	Seedless non-tracheophyte	Bryophyta
DicomCPR5	Dicom.14G001200.1.p	*Diphasiastrum complanatum v3.1*	Seedless tracheophyte	Lycopodiopsida
CericCPR5	Ceric.38G046900.1.p	*Ceratopteris richardii v2.1*	Seedless tracheophyte	Polypodiopsida
AtriCPR5	ATR_00156G00170	*Amborella trichopoda*	Spermatophyta	Basal angiosperm
AtCPR5	AT5G64930	*Arabidopsis thaliana*	Spermatophyta	Dicot
BradiCPR5.1	Bradi3g57717.1.p	*Brachypodium distachyon v3.1*	Spermatophyta	Monocot
BradiCPR5.2	Bradi2g58840.1.p	*Brachypodium distachyon v3.1*	Spermatophyta	Monocot
CocitCPR5	Cocit.H3845.1.p	*Corymbia citriodora v2.1*	Spermatophyta	Dicot
GlymaCPR5	Glyma.06G145800.1.p	*Glycine max Wm82.a4.v1*	Spermatophyta	Dicot
GohirCPR5.1	Gohir.D03G045400.2.p	*Gossypium hirsutum v3.1*	Spermatophyta	Dicot
GohirCPR5.2	Gohir.A02G134000.1.p	*Gossypium hirsutum v3.1*	Spermatophyta	Dicot
HorvuCPR5.1	HORVU.MOREX.r3.6HG0618780.1	*Hordeum vulgare Morex V3*	Spermatophyta	Monocot
HorvuCPR5.2	HORVU.MOREX.r3.3HG0309890.1	*Hordeum vulgare Morex V3*	Spermatophyta	Monocot
ManesCPR5.1	Manes.13G077600.1.p	*Manihot esculenta v8.1*	Spermatophyta	Dicot
ManesCPR5.2	Manes.12G141400.1.p	*Manihot esculenta v8.1*	Spermatophyta	Dicot
NtCPR5.1	mRNA_71958	*Nicotiana tabacum K326*	Spermatophyta	Dicot
NtCPR5.2	mRNA_118909	*Nicotiana tabacum K326*	Spermatophyta	Dicot
OsCPR5.1	LOC_Os02g53070.1	*Oryza sativa_323_v7.0*	Spermatophyta	Monocot
OsCPR5.2	LOC_Os01g68970.1	*Oryza sativa_323_v7.0*	Spermatophyta	Monocot
PahalCPR5.2	Pahal.5G042600.1.p	*Panicum hallii v3.1*	Spermatophyta	Monocot
PahalCPR5.1	Pahal.1G413600.1.p	*Panicum hallii v3.2*	Spermatophyta	Monocot
PavirCPR5.1-1	Pavir.1KG111437.1.p	*Panicum virgatum v5.1*	Spermatophyta	Monocot
PavirCPR5.1-2	Pavir.1NG487400.1.p	*Panicum virgatum v5.1*	Spermatophyta	Monocot

PavirCPR5.2-1	Pavir.5NG012660.1.p	*Panicum virgatum v5.1*	Spermatophyta	Monocot
PavirCPR5.2-2	Pavir.5KG720000.1.p	*Panicum virgatum v5.1*	Spermatophyta	Monocot
PtrifCPR5	Ptrif.0007s2410.1.p	*Poncirus trifoliata v1.3.1*	Spermatophyta	Dicot
PotriCPR5.1	Potri.005G083600.1.p	*Populus trichocarpa v4.1*	Spermatophyta	Dicot
PotriCPR5.2	Potri.007G082100.1.p	*Populus trichocarpa v4.1*	Spermatophyta	Dicot
SolycoCPR5	Solyc04g054170.4.1	*Solanum lycopersicum ITAG4.0*	Spermatophyta	Dicot
StrasiaCPR5.1	GER47577.1	*Striga_asiatica_ 008636005.1_SGA_v2.0*	Spermatophyta	Dicot
StrasiaCPR5.2	GER47578.1	*Striga_asiatica 008636005.1_SGA_v2.0*	Spermatophyta	Dicot
ThuplCPR5	Thupl.29379795s0007.1.p	*Thuja plicata v3.1*	Spermatophyta	Gymnosperm
VviCPR5	VIT_207s0031g01470.1	*Vitis vinifera v2.1*	Spermatophyta	Dicot
ZmayCPR5.1	Zm00001d052145_P001	*Zea mays RefGen_V4*	Spermatophyta	Monocot
ZmayCPR5.2	Zm00001d012040_P001	*Zea mays RefGen_V4*	Spermatophyta	Monocot
ZosmaCPR5	Zosma03g20130.1	*Zostera marina v3.1*	Spermatophyta	Monocot

table S8. Primers used in this study

Primer	Sequence (5´-3´)	Description
NUP98a_Fw	TACAAAAAAGCAGGCTTCATGTTTGGCTCATCTAATCCTTTTGG	**For localization**
NUP98a_Rv	CAAGAAAGCTGGGTCAACTCCATCTTCTTCATCTTCGT	
NUP155_Fw	TACAAAAAAGCAGGCTTCAAGATGTCACAAGACGATGAG	
NUP155_Rv	CAAGAAAGCTGGGTCGAAGGAGAATGGACTTAAGAGAGACT	
NUP160_Fw	TACAAAAAAGCAGGCTTCATGGAGGAGAATCGTCGG	
NUP160_Rv	CAAGAAAGCTGGGTCACCGGTTGCAGAGGATACAG	
NUP50a_Fw	TACAAAAAAGCAGGCTTCATGGGTGACTCGGAAAACGT	
NUP50a_Rv	CAAGAAAGCTGGGTCAGTATCTGTAGCTGTTGGAGAGT	
NUP214_Fw	TACAAAAAAGCAGGCTTCAAGATGAGCAGAGTTGAGATTGAAG	
NUP214_Rv	CAAGAAAGCTGGGTCTTTTCTCATCTGTGTGAAGAGTTCC	
Rae1_Fw	TACAAAAAAGCAGGCTTCATGGCAACTTTTGGTGCGC	
Rae1_Rv	CAAGAAAGCTGGGTCTTTTCTGCCGGTTGCTCCAA	
Sec13_Fw	TACAAAAAAGCAGGCTTCAACATGCCAGGTCAGAAGATTGA	
Sec13_Rv	CAAGAAAGCTGGGTCAGGCTCAACAGCAGTAACTTGTTCC	
Elys/HOS1_Fw	TACAAAAAAGCAGGCTTCATGGATACGAGAGAAATCAACGGT	
Elys/HOS1_Rv	CAAGAAAGCTGGGTCTCTTGCTGCGAATCTACGTCT	
NUP93a_Fw	TACAAAAAAGCAGGCTTCATGGCGAACGACCAAGAGAT	
NUP93a_Rv	CAAGAAAGCTGGGTCAAAGCTTCGAGCCACCTTCTCG	
NUP62_Fw	TACAAAAAAGCAGGCTTCATGTCGGGGTTTCCATTTGGT	
NUP62_Rv	CAAGAAAGCTGGGTCAGACATCCAGTGCTTTGG	
NUP136_Fw	TACAAAAAAGCAGGCTTCCTAATGGCGAGCGCGGCAC	
NUP136_Rv	CAAGAAAGCTGGGTCTTTCTTCCTGGTGGATTTCTTTGC	
NUP107_Fw	TACAAAAAAGCAGGCTTCATGGATATGGATATGGACACTTCCC	
NUP107_Rv	CAAGAAAGCTGGGTCAGGTGATGAAAGTTCCTCTTGA	
NUP50b_Fw	TACAAAAAAGCAGGCTTCATGGGGGACTCCGATAATGC	
NUP50b_Rv	CAAGAAAGCTGGGTCCCTAGCATCTTCAGCACTCGGTGAG	
NUP35_Fw	TACAAAAAAGCAGGCTTCAAAATGAGTGCTGCAGCACACAGG	
NUP35_Rv	CAAGAAAGCTGGGTCAACACCGAACATCAAGTCAAAGA	
NUP93b_Fw	TACAAAAAAGCAGGCTTCATGGCGAACGACCAGGAG	
NUP93b_Rv	CAAGAAAGCTGGGTCAAAGCTTCGAGCTATCTTCTCG	
NUP43_Fw	TACAAAAAAGCAGGCTTCATGGAGATGATGCAGGATTCGT	
NUP43_Rv	CAAGAAAGCTGGGTCAGGCCTTGAGAAAACTGCTA	
NUP85_Fw	TACAAAAAAGCAGGCTTCAAAATGCCGGGTATGTCTTCGGA	
NUP85_Rv	CAAGAAAGCTGGGTCACATTCTTCGAGAAAAGCACGT	
NUP58_Fw	TACAAAAAAGCAGGCTTCATGTCGTTTTTTCCCCCAC	
NUP58_Rv	CAAGAAAGCTGGGTCTGTACGGCGTGTAGTTCGAGATTTT	
NUP82_Fw	TACAAAAAAGCAGGCTTCGAGTTCATGGCCACTCAAGGAGAAGC	
NUP82_Rv	CAAGAAAGCTGGGTCTGTCTTACAGCAGACACCGTCACTT	
Gp210_Fw	TACAAAAAAGCAGGCTTCATGGTTCCCGTCTCGTTCTG	
Gp210_Rv	CAAGAAAGCTGGGTCCATAGTGTTTTGAGGATTAAACC	
NUP205_Fw	TACAAAAAAGCAGGCTTCATGGTGTCGCCGAAAGATTT	
NUP205_Rv	CAAGAAAGCTGGGTCTACACACTTTTGGATGGCCA	
CPR5_Fw	TACAAAAAAGCAGGCTTCTTTAAGGCTATGGAAGCCCTCCTCC	
CPR5_Rv	CAAGAAAGCTGGGTCCTCGTCAGCATAGTCAGACCCACCA	
GGBmScarlet3F	AAAGGTCTCAAACAATGGACAGTACCGAAGCT	
GGBmScarlet3R	AAAGGTCTCAAGCCGGATCCCCCGGAGC	
PpNUP98.1_Fw	TGTACAAAAAAGCAGGCTTAATGTTTGGATCCAGCAGCCC	
PpNUP98.1_Rv	TGTACAAGAAAGCTGGGTAATCAAAATCCAGACCATATCCACTG	
2_Fw	AAAAAAGCAGGCTTAATGTCGGGCTTCACAGGATT	
PpNup62_Rv	AAGAAAGCTGGGTAGGCTCCACGCAAACGAGATC	
PpNup58_Fw	AAAAAAGCAGGCTTAATGGCGGGGATGTTCCAAAC	
PpNup58_Rv	AAGAAAGCTGGGTACTTTCGACGTGTGCCAC	
PpNup35.1_Fw	TACAAAAAAGCAGGCTTCATGAGTACCCCAGGCGCG	
PpNup35.1_Rv	CAAGAAAGCTGGGTCCATACCAAATACAAAATCCACAAATT	

PDLP5_SIM_Fw	TTTGGTCTCAGGCTCTATGATCAAGACAAAGACGACG	**For SIM**
PDLP5_SIM_Rv	TTTGGTCTCACTGATTTACACCATTTCTCATCTGCA	
CPR5_SIM_Fw	TTTGGTCTCAGGCTCTATGGAAGCCCTCCTCCTC	
CPR5_SIM_Fw	TTTGGTCTCACTGAAGCATAGTCAGACCCACC	
GGDmScarlet3F	AAAGGTCTCATCAGGTATGGACAGTACCGAAGCT	
GGDmScarlet3R	AAAGGTCTCAGCAGGGATCCCCCGGAGC	
CPR5_Topol_Rv	GGGGACCACTTTGTACAAGAAAGCTGGGTATCAAGCATAGTCAG ACCCACC	**For CPR5 topology**
mEGFP_Fw	GGGGACAAGTTTGTACAAAAAAGCAGGCTTCACCATGGTGAGCA AGGGCGAGG	**For microparticle bombardment**
mEGFP_Rv	GGGGACCACTTTGTACAAGAAAGCTGGGTGTTACTTGTACAGCT CGTCCATGCC	
2xmEGFP_Fw	GGGGACAAGTTTGTACAAAAAAGCAGGCTTCACCATGGTTTCTA AGGGTGAGG	
2xmEGFP_Rv	GGGGACCACTTTGTACAAGAAAGCTGGGTGTTACTTGTACAGCT CGTCCATGCC	
NUP62_F	GCTTTTTCTATTGAGGTTCAAACTTGTAAGC	**For transgenic line expressing NUP62-GFP**
NUP62_R	CCGGTCAAGAGAAATATAATAATCTCTG	
NUP62_U1	AGACATCCAGTGCTTTGGAGCC	
NUP62_D1	TGATAAGAATTACAAAAACCACATAATCTC	
NUP62GFP_HiFiF	AAGCACTGGATGTCTGGTGGAGGCGGTTCAGGCGGAGGTGG	
NUP62GFP_HiFiR	TTGTAATTCTTATCACTTGTACAGCTCGTCCATGCCGTG	